On-chip receiver RF front-end

Torleif Skår

Thesis submitted for the degree of
Master in Electrical Engineering, Informatics and Technology
(Microelectronics and sensor technology)
60 credits

Department of Physics
Faculty of mathematics and natural sciences

UNIVERSITY OF OSLO

Autumn 2020

On-chip receiver RF front-end

Torleif Skår

On-chip receiver RF front-end

http://www.duo.uio.no/

Printed: Reprosentralen, University of Oslo

First and foremost, I would like to express my sincere gratitude to my supervisors, Sumit Bagga & Dag T. Wisland. Thanks for both the opportunity to take on this thesis, as well as providing me with your scientific insight in the field of RFIC design. This wouldn't have been possible without you.

I would also like to extend my thanks to Kristian Kjelgård at the Nanoelectronics group for helping out with all lab related things, whether it would be PCBs, wire-bonding, wafer-probing or VNAs, you've been of tremendous help.

A special thanks to the people at Integrand Software for providing me with a license for their electromagnetic simulator, EMX. This was crucial for making the custom passive structures in this thesis.

Last, but not least: a special thanks to friends and family for keeping me sane during this work.

Thanks,
Torleif Skår

Abstract

IEEE 802.15.4z (UWB) is viewed as an alternative technology for the Internet-of-Things (IoT). Having matured over the last two decades, it has found its niche as a low-cost, low-power technology. Today, UWB technology is synonymous with asset tracking (RTLS) and vital sensing (radar).
As UWB devices share precious spectrum resources with existing wireless RF systems (e.g., at 5 GHz), filters ensure reliability. Low noise amplifiers (LNAs) play an important role in the RF front-end (RFFE) by providing sufficient gain to keep the system noise figure low, as well as impedance matching for maximum power transfer. Co-designed with the filter, a frequency-selective LNA is required to reject out-of-band frequencies to further enhance the sensitivity of the RFFE. In the design of these radio frequency integrated circuits (RFICs), monolithic inductors/transformers are vital components.

Contents

List of Figures

List of Tables

Chapter 1

Introduction

Since it introduction in 2002, ultra-wideband (UWB) technology has gone through several metamorphosis stages. Fast forward to 2019, and with Apple's UWB U1 chip for communications the technology got a second lease on life [1]. Samsung's Galaxy Note 20 is the first Android smartphone to feature UWB [2]. Without doubt, UWB has gained a strong foothold in the commercial space.

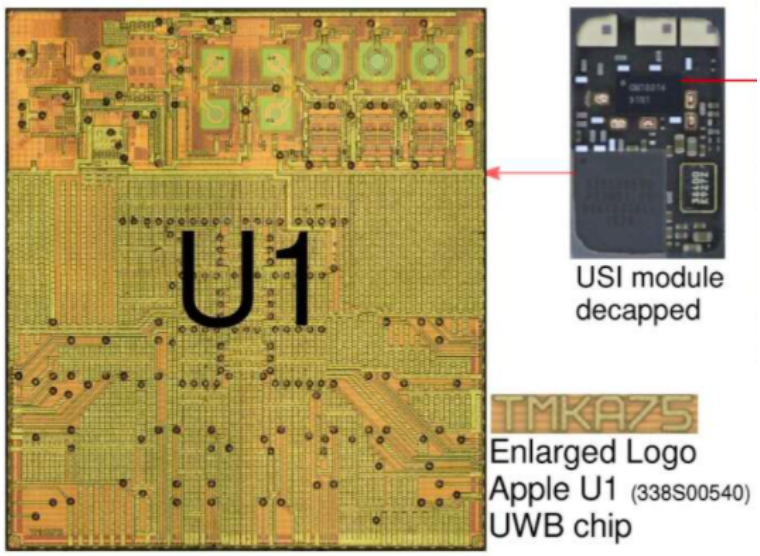

Figure 1.1: Apple's U1 UWB chip for communications [1]

Today, UWB is primarily used for real-time location systems (RTLS) and radar systems. RTLS based on UWB RF communications provides location information (mainly indoor) when GPS is unable to do so. Decawave (now Qorvo) is still at the forefront of RTLS with their CMOS 90 nm DW1000 IC. As shown in Fig. 1.2, the transceiver is based on the classical zero-IF architecture.

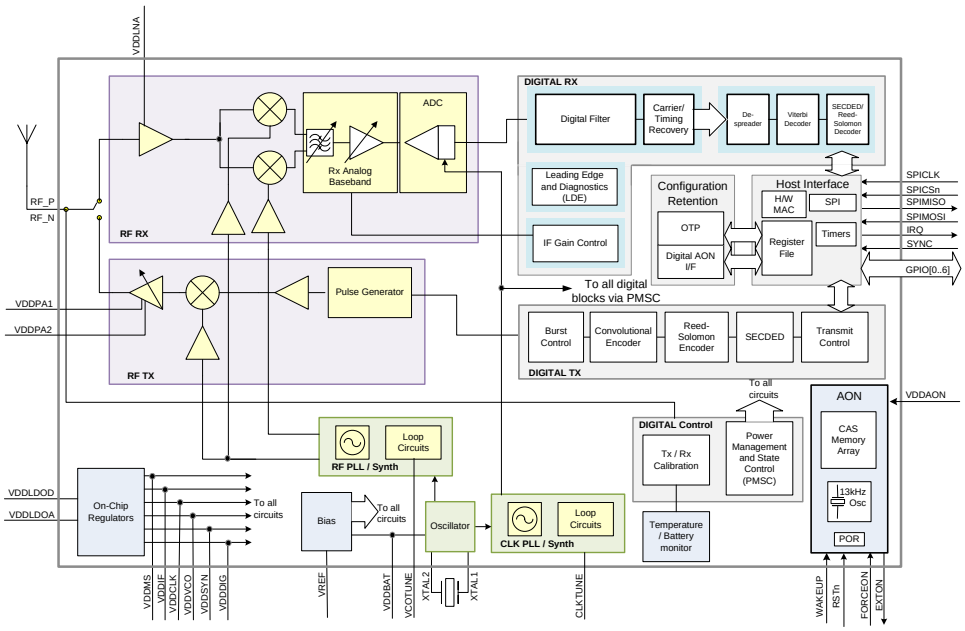

Figure 1.2: Decawave's DW1000 IC for RTLS [3]

Novelda, on the other hand has shown how to use UWB technology for radar applications with their 55 nm CMOS X4 IC. This UWB human presence sensor (see figure below) measures vital signs, such as breathing, and will be integrated into Lenovo's flagship laptop, the ThinkPad X1 Nano [4].

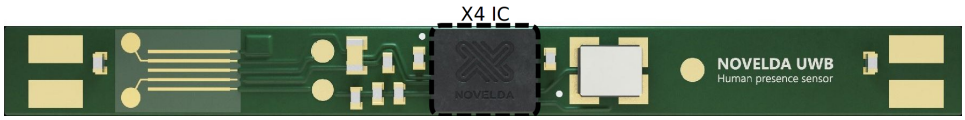

Figure 1.3: Novelda's human presence sensor based on the X4 CMOS IC [4]

The 2-port, full-duplex transceiver is based on the direct-RF sampling architecture (see Fig. 1.4a). Direct-RF sampling reduces the complexity of RF front-ends (RFFE) and simplifies analog filtering requirements. The receiver bandwidth is from 6.1-10.5 GHz.

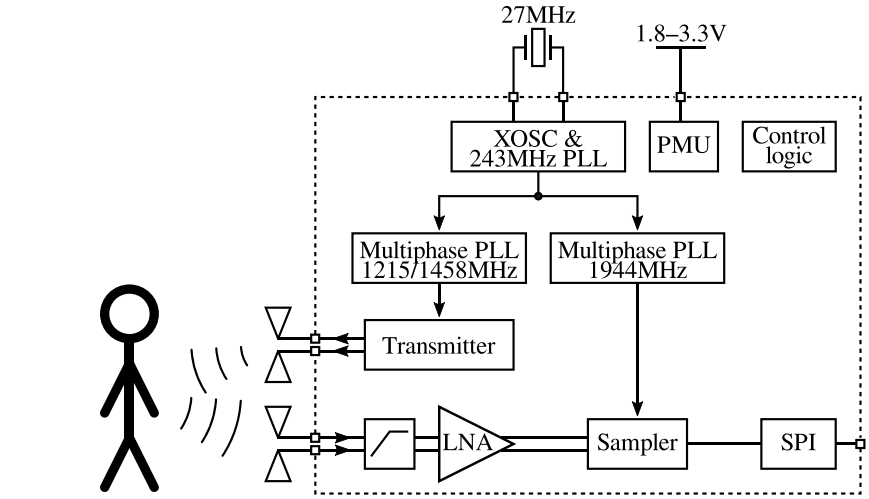

(a) Block diagram of Novelda's direct-RF UWB transceiver in 55 nm CMOS

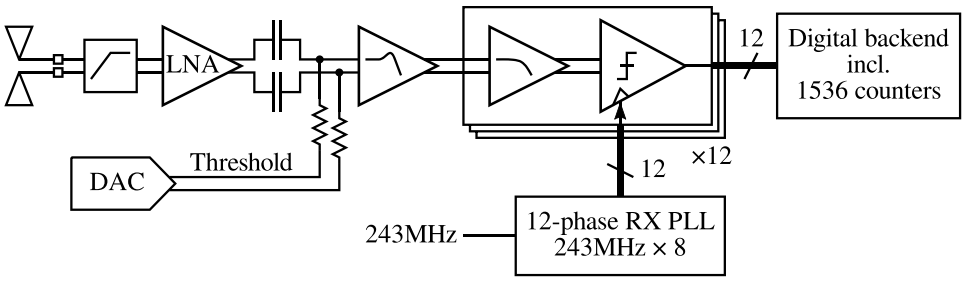

(b) Block diagram of the direct-RFFE comprising signal conditioning (filtering) via HPF, amplification via frequency-selective LNA and a high-speed +(29 GHz) ADC

Figure 1.4: Block diagrams of the Novelda X4 IC [5]

In Fig. 1.4b, the high-pass filter removes interferers from the 5 GHz-band and is the 1st block in the receiver chain. The circuit of the Q-boosted HPF is shown in Fig. 1.5. The filter employs parallel LC resonance in series with the RF signal path to block out-of-band interferers. Drawback is that the signal path and the interference blocking are not orthogonal. Thus, the insertion loss of the filter > 3 dB.

We propose a double harmonic trap (DHT) HPF with series LC resonance (for out-of-band interferers) that is orthogonal to the RF signal path. This reduces the insertion loss to below 3 dB.

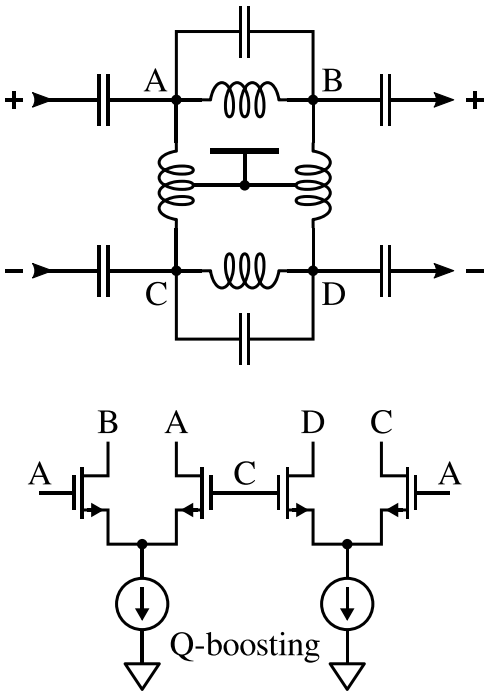

Figure 1.5: HPF with Q-enhancement [5]

For a single-ended antenna, we propose an area efficient single-ended to differential HPF with an 'embedded' on-chip balun. This is a single harmonic trap filter.

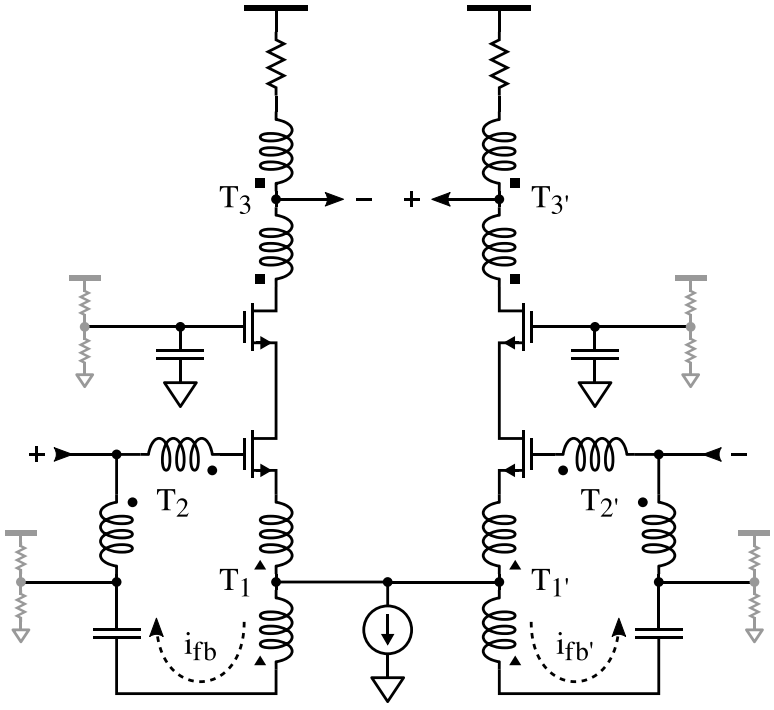

Figure 1.6: Wideband LNA [5]

In Fig. 1.6, the LNA comprise reactive feedforward (for passive voltage boosting) and negative feedback (for wideband impedance matching) loops via two asymmetrical uncoupled auto-transformers. The voltage at the

gate of the common-source stage is nearly 2× the input voltage. This g_m-boosted wideband LNA has a peak gain of 14.7 dB at 7.29 GHz.

We propose a current reuse reactively tuned pseudo-differential LNA based on Fig. 1.6 with an additional common-gate stage for higher reverse isolation.

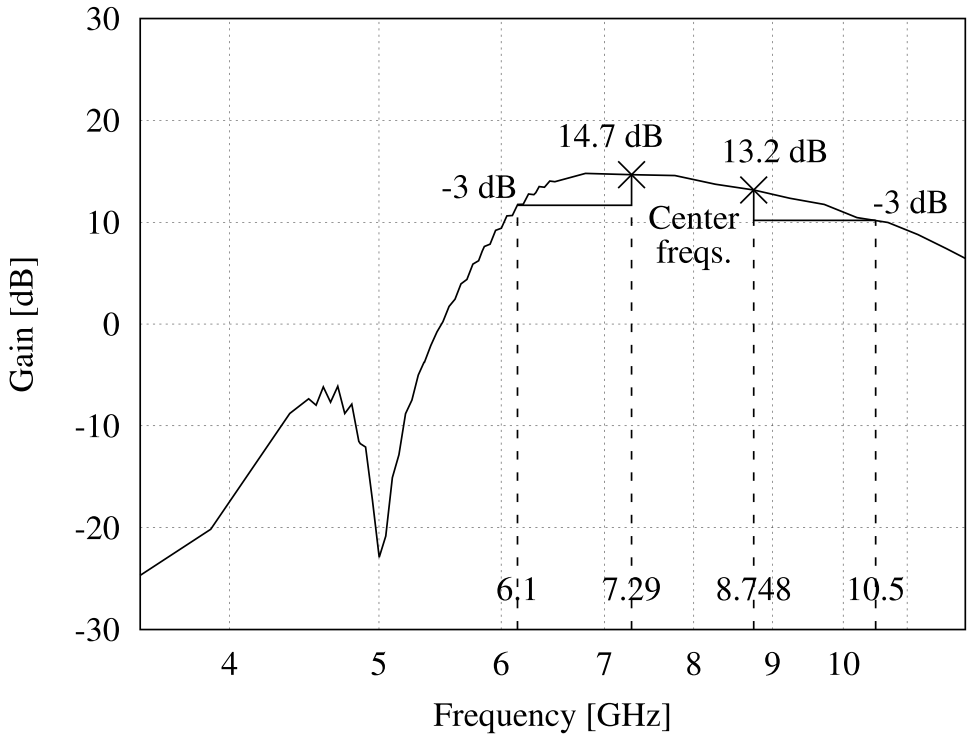

Figure 1.7: Measured RF front-end gain of the HPF, LNA and pre-amplifier stages (buffers) [5]

We know that the full-duplex doubles the spectral capacity compared to half-duplex. Ferrite circulators employed for full-duplex mode are bulky and cannot be integrated on-chip. Magnetic-free circulators are becoming more and more attractive because of their small form factors and CMOS compatibility. For example, an active 2-port full-duplex bi-directional frequency converter (BDFC) is shown in Fig. 1.8. It achieves +25 dB TX-ANT/ANT-RX isolation with an insertion loss of only 3 dB. One major drawback is its 48 mW power consumption.

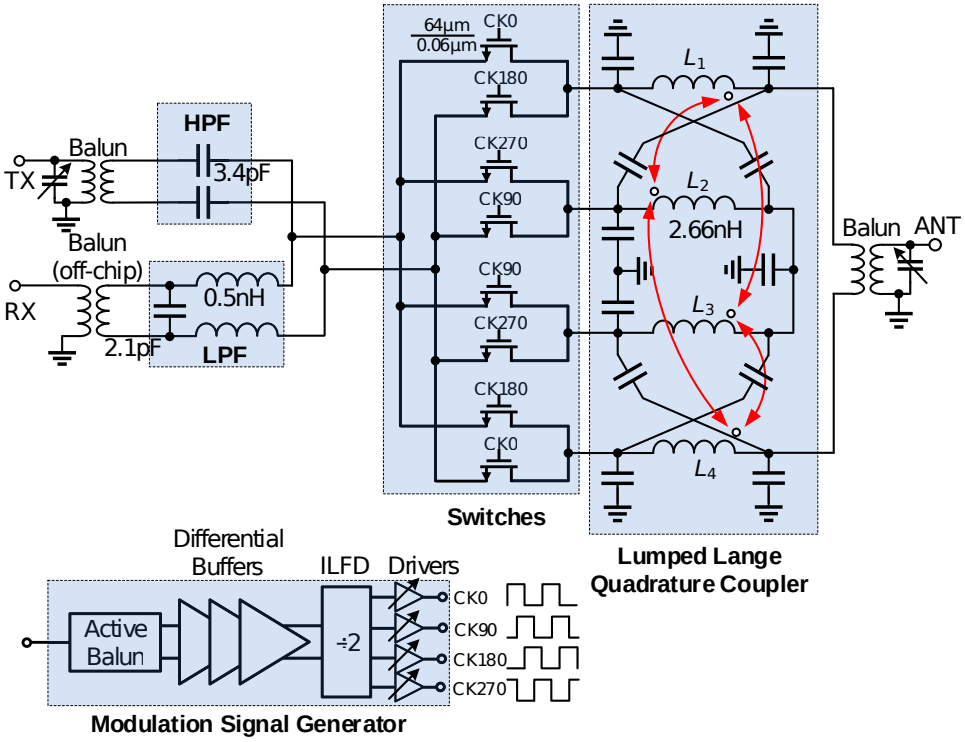

Figure 1.8: Full schematic of the BDFC-based front-end [6]

This work

Operating a differential 1-port UWB radar in full-duplex mode is most desirable as it would allow for single-antenna usage. This work presents two improved RF front-ends. Based on [5], the first of the two is a 1-port 'passively reconfigurable' RFFE, i.e. half-duplex operation in differential mode, and full-duplex operation in single-ended mode, see Fig. 1.9. Unlike [6], where the authors use 48 mA for FD-mode, we passively configure the RFFE from HD to FD.

The second design focuses on an area efficient single-ended to differential front-end. The area efficient HPF trades-off performance (insertion loss), yet the noise of the combined RFFE is $\ll 10\,\mathrm{dB}$.

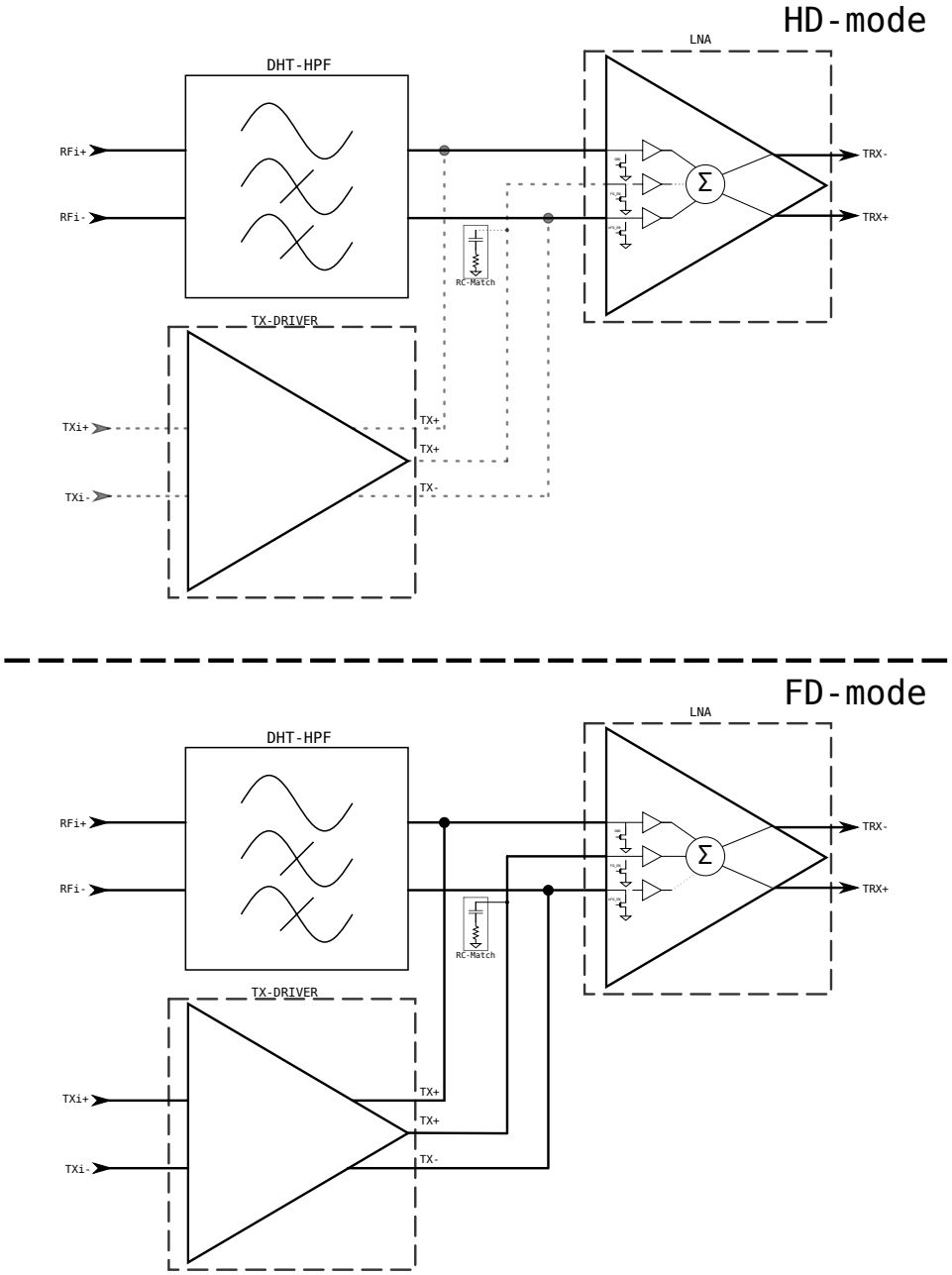

Figure 1.9: Block diagram of full-duplex single-ended RFFE

Outline

In this thesis, we propose two passive high-pass filters (HPF) in Chapter 2, a wideband reactive low-noise amplifier (LNA) in Chapter 3, a 'passively reconfigurable' RF front-end (RFFE) and an area efficient RFFE comprising said components in Chapter 4. Measurement results are presented in Chapter 5. Conclusions are drawn in Chapter 6.

Chapter 2

High-Pass Filter Design

2.1 Introduction

In Table 2.1 we present a list of the specifications we'll deisgn and optimize for throughout this chapter.

Table 2.1: Typical filter design specifications

Specification	Units
Pass-/Stop-band frequency	Hz
Passband ripple	dB
Stopband attenuation	dB

Filters can be divided into 3 categories: active, passive and active *plus* passive (hybrid).
As the name suggests, active filters comprise active devices. Even with small form factors, very high frequency (UWB) RF front-ends rarely use 'purely' active filter because of the high power consumption and noise associated with them. *gm-C* active filters using negative feedback OTAs are commonly used in narrowband receivers [7]. For example, high-Q band-pass or band-select *gm-C* are used for selecting 20 MHz channels at 2.4 GHz.
Passive filters rely solely on passive components and are split in 4 groups: resistors & capacitors (RC), resistors & inductors (RL), inductors & capacitors (LC) and resistors, inductors & capacitors (RLC).
Series and parallel inductor-capacitor configurations offer frequency selectivity, and unlike resistors, do not add noise, thus making them attractive. However, inductors fall into the category of big body structures. Designers must find a compromise between die area and the (unloaded) Q-factor, with the latter directly affecting frequency selectivity, insertion loss and/or noise figure.
Hybrid filters can be defined as being either active or passive with complementary passive or active circuits for performance boosting. An example being an LC resonant tank with Q-enhancement/boosting via a cross-coupled pair.

Filter responses can be low-pass, high-pass, band-stop & band-pass, or a combination of the aforementioned. In the congested RF spectrum, we must be able to clearly distinguish and select band(s) of interest. Thus, it is desirable to have a filter with a brick-wall like frequency response. As this is not physically realizable, it is paramount to choose a filter type with the steepest passband to stop-band transition.
For the unlicensed UWB spectrum stretching from 6-10 GHz, a band-pass or a high-pass filter [5] is the 1^{st} component in the receiver chain. As there are no known interferers above 10 GHz, we will design passive LC high-pass filters in submicron CMOS with 1 ultra-thick-metal layer (UTM).
Passive filter topologies to choose from are:

Table 2.2: Passive filter network topologies. Derived from [7, 8].

Filter Topology	Characteristics
Butterworth	Passband response with maximal flatness
Chebyshev	Steeper transition from pass-to-stopband; larger phase (w.r.t. Butterworth). Ripple in pass-band (type I) or stop-band (type II).
Elliptic	Ripple in pass and stopband, transmission zeros; steeper transition from pass-to-stopband; larger phase distortion (w.r.t. Chebychev).
Bessel	Constant group delay (w.r.t. Butterworth); less steep transition from pass-to-stopband (w.r.t. Chebyshev).

2.2 Order

The order of the filter affects the stop-band attenuation, how steep the roll-off is, and the out-of-band & in-band ripple of the filter response.
Off-chip filters maximize the order to meet the specifications for stop-band attenuation and roll-off. However on-chip inductors are big body structures, hence we're physically limited in terms of the order of the filter.
Once the order of the filter is chosen, we can improve out-of-band rejection by creating notches. Two adjacent notches can create a wideband notch ($\geq$ 1 GHz). The notches are realized using parallel or series inductors and capacitors, which give us either an open or a short at the resonance frequency.
Keeping in mind the insertion loss and area, a 7^{th}-order filter will be our upper limit. The minimum order is based on the requirements of the filter response itself. The required order of the filter will be a trade-off between stop-band atteunation & roll-off, versus area.

For maximum roll-off and fastest transition between pass-band and stop-band, the elliptical topology will be used as a baseline for the filter implementation. The drawback with the elliptical topology is the in-band ripple as opposed to Chebychev type II, with only out-of-band ripple. However due to the broadband nature of the signal of interest we assume that the in-band ripple is negligible.

2.3 Center-frequency, cut-off frequency & passband

The unlicensed UWB frequency spectrum strecthes from 3.1-10 GHz, we select a specific band withing this range. It can be subdivided into smaller bands, e.g. 3-5 GHz and 6-10 GHz to avoid 5 GHz interferers/blockers. For this work, we will be focusing on the 6-10 GHz band.
Another factor that determines the center frequency is the frequency spectrum regulations. To be 'worldwide' compliant, a center frequency of 7.875 GHz is chosen.
The bandwidth is a systems level specification. Based on the transmitted pulse spectrum, the -10 dB-bandwidth is 1 GHz. the cut-off frequency & the passband of the high-pass filter is derived from the system BW.

2.4 Specifications

Based on the previous discussions, we will decide the specifications for our passive LC HPF with harmonic traps.
As aforementioned, we want high stop-band attenuation and steep roll-off to attenuate most of the out-of-band. Dual harmonic traps create a wideband notch to supress the adjacent 5 GHz-band RF-blockers.
As a trade-off between attenuation and area, it is desiablre to have a out-of-band attenuation $\geq$ 20 dB for frequencies below 5 GHz. To relax the requirements wrt. the order of the filter, an attenuation of 15 dB at 5.8 GHz is sufficient. The specification for attenuation is:

$$\begin{aligned} |S_{21}|_{DHT} &= \begin{cases} \geq 15\,\text{dB}, f = 5.8\,\text{GHz} \\ \geq 20\,\text{dB}, f \leq 5.0\,\text{GHz} \end{cases} \\ |S_{21}|_{SHT} &= \begin{cases} \geq 15\,\text{dB}, f = 5.8\,\text{GHz} \\ \geq 15\,\text{dB}, f \leq 5.0\,\text{GHz} \end{cases} \end{aligned} \tag{2.1}$$

The -3 dB-passband is equal to the -10 dB-bandwidth, i.e. 1 GHz around the center frequency. We then have the filter passband defined as:

$$\text{Passband } = f_c \pm \frac{BW}{2} = 7.875\,\text{GHz} \pm 500\,\text{MHz}. \tag{2.2}$$

This gives a passband in the range:

$$\text{Passband } \in [7.375\,\text{GHz},\ 8.375\,\text{GHz}]\,, \tag{2.3}$$

where the lower boundary of 7.375 GHz sets the filter -3 dB *cut-off frequency* as well.
The maximum order is set to 7. The minimum order is determined from the required stop-band attenuation, roll-off, cut-off frequency, and area. An LC filter synthesizer, sets our minimum order based on the design specifications to be 5.
For maximum power transfer, we want to be impedance matched [9]. Given the passive LC filter implementation, one expects the filter to be of a *transparent* nature when impedance matched. Transparency lets the input impedance of the RF-receiver be determined by the suceeding block. The condition for being impedance matched is given by the maximum power transfer theorem, which states impedance matching when [9]:

$$Z_{filter} = Z_{ant}^{*}, \tag{2.4}$$

where Z_{filter} is the input impedance looking into the filter, and Z_{ant}^{*} is the complex conjugate of the characteristic impedance of the antenna.
To quantify impedance matching, the reflected wave power should not be higher than 10% of the incident wave power [10]. In terms of S-parameters one is impedance matched under the condition:

$$S_{11} \leq -10\,\text{dB}, \tag{2.5}$$

For $< 1\%$ power reflected, $S_{11} \leq -20$ dB. This our wanted specification. In terms of S-parameters, we define the NF & IL requirement as:

$$\text{NF} \ = \text{IL} \ = \begin{cases} |S_{21}|_{DHT} \leq 3\,\text{dB}, \\ |S_{21}|_{SHT} \leq 4\,\text{dB}. \end{cases} \tag{2.6}$$

2.5 DHT filter: pseudo-differential to pseudo-differential

Design specifications for the PD-PD DHT elliptic filter are shown in Table 2.3.
The series-first capacitance was removed due to it providing little to no performance gain, nor do we need DC isolation between the antenna and the filter, hence it was removed. The removal of this capacitance make the order of the filter to 4.
The motivation behind the realization of a pseudo-differential to pseudo-differntial (PDPD) filter is to use the filter in a differential, as well as in a single-ended manner. This is a filter to be used for a pseudo full-duplex system, where we switch between single-ended and differential-mode.
From Fig. 2.1, we see two notches, $C_1 + L_1$ & $C_3 + L_2$, in combination with the series capacitances C_2 & C_4. These reactances realizes a 4^{th}-order filter implementation.
The PDPD filter was built in a half-circuit manner, being symmetrical along the signal-path on both the positive and negative inputs. Looking at the half-circuit inductors, L_1 & L_2, we see that they're implemented

Table 2.3: Target specifications for the passive elliptic LC-filter with dual-harmonic traps

Parameter	Design specification
Type	HPF w/DHT
Order	4^{th}
Passband	7.375-8.375 GHz
Stopband	$\leq 5.8\,\text{GHz}$
Stopband attenuation: $f = 5.8\,\text{GHz}$ $f \leq 5.0\,\text{GHz}$	 $\geq 15\,\text{dB}$ $\geq 20\,\text{dB}$
IL & NF	$\leq 3\,\text{dB}$
S_{11}	$\leq -20\,\text{dB}$

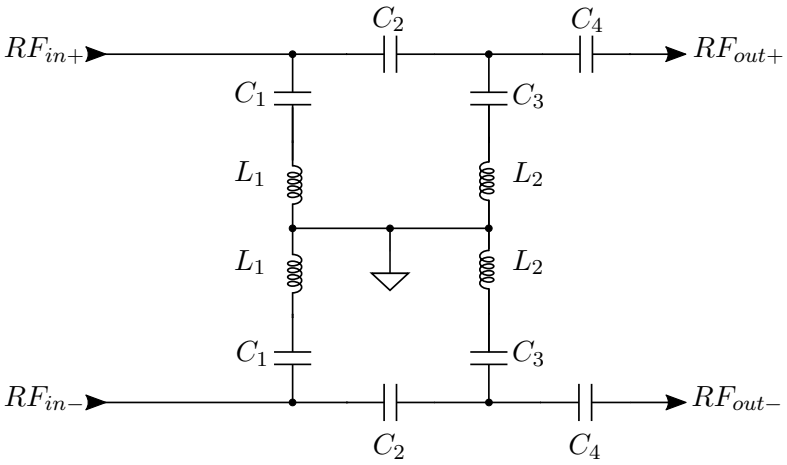

Figure 2.1: Schematic for the PDPD-Filter

Table 2.4: Component parameters

Name	Reactance	Q_f *	SRF [GHz]
C_1	710 fF	45.5	61.4
C_2	470 fF	67.1	76.3
C_3	510 fF	63	73.6
C_4	1 pF	32.5	51.3
L_1	1.58 nH	14.6	23.7
L_2	1.58 nH	14.6	23.7

* @ 5.8 GHz

as single-ended inductors. Using these single-ended inductors allows us to short one half of the circuit, without affecting the inductance on the other

half.
The inductors form a pseudo-differential topology. Realizing these inductors as center-tapped inductors as opposed to single-ended inductors would increase the common-mode rejection ratio (CMRR) of the filter.
The center-tapped inductor would trade-off the half-circuit functionality & higher Q_f for reduced area.
To attenuate the 5 GHz-band, we use a DHT filter. Notches are realized with series LC resonance. The two notches create a wideband notch. The two notches are realized by the reactances: $C_1 + L_1$ & $C_3 + L_2$.

Table 2.5: LC resonator parameters for the PDPD-filter

Components	Notch frequency [GHz]	Q_f *
C_1 & L_1	4.8	11.6
C_3 & L_2	5.6	12

* @ notch frequency

The physical realization the schematic, Fig. 2.1, was done in the following manner:

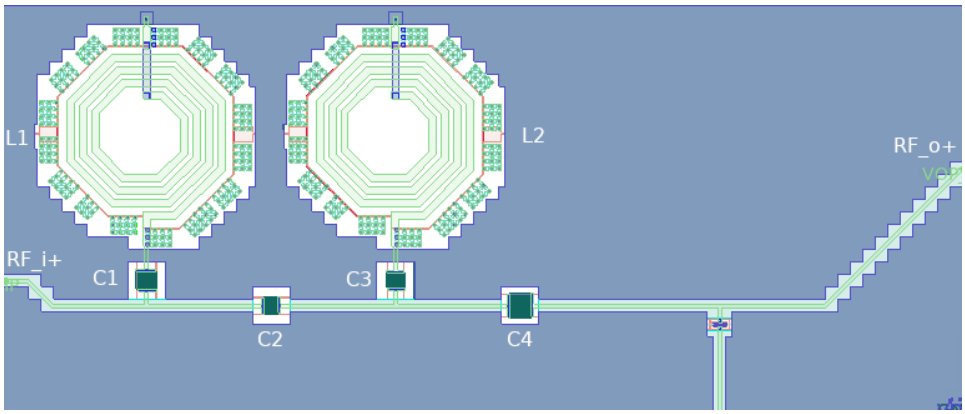

Figure 2.2: Half-circuit layout for the PDPD-Filter

The PDPD is realized in a half-circuit manner, where the filter is symmetrical along the X-axis. The symmetry is done to maximize the CMRR of the filter.
UTM has the lowest sheet resistance, and is thus sued for all RF routing, which minimizes the insertion loss.
The passive structures were realized using TSMC's scalable symmetrical center tapped inductors (`spiral_std_sym_ct_mu_z`) & scalable capacitors (`crtmom_rf`).

2.5.1 Simulation results

The input impedance matching (S_{11}) of the SEDE filter, shows how well matched the filter is to 100 Ω source. The worst case matching is in

the upper frequency of the passband, and is: $S_{11,max} = -13.92\,\text{dB}$ at 8.375 GHz.
The minimum required matched bandwidth is: $S_{11} \leq -10\,\text{dB}$ in the range 6.1-9.3 GHz.
The recommended matched bandwidth is: $S_{11} \leq -20\,\text{dB}$ in the range 6.5-7.7 GHz.
From S_{11}, we see that the matched bandwidth is skewed towards the lower frequencies, and not centered around the center frequency of 7.875 GHz. This frequency offset is most likely due to additional parasitic capacitance.

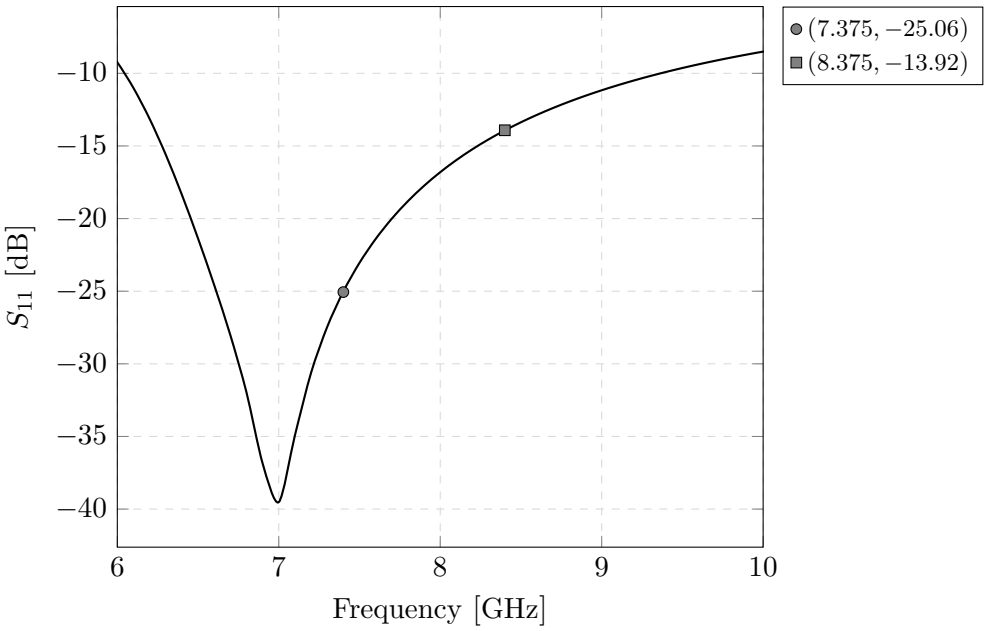

Figure 2.3: S_{11} for the PDPD elliptic filter.

The worst case output impedance matching (S_{22}) is at the lower frequency of the passband, and is: $S_{22,max} = -10.42\,\text{dB}$ at 7.375 GHz.The minimum required matched bandwidth is: $S_{22} \leq -10\,\text{dB}$ in the range 6.4-8.5 GHz.
The recommended bandwidth, where the return loss is less or equal to 1% of the input signal, is not achieved for the output impedance matching. This filter is not to be used standalone, thus the output return loss is not of concern.
The IL & NF was simulated by using a differential source of $100\,\Omega$, while loading it with a differential load of $100\,\Omega$. The worst case IL & NF is shown to be in the lower frequency of the passband, i.e. at the cut-off frequency of the filter. The worst case scenario can be shown to be:

$$\begin{aligned} IL_{max} &= 2.51\,\text{dB},\ f = 7.375\,\text{GHz} \\ NF_{max} &= 2.35\,\text{dB},\ f = 7.375\,\text{GHz} \end{aligned} \tag{2.7}$$

In terms of bandwidth, we cover the IL & NF requirements in a

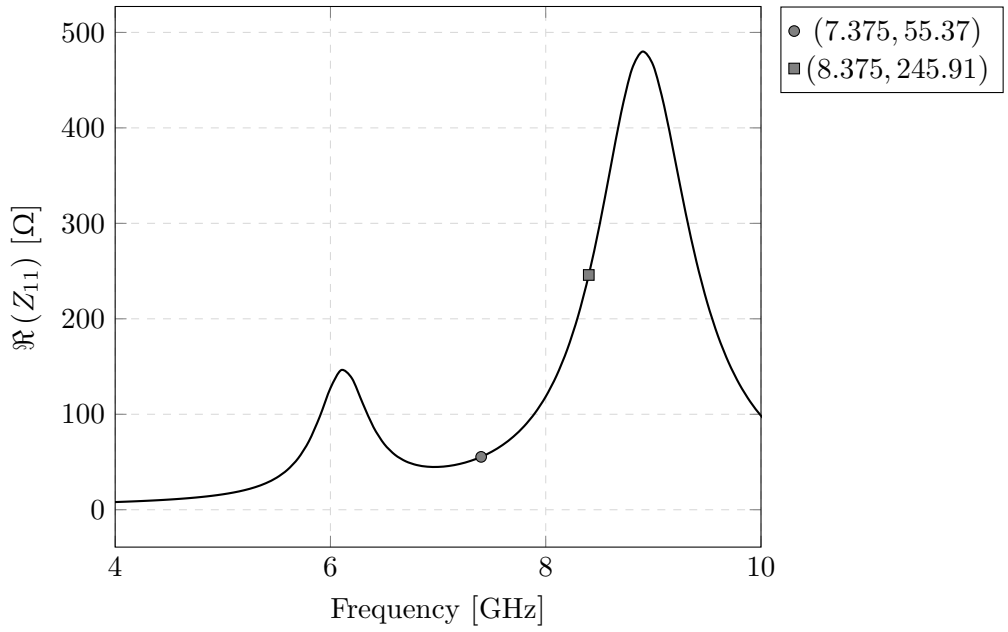

Figure 2.4: Real input impedance of the PDPD elliptic filter.

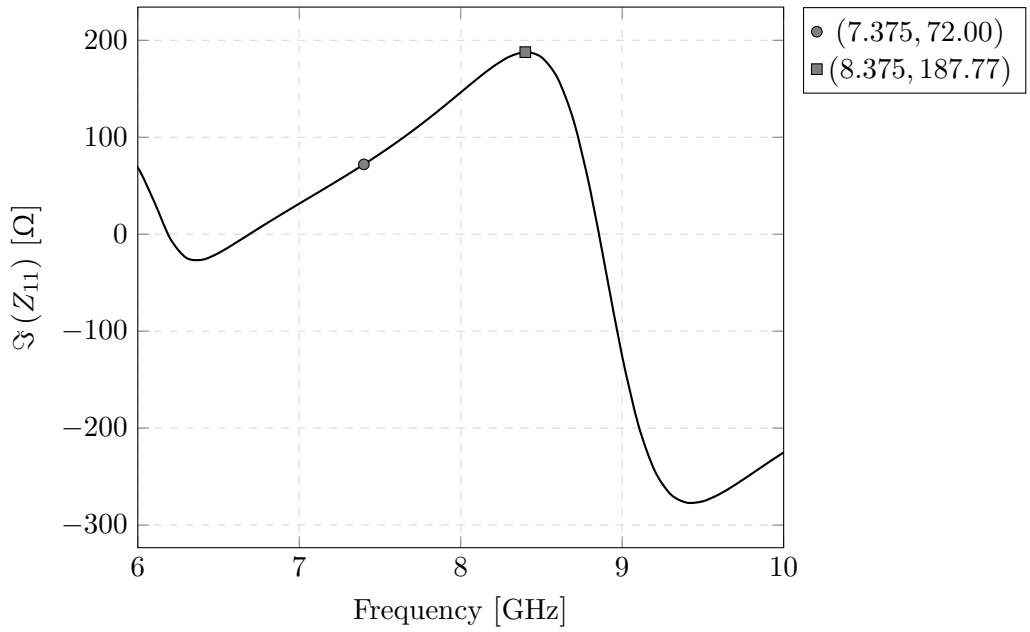

Figure 2.5: Imaginary input impedance of the PDPD elliptic filter.

bandwidth of:

$$\begin{aligned} IL &\leq 3\,\text{dB},\ f \in [7,\ 12]\,\text{GHz} \\ NF &\leq 3\,\text{dB},\ f \in [7,\ 12]\,\text{GHz} \end{aligned} \tag{2.8}$$

In the scenario of not being completely transparent, i.e. impedance

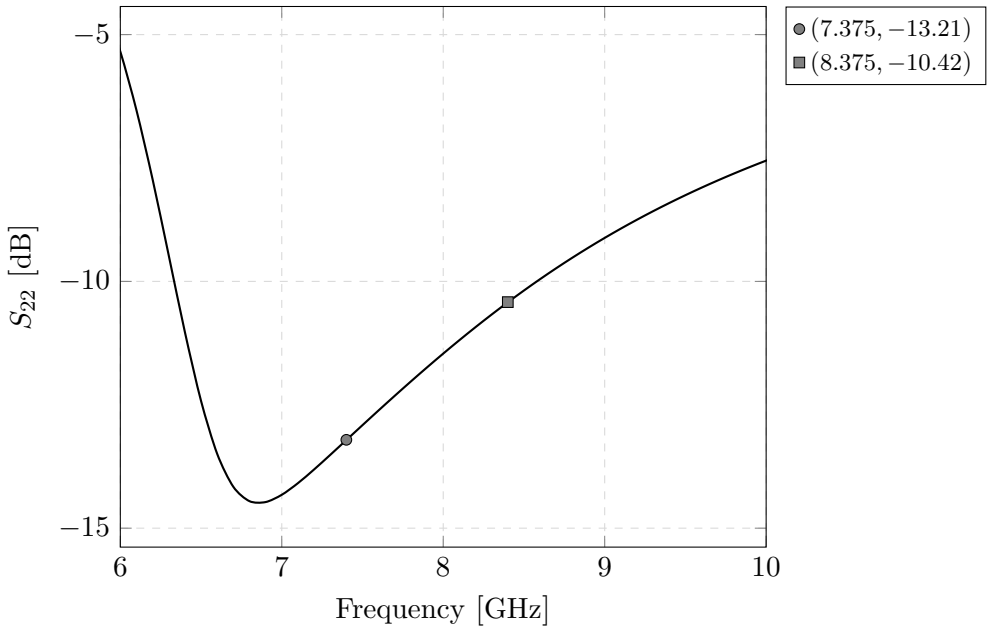

Figure 2.6: S_{22} for the PDPD elliptic filter.

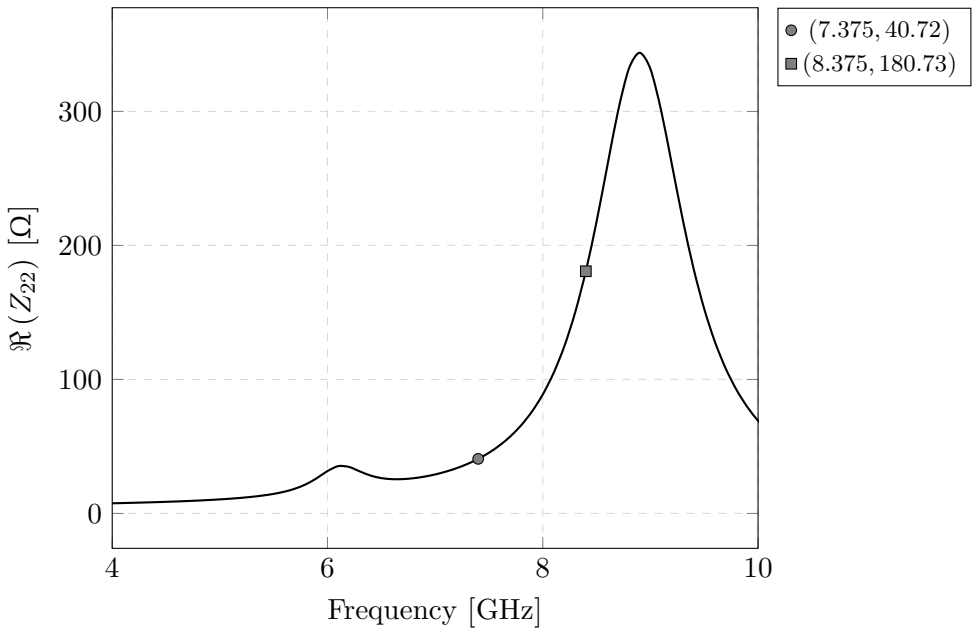

Figure 2.7: Real output impedance of PDPD elliptic filter.

mismatch, we expect that the IL is larger than the NF. Which is seen in the PDPD-filter realization.

Looking at the filter rejection, we find the attenuation at the bands of

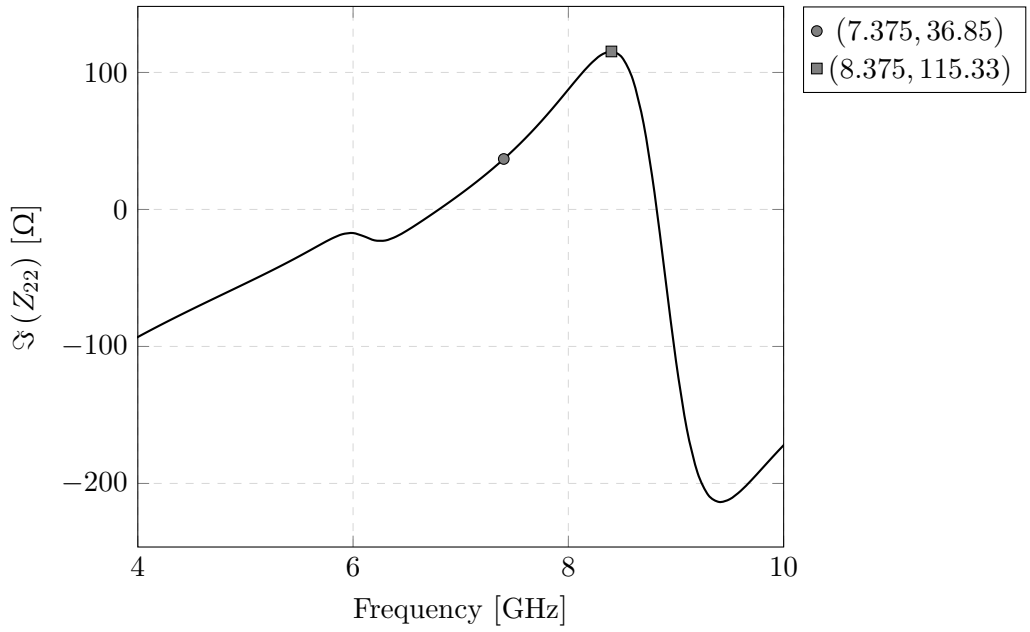

Figure 2.8: Imaginary output impedance of PDPD elliptic filter.

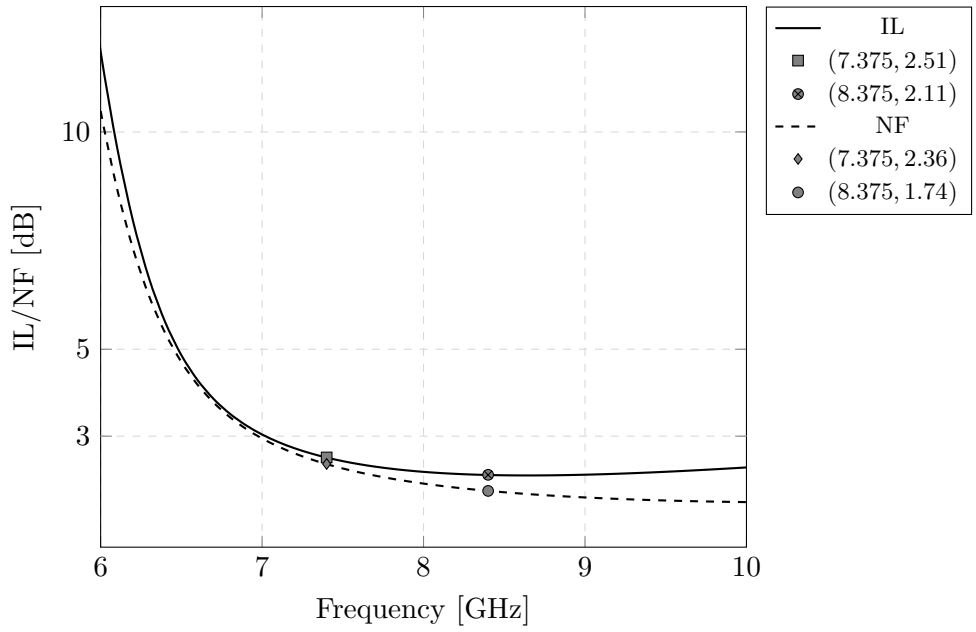

Figure 2.9: Insertion loss & NF from the PDPD elliptical filter.

interest to be:

$$\text{Rejection} = \begin{cases} \geq 14\,\text{dB}, \;\; f \in [0, 2.4]\,\text{GHz}, \\ \geq 20\,\text{dB}, \;\; f \in [3.8, 5.4]\,\text{GHz}, \\ 17.32\,\text{dB}, \;\; f = 5.8\,\text{GHz} \end{cases} \tag{2.9}$$

While the 5 GHz band is sufficiently attenuated, the attenuation at 2.4 GHz is lower than the requirement. We expect the antenna to provide additional attenuation in the 2.4 GHz. From a systems level we expect sufficient attenuation for the 2.4 GHz band.

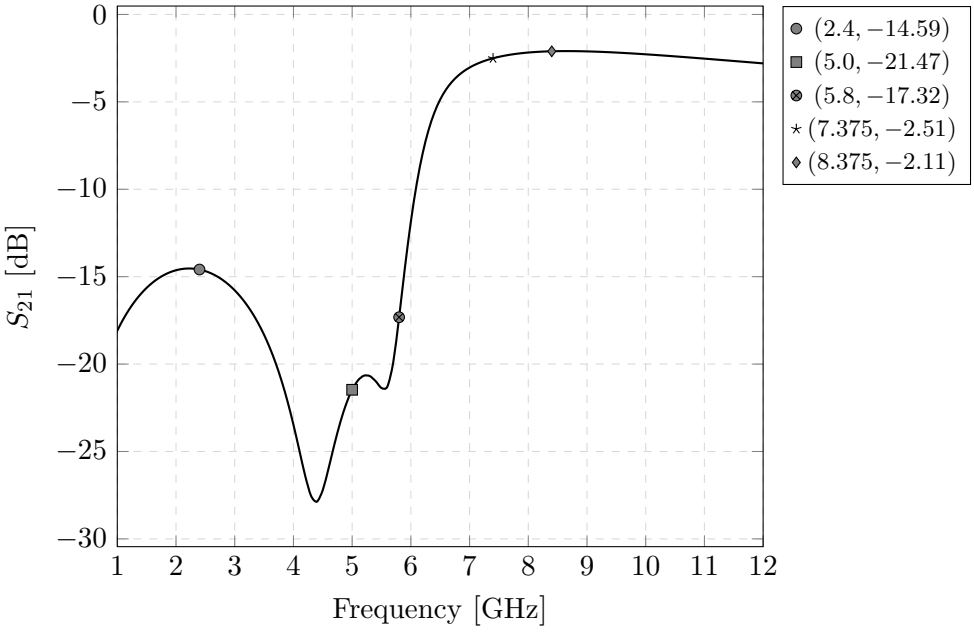

Figure 2.10: Transfer function of the PDPD elliptical filter.

The maximum group delay (GD) of the filter is in the lower frequency of the passband, and is $GD_{max} = 101.2\,\text{ps}$.
From the summary in Table 2.6, we see that the PDPD realization meets most of the design requirements.

2.6 SHT filter: single-ended to differential

Design specifications for the SE-DE SHT elliptic filter are shown in Table 2.7.
The series-first capacitance was removed due to it providing little to no performance gain, nor do we need DC isolation between the antenna and the filter, hence it was removed. The removal of this capacitance make the order of the filter to 4.
The single-ended to differential filter (SEDE), is realized to provide an area-optimized version of the elliptical HPF. In addition to saving area on-chip, we want to save area off-chip by using a single-antenna.
From Fig. 2.12, we see a single notch, $CT - L_1 + C_2$ in combination with the balun, T_1 and the series capacitances, C_1 & C_3. These reactances realizes a 4^{th}-order filter.

The transformer T_1 is realized as a balun, which does the single-ended to

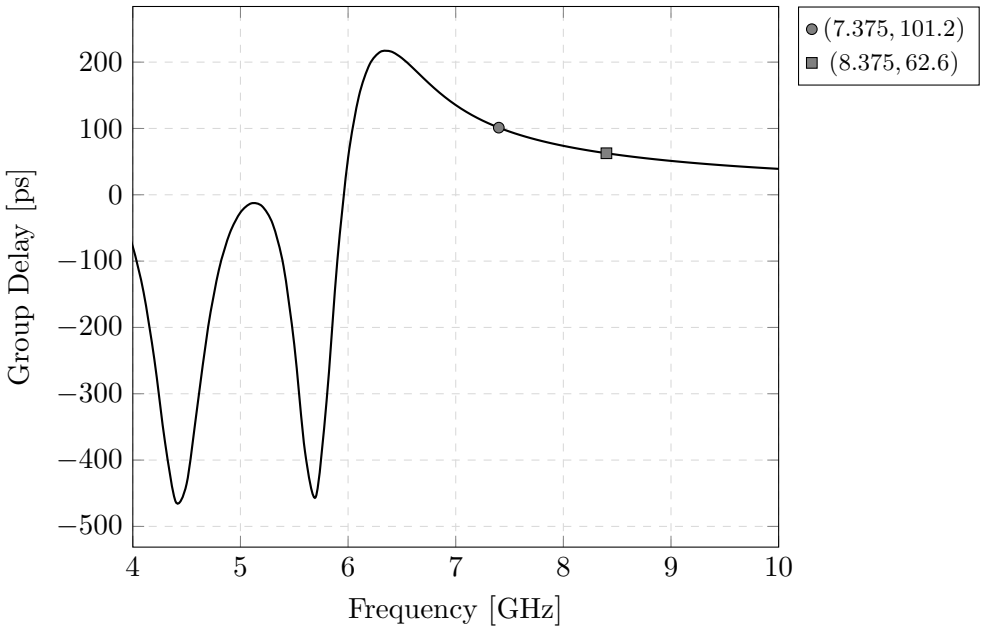

Figure 2.11: Group delay of the PDPD elliptical filter.

Table 2.6: Summary for the PDPD elliptical filter

Parameter	Implementation	Specification
IL	$\leq 2.51\,\text{dB}$	$\leq 3\,\text{dB}$
NF	$\leq 2.36\,\text{dB}$	$\leq 3\,\text{dB}$
RL:		
Minimum*	6.1-9.3 GHz	7.375-8.375 GHz
Recommended†	6.5-7.7 GHz	7.375-8.375 GHz
RL_O:		
Minimum‡	6.4-8.5 GHz	7.375-8.375 GHz
Recommended§	N/A	7.375-8.375 GHz
Rejection:		
@ 2.4 GHz	14.59 dB	$\geq 20\,\text{dB}$
@ 5.0 GHz	21.4 dB	$\geq 20\,\text{dB}$
@ 5.8 GHz	17.32 dB	$\geq 15\,\text{dB}$
GD	$\leq 101.2\,\text{ps}$	N/A

* $S_{11} \leq -10\,\text{dB}$
† $S_{11} \leq -20\,\text{dB}$
‡ $S_{22} \leq -10\,\text{dB}$
§ $S_{22} \leq -20\,\text{dB}$

differential conversion through impedance transformation. We know that

Table 2.7: Target specifications for the passive elliptic LC-filter with a signle-harmonic trap

Parameter	Design specification
Type	HPF w/SHT
Order	4^{th}
Passband	7.375-8.375 GHz
Stopband	≤ 5.8 GHz
Stopband attenuation:	
$f = 5.8$ GHz	> 15 dB
$f \leq 5.0$ GHz	> 15 dB
IL & NF	≤ 4 dB
S_{11}	≤ -20 dB

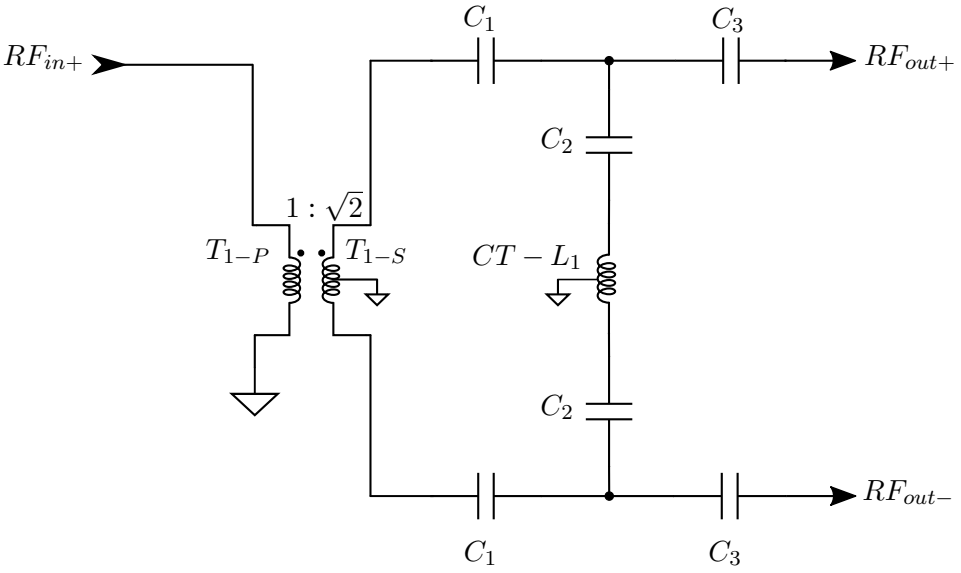

Figure 2.12: Schematic for the SEDE elliptic filter

Table 2.8: Component parameters for the SEDE elliptic filter

Name	Reactance	Q_f *	SRF [GHz]
C_1	350 fF	88.1	89.1
C_2	575 fF	55.8	68.7
C_3	1 pF	32.5	51.3
AT_1 †)	2.7 nH	20.1	17.9

* @ 5.8 GHz

† Driven differentially

we can write the turns ratio between two windings [11]:

$$\frac{n_S}{n_P} = \frac{v_S}{v_P} = \frac{i_P}{i_S} = \sqrt{\frac{L_S}{L_P}}, \tag{2.10}$$

where n_S is the number of turns in the secondary winding, n_P is the number of turns in the primary winding, v_S, v_P is the voltage across respectively the secondary and primary windings, i_P, i_s is the current going through respectively the primary and secondary windings, and L_S, L_P is the self-inductance of respectively the secondary winding, and the primary winding.
From Eq. (2.10), we find the required impedance transformation:

$$Z_S = \left(\frac{n_S}{n_P}\right)^2 Z_P = \left(\frac{L_S}{L_P}\right) Z_P \tag{2.11}$$

.
We know that our primary winding has an impedance equal to the characteristic impedance of the antenna, which we assume is:

$$Z_P = Z_{Ant} = 50\,\Omega \tag{2.12}$$

Combining Eqs. (2.11) and (2.12), we can calculate the required turns ratio for the unbalanced to balanced tranformation of $1{:}\sqrt{2}$, or in terms of self-inductances, $L_S = 2L_P$.

Table 2.9: Component parameters of the transformer in the SEDE elliptic filter.

Name	Inductance [nH] *	Q_f *	SRF [GHz]	k
T_1	1.35 nH†	1.12	10.67	0.82
T_{1-P}	0.44 nH	4.25	> 20	N/A
T_{1-S}	0.75 nH§	4.50	> 20	N/A

* @ 7.875 GHz
† Mutual inductance between the two windings
§ Differentially driven

To minimize the on-chip area, a single harmonic trap is realized, as opposed to dual harmonic trap. The notch is realized through reactances, C_2 in series with the center-tapped inductor, $CT - L_1$. This SHT resonates at 5.7 GHz,i.e. at the upper frequency of the 5 GHz-band. In the SEDE-filter there's one additional resonator, and that's the series connection between the secondary winding of the balun, T_{1-S} and the series capacitance, C_1. To minimize insertion loss, this series resonator resonates withing the passband.
To minimize area, the notch inductor is realized using a center-tapped inductor instead of a single-ended inductor.The center-tapped inductor has a higher self-inductance due to the positive mutual inductance,

Table 2.10: LC resonator parameters for the SEDE-filter

Components	Resonance frequency [GHz]	Q_f *
$T_{1-S} + C_1$ †	6.7	3.8
$C_2 + AT_1$ §	5.7	14.8

* @ resonance frequency
† With the center-tap as input, single-ended
§ Differentially driven

when driven differentially. Assuming perfect coupling between the two windings, we estimate the self-inductance of the transfomer to be $\approx 4\times$ the inductance of a single-ended equivalent (in area) [11]. In addition, we also get an increase of Q_f when driven differentially [11].

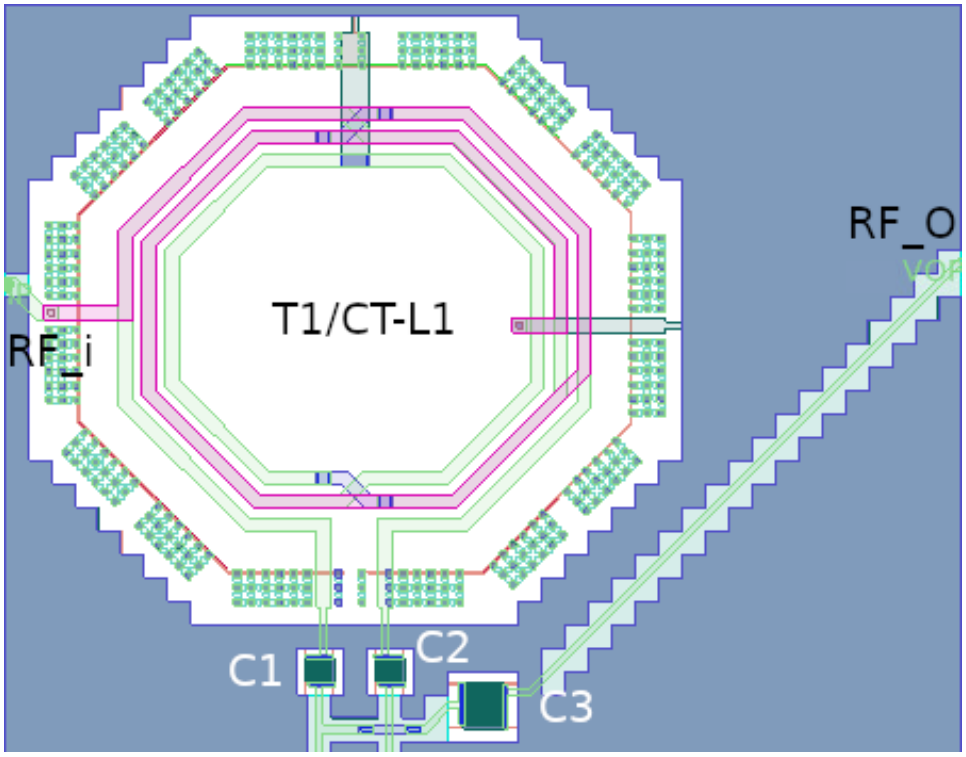

Figure 2.13: Half-circuit layout for the SEDE-Filter

The SEDE is realized in a half-circuit manner, where the filter is symmetrical along the X-axis. The symmetry is done to maximize the CMRR of the filter.
UTM has the lowest sheet resistance, and is thus sued for all RF routing, which minimizes the insertion loss.
The passive structures were realized using TSMC's scalable symmetrical center tapped inductors (`spiral_std_sym_ct_mu_z`) & scalable capacitors (`crtmom_rf`).
The balun is implemented using the foundry model for the inductor, which

is equivalent to $CT - L_1$ (see Fig. 2.12), as the secondary winding. For the primary winding we use the AP-redistribution layer which sits on top of the UTM. The stacked transformer topology is used to maximize the coupling coefficient between the primary and secondary winding [11], which in turn decreases the insertion loss of the transformer. The primary winding was offset by a distance, d, to reduce the amount of coupling capacitance between the two windings, which in turn increase the self-resonance frequency of the balun [11].

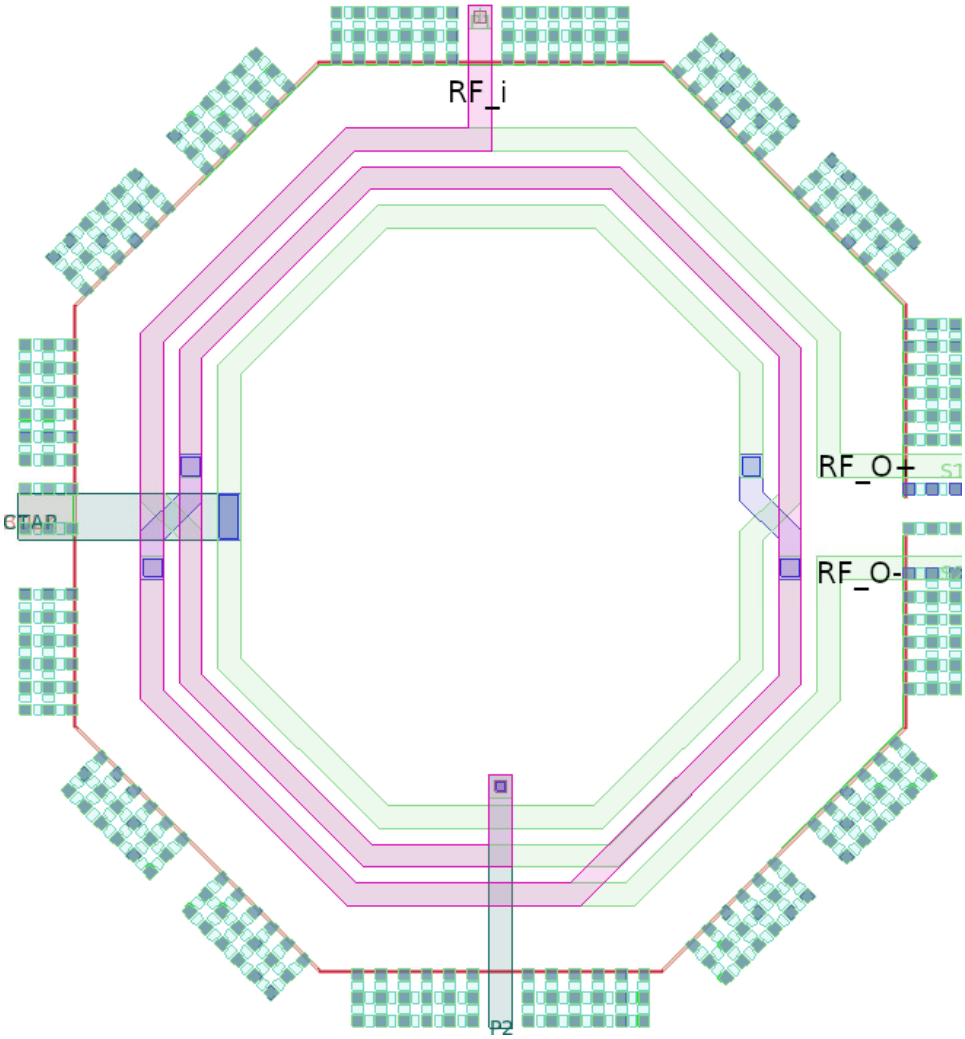

Figure 2.14: Transformer T_1 from Fig. 2.12

2.6.1 Simulation results

The input impedance matching (S_{11}) of the SEDE filter, shows how well matched the filter is to 50 Ω source. The worst case matching is in the upper frequency of the passband, and is: $S_{11,max} = -19.74\,\text{dB}$ at 8.375 GHz.

The minimum required matched bandwidth is: $S_{11} \leq -10\,\text{dB}$ in the range 6.4-12 GHz.

The recommended matched bandwidth is: $S_{11} \leq -20\,\text{dB}$ in the range 6.9-8.3 GHz.

From S_{11}, we see that the matched bandwidth is skewed towards the lower frequencies, and not centered around the center frequency of 7.875 GHz. This frequency offset is most likely due to additional parasitic capacitance.

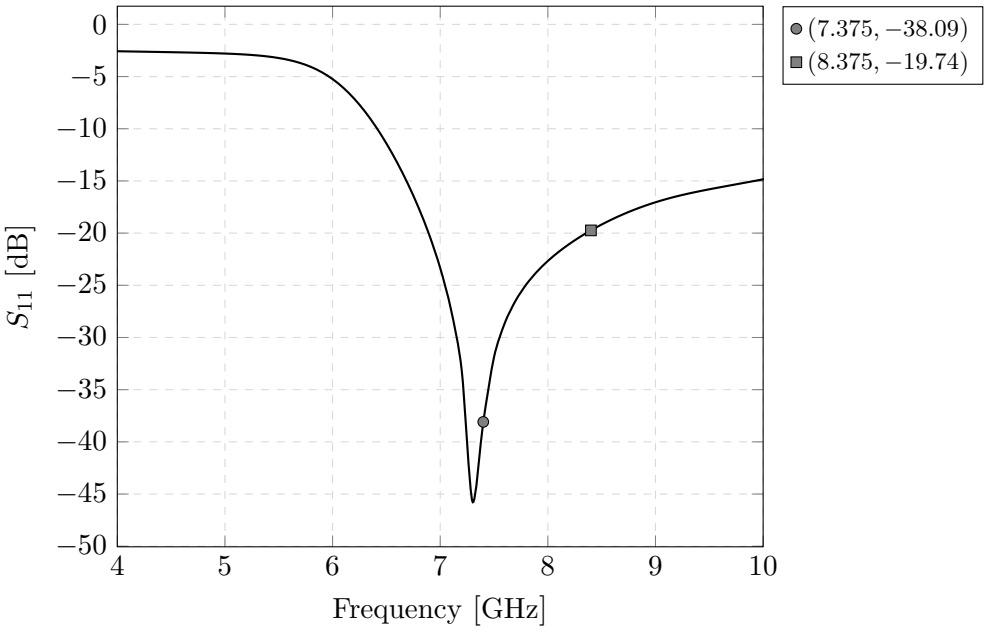

Figure 2.15: S_{11} for the SEDE elliptic filter.

The worst case output impedance matching (S_{22}) is at the lower frequency of the passband, and is: $S_{22} = -13.64\,\text{dB}$ at 7.375 GHz.

The minimum required matched bandwidth is: $S_{22} \leq -10\,\text{dB}$ in the range 7-10.8 GHz.

The recommended matched bandwidth is: $S_{22} \leq -20\,\text{dB}$ in the range 8-9 GHz.

This filter is not to be used standalone, thus the output return loss is not of concern.

The IL & NF was simulated with a single-ended $50\,\Omega$ source, and a $100\,\Omega$ differential load. The worst case IL & NF is shown to be in the lower frequency of the passband, i.e. at the cut-off frequency of the filter. The worst case scenario is:

$$\begin{aligned} IL_{max} &= 3.06\,\text{dB},\ f = 7.375\,\text{GHz} \\ NF_{max} &= 2.95\,\text{dB},\ f = 7.375\,\text{GHz} \end{aligned} \tag{2.13}$$

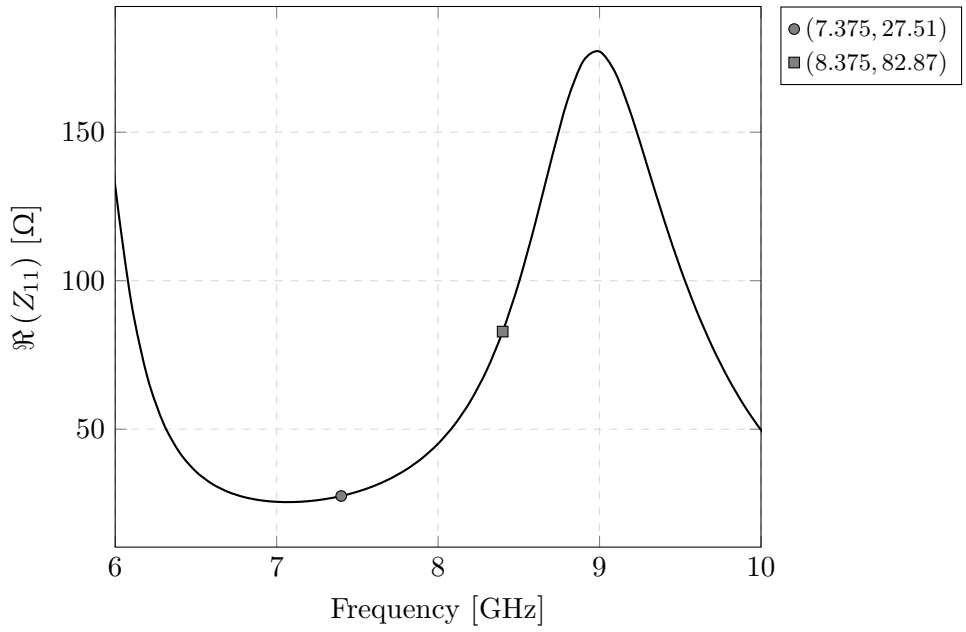

Figure 2.16: Real input impedance of the SEDE elliptic filter.

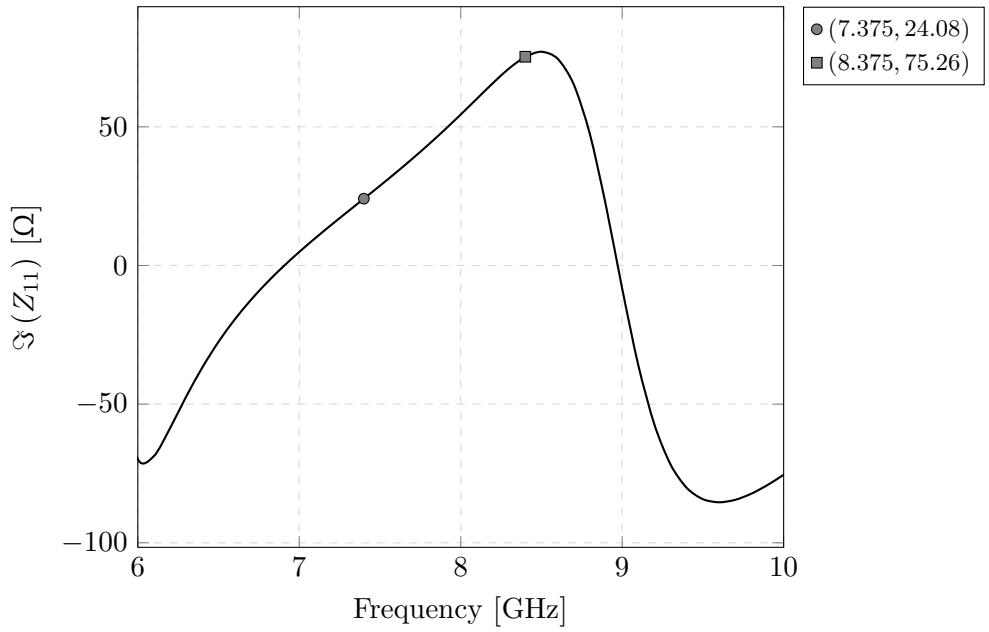

Figure 2.17: Imaginary input impedance of the SEDE elliptic filter.

We cover the IL/NF specifications over the following bands:

$$\begin{aligned} IL &\leq 3\,\text{dB},\ f \in [7.5,\ 10.3]\,\text{GHz} \\ NF &\leq 3\,\text{dB},\ f \in [7.4,\ 12]\,\text{GHz} \end{aligned} \tag{2.14}$$

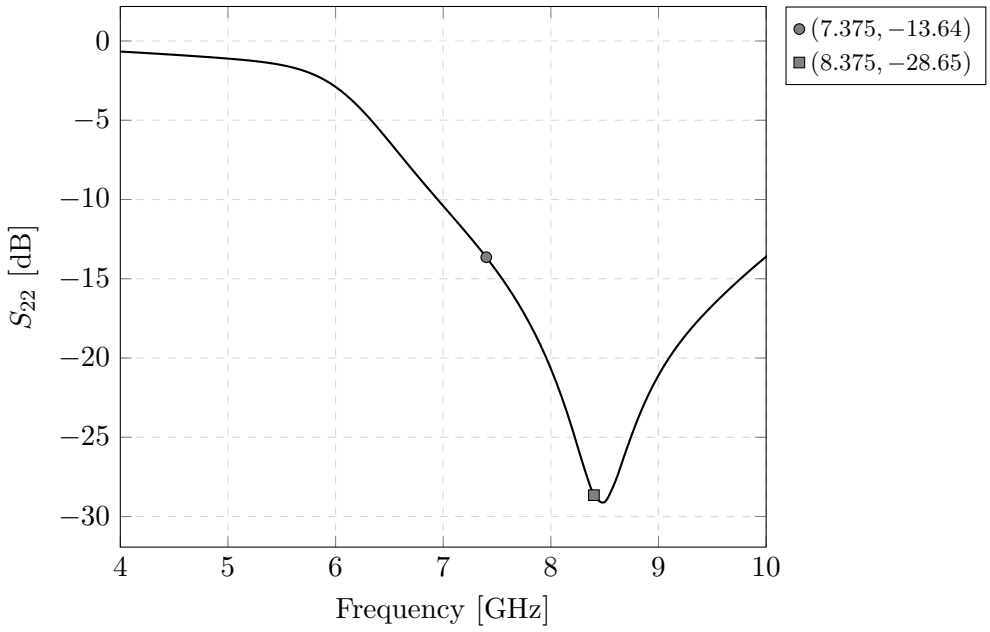

Figure 2.18: S_{22} for the SEDE elliptic filter.

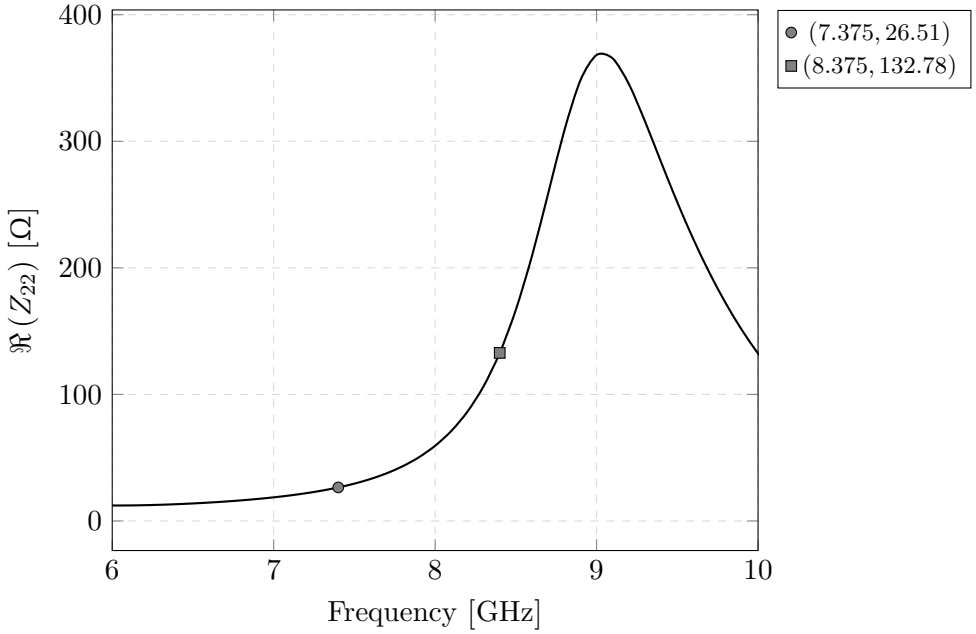

Figure 2.19: Real output impedance of SEDE elliptic filter.

If we compare the NF_{max} for the SEDE vs PDPD (see Eq. (2.7)), the SEDE filter has 0.7 dB higher NF. This added NF is due to the non-ideal coupling between the primary and secondary windings. The insertion loss

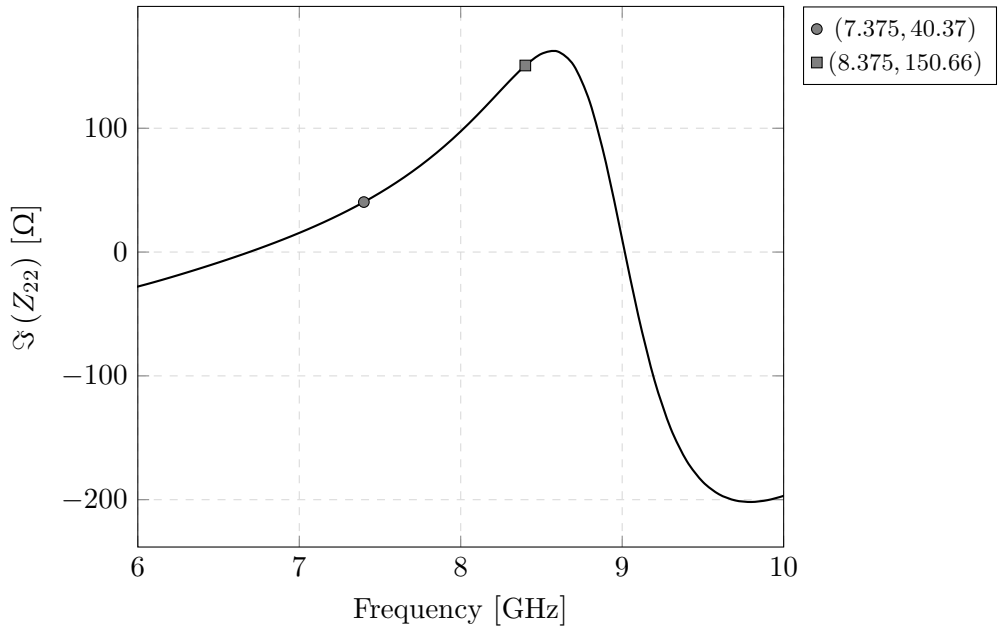

Figure 2.20: Imaginary output impedance of SEDE elliptic filter.

is approximated as:

$$IL_k = |10\log_{10}(|k|)| = |10\log_{10}(|0.82|)| \approx 0.86\,\text{dB}, \tag{2.15}$$

where k is the coupling coefficient between the primary and secondary winding in the balun (see Table 2.9).
Attenuation at the bands of interest are:

$$\text{Rejection} = \begin{cases} \leq 24\,\text{dB}, & f \in [0, 2.4]\,\text{GHz}, \\ \leq 15\,\text{dB}, & f \in [0, 5.9]\,\text{GHz}, \\ 17.3\,\text{dB}, & f = 5.8\,\text{GHz} \end{cases} \tag{2.16}$$

The 2.4 GHz-band, and the upper frequency of the 5 GHz is sufficiently attenuated. However, between the 2.4 GHz- and 5 GHz-band is lower than the specifications. If we compare the results with the ones from the PDPD filter (see Eq. (2.9)), we see that an additional notch provides the required attenuation at frequencies below the 5 GHz-band.
The maximum group delay (GD) of the filter is in the lower frequency of the passband, and is $GD_{max} = 115.06\,\text{ps}$.
From Table 2.11, we see that the SEDE implementation the design specifications.

2.7 Conclusion

In this chapter we've gone over the fundamentals of filters, set design specifications, realized two different elliptical passive LC filters.

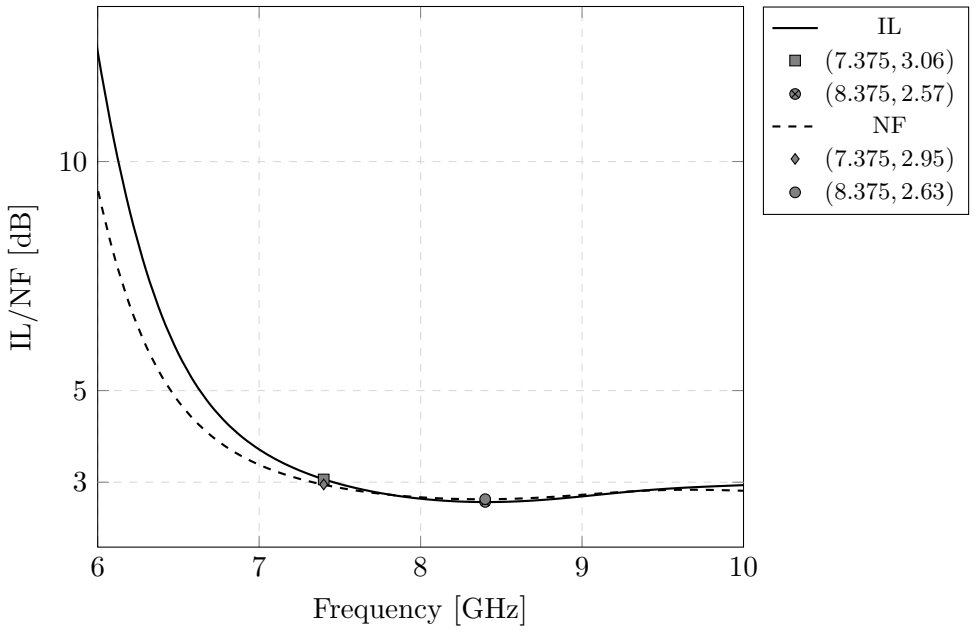

Figure 2.21: Insertion loss & NF from the SEDE elliptical filter.

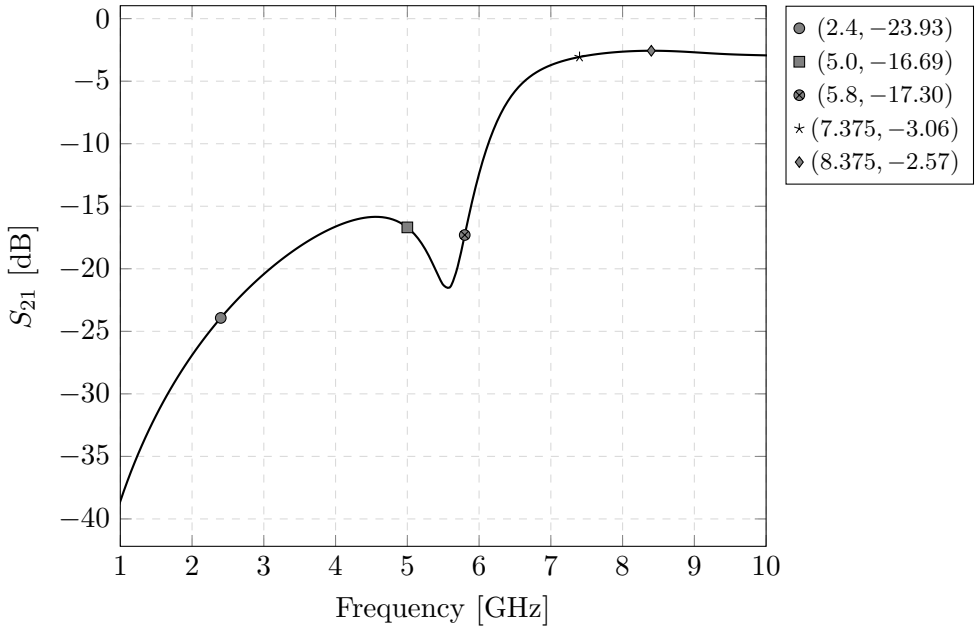

Figure 2.22: Transfer function of the SEDE elliptical filter.

The two filters match the design specification, and hence can be used in a receiver RF front-end. The pseudo-differential to pseudo-differential filter elliptical filter is used in a pseudo simultaneous transmit and receive RF receive, while the single-ended to differential elliptical filter is used in a single-antenna, single-ended to differential area optimized RF receiver

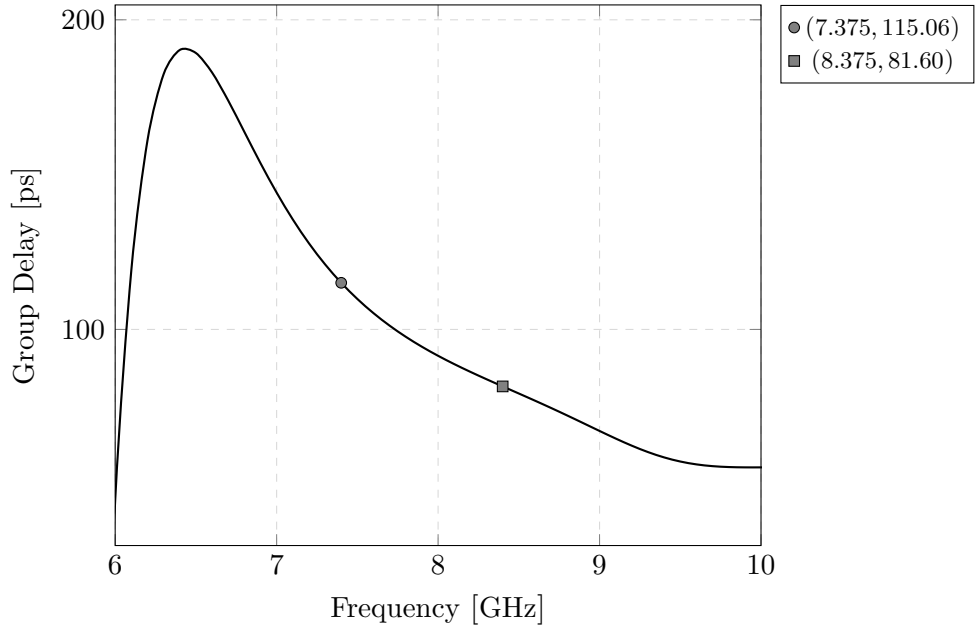

Figure 2.23: Group delay of the SEDE elliptical filter

Table 2.11: Summary for the SEDE elliptical filter

Parameter	Implementation	Specification
IL	$\leq 3.06\,\text{dB}$	$\leq 4\,\text{dB}$
NF	$\leq 2.95\,\text{dB}$	$\leq 4\,\text{dB}$
S_{11}:		
Minimum*	6.4-12 GHz	7.375-8.375 GHz
Recommended†	6.9-8.3 GHz	7.375-8.375 GHz
S_{22}		
Minimum‡	7-10.8 GHz	7.375-8.375 GHz
Recommended§	8-9 GHz	7.375-8.375 GHz
Rejection:		
@ 2.4 GHz	23.93 dB	$\geq$15 dB
@ 5.0 GHz	16.69 dB	$\geq$15 dB
@ 5.8 GHz	17.30 dB	$\geq$15 dB
GD	$\leq 115.06\,\text{ps}$	N/A

* $S_{11} \leq -10\,\text{dB}$
† $S_{11} \leq -20\,\text{dB}$
‡ $S_{22} \leq -10\,\text{dB}$
§ $S_{22} \leq -20\,\text{dB}$

front-end.

Table 2.12: Summary of the filter implementations. For filter specifications, see Tables 2.6 and 2.11.

Parameter	PDPD	SEDE
IL	$\leq$ 2.51 dB	$\leq$ 3.06 dB
NF	$\leq$ 2.36 dB	$\leq$ 2.95 dB
S_{11}:		
Minimum*	6.1-9.3 GHz	6-9.2 GHz
Recommended†	6.5-7.7 GHz	6.9-8.3 GHz
S_{22}:		
Minimum‡	6.4-8.5 GHz	6.3-8.6 GHz
Recommended§	N/A	8-9 GHz
Rejection:		
@ 2.4 GHz	14.59 dB	23.93 dB
@ 5.0 GHz	21.4 dB	16.69 dB
@ 5.8 GHz	17.32 dB	17.30 dB
GD	$\leq$ 101.2 ps	$\leq$ 115.1 ps

* $S_{11} \leq -10$ dB
† $S_{11} \leq -20$ dB
‡ $S_{22} \leq -10$ dB
§ $S_{22} \leq -20$ dB

Chapter 3

Low-Noise Amplifier Design

3.1 Introduction

The low-noise amplifier (LNA) is a crucial block in the receiver chain. Its primary goal is to amplify the received (or preferably the wanted) signal to an adequate level without significantly elevating the noise floor. Its secondary purpose is to suppress 'noise sources' from all succeeding blocks along the receiver chain, such as mixers found in homo- or heterodyne architectures. So, higher the gain of the LNA, the lower the noise contributions of subsequent circuits.
If the LNA is the first block of the receiver chain, its input impedance must be matched to that of the antenna for maximum power transfer. As we have seen in Chapter 2, the HPF is the first block in our receiver to suppress interferers from the 5 GHz band which will most likely saturate the LNA. Thus, the input impedance of the LNA is transformed via the HPF. This allows the designer a greater degree of flexibility in choosing the input impedance of the LNA. In our case, the HPF components are scaled for impedances of 100 Ohms, which is also the differential impedance of the antenna.
In this chapter, we will start by going over the basics of LNA design, briefly look at classical topologies, and then provide circuit specifications for our design.

3.2 Circuit design

The LNA circuit is based on Novelda's UWB Radar SoC's LNA [5].
The two LNAs comprise cascode (common source plus common gate stage) input stages. This current reuse LNA adds an extra CG-stage 'on top' for improved reverse isolation. This, however, requires a power supply $> 1\,\mathrm{V}$. The feedforward and feedback reactive loops via on-chip symmetrical center-tapped transformers provide passive voltage boosting and impedance matching, respectively.
Table 3.1 compares the LNA in [5] and this work. For higher voltage headroom, we scrap the current source. For better common-mode rejection, we replace the single-ended spiral inductors in [5] with a single

differential center-tapped inductor.

Table 3.1: Comparison between the two LNAs

	Novelda [5]	Implementation
Input stage	CS-stage with passive voltage boosting	CS-stage with passive voltage boosting
Active stages	CS+CG	CS+CG+CG
Input/output	Differential to pseudo-differential	Pseudo-differential to differential
Signal-conditioning	In-band peaking with bridged T-coil	In-band peaking with center-tapped LC-tank

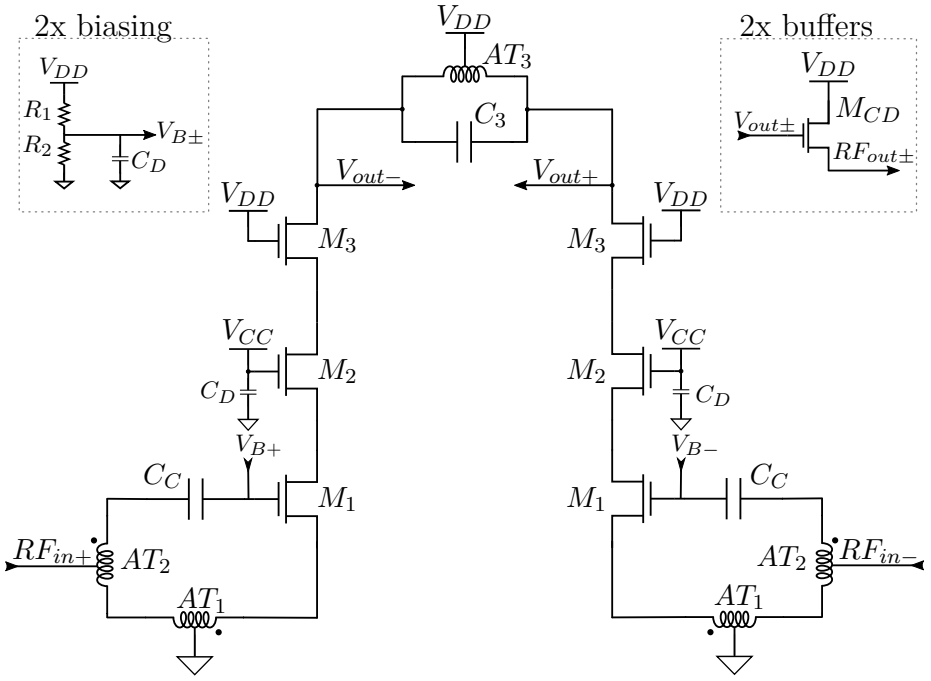

Figure 3.1: The LNA, including biasing for the input stage, and output buffers.

Table 3.2: Passive component parameters of the LNA.

Name	Value	Q-value*	SRF [GHz]
AT_1†	1.05 nH	9.8	>20
AT_2†	2.1 nH	9.2	18.3
AT_3†	1.7 nH	13.6	>20
C_C	510 fF	46.2	>20
C_D‡	6.8 pF	N/A	N/A
C_3	165 fF	126	>20
R_1	5.1 kΩ	N/A	N/A
R_2	2.2 kΩ	N/A	N/A

* @ $f_c = 7.875$ GHz
† Measured while being differentially driven.
‡ Implemented through the usage of an inverter.

Table 3.3: Active component dimensions of the LNA

Name	Ratio [µm/nm]
M_1	110/80
M_2	110/70
M_3	110/70
M_{CD}	40/60

Typical design specifications we use for designing LNAs:

Parameter	Unit
Gain	dB
Bandwidth	GHz
Noise Figure	dB
Reverse Isolation	dB
1-dB compression point	dBm
Impedance matching	dB
Power consumption	mW

In terms of gain of the active stage, there's no difference between whether

going for a CS-stage or a CG-stage[1]. We know that the gain of a single stage amplifier can be written as:

$$A_V = \frac{v_{out}}{v_{in}} = |g_m r_o|, \tag{3.1}$$

where the g_m is the transconductance of the MOSFET, and r_o is the drain-source resistance due to the channel length modulation. The resistance can be approximated to [12]:

$$r_o \approx \frac{1}{\lambda I_D}, \tag{3.2}$$

where λ is the 'channel-length modulation coefficient', which scales with $\lambda \propto \frac{1}{L}$. While one can scale the intrinsic gain up by maximizing the current (increasing g_m) and make the device longer (increasing r_o), there is an upper limit for intrinsic gain. For a 65 nm process this is approximately 10. To increase the gain, one typically loads the active device with an additional resistive load, however due to the system requirement of having signal conditioning, a resistive load is not viable. To achieve a higher gain, without having to be dependent on the physical length of the device itself, we use a tuned load (LC-tank). The gain of an LC-tank can be approximated to [13]:

$$A_V = g_m \cdot (R_P || r_o) \approx g_m \cdot \omega L Q = g_m Q^2 r_s, R_P \gg r_o, \tag{3.3}$$

at the resonance frequency. The benefits of using a tuned amplifier are:

- Voltage drop: Ideally the voltage drop across the LC tank is 0, however due to the metals itself in the inductor, there will always be some resistance (r_s). This resistance is small when compared the resistive load, hence the voltage drop is significantly less.
- Voltage swing: it's possible to achieve an AC voltage swing across the LC tank higher than the DC-voltage [13].
- Bandwidth selectivity: If the tank is tuned correctly we will achieve a bandpass response. This provides additional filtering with regards to out-of-band blockers.

On the other hand, on-chip inductors are bulky (in terms of area), and lossy. One expect a maximum $Q \approx 20$.

[1]The CS-stage has a phase shift of 180° compared to the CG-stage.

Table 3.4: Trade-offs in terms of gain for the three common output stages.

Parameter	Unloaded	Resistive	Tuned
Gain	Low	High	Q-dependent
Voltage drop	None	High	Low
Peak voltage	V_{DD}	V_{DD}	$> V_{DD}$ *
Area	Very low	Low	High

* Swings around the DC-level.

For $A_V \geq 30\,\text{dB}$ and frequency selectivity, we will use an LC-tank as the LNA load.

Table 3.5: Summary of gain contributions in an LNA

Component	Gain	Limitation
Unloaded	$g_m r_o$	W/L & process dependent.
Resistive load	$g_m R_L$	Noise, DC voltage drop.
Tuned load	$g_m \omega L Q$	Area & Q_f †

† Dependent on the available material of the process.

The center frequency for the LNA is given by the resonant frequency of the LC-tank as:

$$f_c = \frac{1}{2\pi \cdot \sqrt{LC}}, \tag{3.4}$$

where L is the self-inductance of the inductor, and C is the capacitance (including parasitic capacitance). To maximize gain, we will find the value of L with the highest value of Q. Thus, $L_{AT_3} = 1.7\,\text{nH}$ and $C_3 = 165\,\text{fF}$, and the resonant frequency is:

$$f_c = \frac{1}{2\pi\sqrt{1.7\,\text{nH} \cdot 165\,\text{fF}}} \approx 9.5\,\text{GHz} \tag{3.5}$$

If we wanted to match the system center frequency, $f_c = 7.875\,\text{GHz}$, we have to see a parasitic capacitance value of $C_{par} \approx 75\,\text{fF}$. This parasitic capacitance is mostly dependent on the layout itself, and especially the width and length of the signal-wire itself. Moving onward, we assume that the resonant frequency is at the center frequency of the system, $f_c = 7.875\,\text{GHz}$.
In terms of bandwidth, we have that the device bandwidth, i.e. the maximum frequency of operation on the device level itself to be:

$$BW = f_T \approx \frac{g_m}{2\pi C_{gg}}, \tag{3.6}$$

where f_T is the transit frequency of the device, C_{gg} is the total capacitance looking into the gate , and g_m is the transconductance. While

the transit frequency doesn't show exactly the 'practical' bandwidth, it gives us the upper frequency of operation. For the 65 nm we know the transit frequency to be much larger than the frequency of interest.
The effective bandwidth is limited to the output stage. In the case of using a tuned load, we know that the fractional $-3\,\mathrm{dB}$ bandwidth can be written as [13]:

$$BW = f_r = \frac{f_c}{Q}, \tag{3.7}$$

where f_r is the fractional bandwidth, f_c is the center frequency, and Q is the quality factor of the tank.
For the bandwidth specification, we have the system level requirement of:

$$BW_{-10\,\mathrm{dB}} = 1\,\mathrm{GHz},\ f_c \pm 500\,\mathrm{MHz} \tag{3.8}$$

To find the Q, we use the $-3\,\mathrm{dB}$-bandwidth, and find that to be:

$$Q_f = \frac{f_c}{BW_{-3\,\mathrm{dB}}} = \frac{7.875\,\mathrm{GHz}}{400\,\mathrm{MHz}} \approx 19.7 \tag{3.9}$$

This gives us a Q of 19.7, which in turn gives us a $-10\,\mathrm{dB}$ BW of 1 GHz. If required, one could extend the effective bandwidth implementing *T-coil bandwidth enhancement*[13, 14].

Table 3.6: Summary of BW limitations in an LNA

Component	BW	Limitation
No ext. load	$\frac{g_m}{2\pi C_{gg}}$	WL & process dependent.
Resistive load	$\frac{g_m}{2\pi RC_{gg}}$	R & f_t.*
Tuned load	$\frac{f_c}{Q_f}$	f_c & Q_f†

* Dependent on the input stage.
† Dependent on the available material of the process.

To ensure that the characteristics of the LC-tank doesn't change, we need to ensure that the load of the tank is constant. This can be achieved through the usage of common-drain (CD) stages, where we do the voltage buffering between the LC-tank and the 'outside world'. The implementation of the CD-stages is shown in Fig. 3.1, where they are dimensioned to achieve an output impedance of:

$$Z_{out} = \frac{1}{g_m} = 50\,\Omega, \tag{3.10}$$

where we assumed that the output load is $Z_{out} = 50\,\Omega$. For the output matching, it's the same as with the CG-stage, the g_m is set to be the reciprocal of the load, i.e. $g_m = 50\,\Omega^{-1} = 25\,\mathrm{mS}$.
For the CD-stage we trade-off impedance isolation for power & gain.

For the input impedance matching, we're dependent on the realized input stage, as well as the input matching network. A CG-stage has an input impedance of [15]:

$$R_{in} \approx \frac{1}{g_m} \tag{3.11}$$

For an inductively loaded CS-stage, we have the input impedance as [15]:

$$Z_{in}(s) = \frac{L_1 (C_1 + C_f) s^2 + R_s (C_1 + C_f) s + 1}{[L_1 C_1 s^2 + (R_s C_1 + g_m L_1) s + 1 + g_m R_s] C_f s}, \tag{3.12}$$

where we have the output inductor, L_1, the output capacitance, C_1, the feedback capacitance between the gate and the drain of the CS-stage, C_F, the parasitic series resistance in the output inductor, R_S, and g_m is the transconductance of the CS-stage. One of the issues with a single CS-stage is that the feedback capacitor, C_f creates a negative resistance at a certain frequency.

While CG-stage is easily matched when compared to the CS-stage, we want to be able to increase the g_m of the device (to increase gain) without sacrificing input impedance matching. Moving forward, a CS-stage is the chosen topology for the input stage.

To do impedance matching on the CS-stage, we want to resonate out both the capacitance seen between gate-drain, as well as gate-source. Using inductive degeneration, we manage to resonate the gate-source capacitance out. The inductive degeneration is implemented through the auto-transformer, AT_1 (Fig. 3.1). To resonate out the gate-drain capacitance, we will be using a series inductance, AT_2 (Fig. 3.1). If we couple these two auto-transformers, there are several benefits:

the input impedance matching, is the impedance transformed by the coupling of the two windings, created by AT_1 & AT_2. For transfomers, we have the general impedance tranformation:

$$Z_p = \frac{Z_s}{N^2}, \tag{3.13}$$

where, Z_p is the impedance looking into the first winding, and Z_s is the impedance looking into the secondary winding, while N is the turn ratio between secondary and primary turn ratio. In the case of looking into the source-side of a MOSFET we have the relation:

$$Z_{in} = Z_p = \frac{\frac{1}{g_m}}{N^2} \tag{3.14}$$

By coupling the current back into the gate in the positive feedback loop, we achieve passive g_m-boosting [16]. The effective g_m-boosted transconductance, G_m can be written as:

$$G_m = k \cdot \frac{N_S}{N_P} \cdot g_m \tag{3.15}$$

Thus, the input impedance looking into the g_m-boosted CS-stage, assuming we're at resonating out all the capacitance:

$$Z_{in} = \frac{\frac{1}{G_m}}{N_{P,S}^2} = \frac{\frac{1}{\frac{N_S}{N_P} \cdot g_m}}{\left(\frac{N_P}{N_S}\right)^2} = \frac{N_S}{N_P} \cdot \frac{1}{g_m}, \tag{3.16}$$

which in terms of self-inductance can be written as [11]:

$$Z_{in} = \frac{N_S}{N_P} \cdot \frac{1}{g_m} = \frac{\sqrt{L_2 L_1}}{g_m} \tag{3.17}$$

From a matching perspective we're now contrained by the transconductance of the device, as well as the turn ratio between the auto-transformers, acting as the primary and secondary windings.
While the turn ratio between the two windings provides a higher effective transconductance we're somewhat limited by the size of the device. We will use a 2:1 self-inductance ratio between the secondary and the primary winding. To find the required g_m of the input stage, we need to solve Eq. (3.17) for g_m. For $Z_{in} = 50\,\Omega$, and a self-inductance ratio of 2:1, we get:

$$g_m = \frac{\sqrt{L_2 L_1}}{Z_{in}} = \frac{\sqrt{2}}{50\,\Omega} \approx 28.28\,\text{mS} \tag{3.18}$$

Table 3.7: Summary of input impedance & limitations

Component	Z_{in}	Limitation
CG-stage	$\frac{1}{g_m}$	N/A
CS-stage	See Eq. (3.12)	Load, C_F & g_m
CS-stage*	$\frac{\sqrt{L_2 L_1}}{g_m}$	$N_{S,P}$†

* With passive voltage boosting
† Turn ratio between secondary- and primary winding.

To maximimize the SNR of the system, we need the LNA to contribute as much gain as possible, while adding the least amount of possible noise to the system. With regards to noise figure (NF), we care about the added noise from the input stage CS-/CG- as well as from the output stage.
For an input impedance matched CG-input stage, i.e. $g_m = \frac{1}{R_S}$, we can estimate the NF to be [15]:

$$\begin{aligned} NF &= 1 + \frac{\gamma}{g_m R_S} + \frac{R_S}{R_1}\left(1 + \frac{1}{g_m R_S}\right)^2 \\ &= 1 + \gamma + 4\frac{R_S}{R_1}, \end{aligned} \tag{3.19}$$

where γ is the process dependent constant, $R_S = 50\,\Omega$ is the source resistance and R_1 is the load resistance.
Assuming that $\gamma = 1$, and that $4\frac{R_S}{R_1} \ll 1 + \gamma$, we get an NF of 3 dB. A lower NF is achievable at the cost of impedance matching.
For a CS-stage, we can estimate the NF to be [15]:

$$\begin{aligned} NF &= \frac{4kT\gamma g_m r_o^2 + 4KTR_S\left(g_m R_o\right)^2}{\left(g_m R_o\right)^2} \cdot \frac{1}{4kTR_S} \\ &= \frac{\gamma}{g_m R_S} + 1, \end{aligned} \tag{3.20}$$

where γ is a process dependent constant, g_m is the transconductance of the CS-stage, and R_S is the source resistance.
For a CS-stage we can achieve a better noise performance by increasing the transconductance of the device, at the cost of increased power consumption.
In addition to the active input stage, the output stage also contributes additional noise. For an LC-tank, the parastic series resistance in the tank adds thermal noise to the total noise power. We can define the added noise from an LC-tank as:

$$\overline{V_n^2} = 4kTR_S = 4kT\frac{\omega L}{Q} \tag{3.21}$$

Due to the small series resistance in the LC-tank, we assume that the input stage itself is the dominant noise contributor. In terms of specifications we want a total NF ≤ 3 dB.
Solving Eq. (3.20) for g_m, the required transconductance of the CS-stage required to achieve the specification is:

$$g_m = \frac{\gamma}{2R_S} = \frac{1}{2 \cdot 50\,\Omega} = 25\,\text{mS}, \tag{3.22}$$

where $\gamma = 1$, and $R_S = 50\,\Omega$. In terms of g_m, one can trade-off noise & gain for area and/or power consumption.
Reverse isolation is the 'reverse gain' of the device. For zero-/low-IF receivers, a high reverse isolation of the LNA is required to minimize LO-leakage to the antenna. An amplifier with low reverse isolation is prone to instability because of the positive feedback through parasitic paths from the output to the input. For high reverse isolation, one employs cascoding. The reverse gain for a cascode is [15]:

$$\frac{V_{ant}}{V_x} \approx \frac{sR_{ant}C_{gd}}{g_{m2}r_{o2}} \tag{3.23}$$

From Eq. (3.23), we see that the reverse isolation increase by a factor $g_m r_o$. We trade off added reverse isolation for voltage headroom. The CG-stage reduce the Miller capacitance.

Table 3.8: Summary of noise contributions in the LNA.

Component	Type of noise	Limitation
MOSFETs	Thermal	γ, process dependent g_{d0}, size dependent
	Flicker	f
	Thermal, gate resistance	$\frac{W}{L}$, N-fingers
CS-stage	Thermal+flicker	$\frac{\gamma}{g_m R_s} + 1$
CG-stage	Thermal+flicker	$1 + \gamma + 4\frac{R_S}{R_L}$
Resistive load	Thermal	R
Tuned load	Thermal	R_S *

* Parasitic series resistance in the LC-tank, layout dependent.

The specification for reverse isolation is, $S_{12} \geq 60\,\text{dB}$, and thus we employ 2×CG-stages. The additional CG-stage it's also beneficial in other ways:

+ Increase in output impedance.

+ Turn off the LNA half-circuit, by turning off the 1st CG-stage.

+ Use of higher supply voltage without having to worry about reliability. In addition, it increases the effectivness of the LDO, due to reduced dropout voltage, going from 1.8-1.5 V as opposed to, 1.8-1.2 V using the nominal voltage supply.

− One of the major costs of cascoding is the reduced voltage headroom, so for two additional CG stages the voltage headroom (relative to the input stage) is reduced by $\approx 2 \cdot V_{th}$, which might cause issue with regards to linearity and/or compression.

The extra CG-stages has similar dimensions as the input stage, albeit an increase in length to increase the gain.
In terms of biasing, we bias the 1st CG-stage to the nominal supply of 1.2 V, and the 2nd CG-stage is over-volted to the system supply voltage, 1.5 V. The 2nd CG-stage is biased to the nominal supply to ensure that the V_{GS} of the device does not surpass the nominal supply. This is done with regards to reliability.
One parameter that is closely related to reverse isolation is the stability of the LNA. We ensure that the amplifier is *inherently stable* regardless of the input/output impedances.
In terms of stability of a two-port network, it's common to use either the:

1. K-Δ stability test

2. μ-stability test,

where:

$$\begin{array}{c}\text{K-}\Delta \text{ stability test: } K > 1 \;\&\; |\Delta| < 1 \\ \mu\text{-stability test: } \mu > 1\end{array}, \tag{3.24}$$

with

$$\Delta = S_{11}S_{22} - S_{12}S_{21} \tag{3.25}$$

$$K = \frac{1 - |S_{11}|^2 - |S_{22}|^2 + |\Delta|^2}{2|S_{12}||S_{21}|}, \tag{3.26}$$

$$\mu = \frac{1 - |S_{11}|^2}{|S_{11}^*\Delta - S_{22}| + |S_{12}S_{21}|}, \tag{3.27}$$

From Eqs. (3.26) and (3.27), we see that reverse isolation, $|S_{12}|$ impacts the stability of the amplifier, so we maximize the reverse isolation.
We want an unconditionally stable LNA, thus, $\mu \geq 1$.
A figure of merit in terms of linearity is the $-1\,\text{dB}$ compression point (P1dB), which tells the input power at which the gain (A_V) compresses by 1 dB. The P1dB can be expressed as [15]:

$$P_{in,-1\,\text{dB}} = \sqrt{0.145|\frac{\alpha_1}{\alpha_3}|}, \tag{3.28}$$

where α_1 is the DC quantity arising from second-order nonlinearity, and α_2 is the fundamental harmonic.
We want to have a P1dB specification of $> -30\,\text{dBm}$
The biasing for the input stage (M_1) is designed around the 'g_m/I_d design methodology' [17].
From specifications, we have a fixed current of 2.5 mA per half-circuit, and g_m & V_{OV} can then be derived. We know that the g_m of the device affects the gain, noise figure and the input impedance. Maximizing g_m is done through maximizing the efficiency, g_m/I_d, which in turn reduces V_{OV}. By reducing V_{OV}, one increases the dimension of the active devices, for a fixed current. For a fixed amount of current, we have the following trades-offs:

- Low Vov (weak inversion):
  - \+ High efficiency, g_m/I_d
  - \- Low current density, $I_d/W \rightarrow$ larger devices
  - \- Biased at the edge of saturation region $\rightarrow$ lower linearity
- High Vov (strong inversion):
  - \+ Higher current density, $Id/W \rightarrow$ smaller devices
  - \+ Deeply biased in saturation region $\rightarrow$ higher linearity
  - \- Lower efficiency, g_m/I_d

One biases between two extremes, i.e. at *medium inversion*. This gives us a compromise between efficiency, gain and active area. Choosing an efficiency of $g_m/I_d = 10\,\mathrm{V}^{-1}$, V_{OV} is [17].

$$V_{OV} = \frac{2I_d}{g_m} = \frac{2}{g_m/I_d} = \frac{2}{10\,\mathrm{V}^{-1}} = 200\,\mathrm{mV} \tag{3.29}$$

From g_m and I_d, we have

$$V_{OV} = \frac{2I_d}{g_m} = \frac{2 \cdot 2.5\,\mathrm{mA}}{30\,\mathrm{mS}} \approx 167\,\mathrm{mV} \tag{3.30}$$

As a rule of thumb, $V_{OV} = 0.1 \cdot V_{DD} = 150\,\mathrm{mV}$.
Moving forward, the overdrive voltge is set to $V_{OV} = 170\,\mathrm{mV}$. The input stage is implemented using low-voltage threshold (LVT) devices from TSMC, the gate-source voltage, V_{GS} is:

$$V_{GS} = V_{OV} + V_{th} = 170\,\mathrm{mV} + 380\,\mathrm{mV} = 550\,\mathrm{mV} \tag{3.31}$$

A resistive divider (see Fig. 3.1) is used for biasing the input stage.

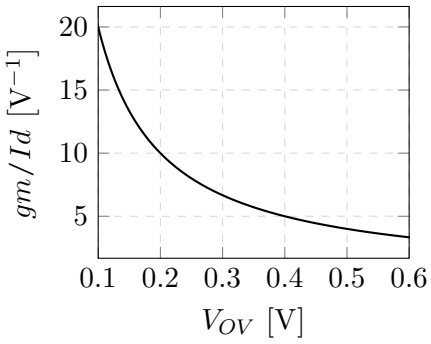

(a) Efficiency g_m/I_d vs V_{OV}

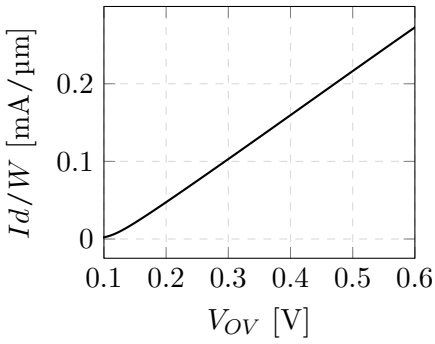

(b) Current density, I_d/W vs efficiency, g_m/I_d

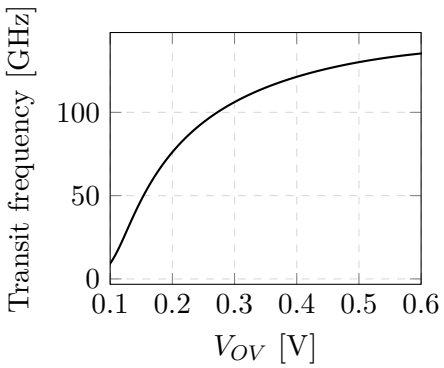

(c) Transit frequency, F_t vs efficiency, gm/I_d

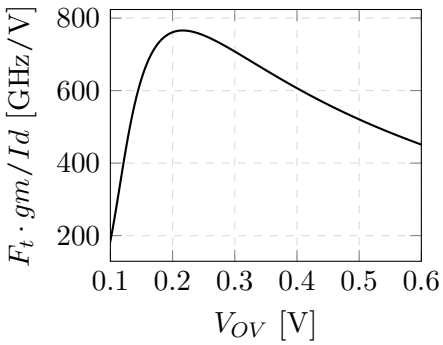

(d) FOM for a single device, Speed-product, $F_t \cdot g_m/I_d$ vs V_{OV}

Figure 3.2: Biasing parameters used for the 'g_m/I_d design methodology'. Simulated on an nMOS device with $W/L = 1\,\mu\mathrm{m}/60\,\mathrm{nm}$.

Table 3.9: Biasing parameters derived using the gm/Id method

Parameter	Realization	Design specification
V_{gate}	447 mV	550 mV
V_{source}	8.337 mV	0 V
V_{th}	382.6 mV	380 mV
V_{OV}	54.34 mV	170 mV
g_m/I_d	12.67 V^{-1}	10 V^{-1}
g_m	36.31 mS	30 mS
I_d	2.865 mA	2.5 mA

The LNA core is build using the PCells from TSMC's 65 nm library, where deep N-well 6T or six terminal low threshold voltage RF active devices are chosen because of their well modelled parasitic capacitance and noise isolation properties.
To reduce gate resistance, we realize MOSFETs with the maximum fingers. The gate noise as a function of fingers, can be modelled as [12]:

$$\overline{V_n^2} = 4kT\frac{R_G}{3}\frac{1}{N^2}, \tag{3.32}$$

where k is the Boltzmann's constant, T is the temperature in kelvin, R_G is the gate resistance, as a function of the polysilicon sheet resistance, and N is the amount of fingers for the device. Increasing the fingers reduces the resistance at the gate, as well as at the drain of the MOSFET.
The LC-tank is realized using TSMC's scalable center-tapped inductor model (`spiral_sym_ct_std_mu_z`), and the capacitor is realized using TSMC's scalable MoM capacitors (`crtmom_rf`)
The center-tapped inductor offers common-mode rejection, higher self-inductance and higher Q when driven differentially [11].
The resistive divider is built with unit-cells, to minimize mismatch. The resistors are implemented in a 4×N manner, where the rest of the array is filled up with dummy devices. R_1 is realized using a total of 8 unit cells, where 7 of them are active, and 1 is a dummy. R_2 is realized using a total 4 units, where 3 of them are active, and 1 is a dummy. Thus, V_{GS} is:

$$V_{GS} = \frac{R_2}{R_1 + R_2}V_{DD} = \frac{3}{10}1.5\,\text{V} = 450\,\text{mV} \tag{3.33}$$

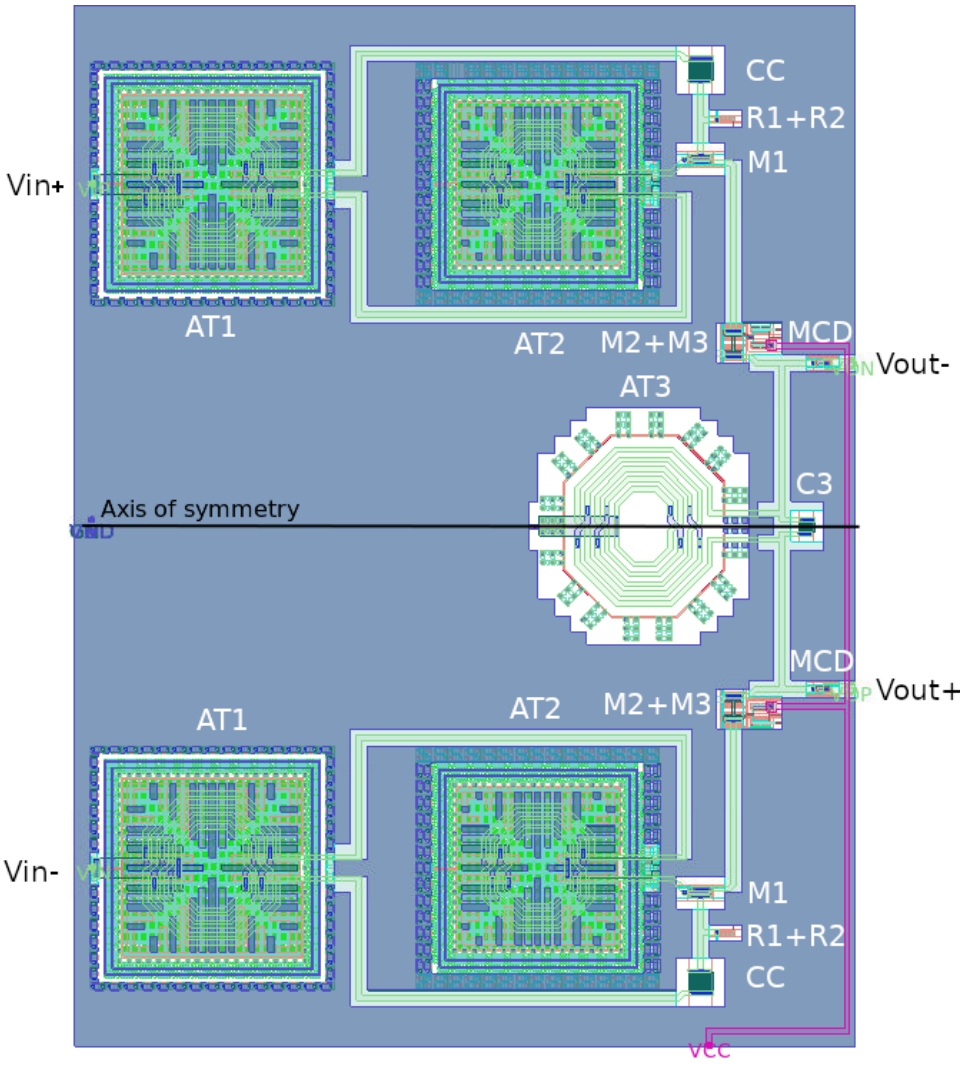

Figure 3.3: Layout of the LNA

Table 3.10: Design specifications of the LNA

Gain	$\geq 30\,\text{dB}$
Bandwidth*	$\geq 1\,\text{GHz}$
S_{11}	$\leq -10\,\text{dB}$
S_{12}	$\geq 60\,\text{dB}$
NF	$\leq 3\,\text{dB}$
P1dB	$\geq -30\,\text{dBm}$
DC current†	$\leq 2.5\,\text{mA}$
Power supply	$1.5\,\text{V}$

* Measured at $-10\,\text{dB}$ from max gain
† Measured for the half-circuit, excluding output buffers.

3.3 Simulation results

The return loss (S_{11}) of the LNA, shows how well the LNA is matched to a differential source impedance of $100\,\Omega$. The maximum return loss is at the upper frequency (8.375 GHz) of the passband, and is $S_{11|max} = -10.45\,\text{dB}$. The bandwidth for $S_{11} \leq -10\,\text{dB}$ is 5.6-8.6 GHz.
From Fig. 3.5a, the real impedance, is off by $\approx 40\,\Omega$ in the band of interest. The reason for this is the change in the biasing condition of the input stage (ground bounce)[2] this causes the V_{OV} to be lower, and g_m to be higher ($\frac{2I_d}{g_m} = V_{OV}$) for a constant current.
The output return loss (S_{22}) of the LNA, shows how well the LNA is matched to a differential $100\,\Omega$ load. The maximum return loss is at the upper frequency (8.375 GHz) of passband, and is: $S_{22|max} = -13.33\,\text{dB}$. The bandwidth for $S_{22} \leq -10\,\text{dB}$ is from 1-12 GHz. For the desired $S_{22} \leq -20\,\text{dB}$, are out of band ($< 4.6\,\text{GHz}$).
For the voltage gain & bandwidth, we look at the transfer function for the LNA. The voltage gain is reported as the maximum gain, while the bandwidth is reported as the $-10\,\text{dB}$-bandwidth.
In terms of maximum gain, we have:

$$\begin{aligned} A_{V|max} &= 20.1\,\text{dB},\ f = 8.1\,\text{GHz} \\ A_{V|no-buffer,max} &= 27.3\,\text{dB},\ f = 8.1\,\text{GHz} \end{aligned} \tag{3.34}$$

From the maximum gain, we can see that the buffers show a loss of 7.2 dB (27.3 dB - 20.1 dB). We see that the resonant frequency of the LC-tank is 8.1 GHz.

[2] Ground bounce as in the ground is not longer at a zero voltage potential,but has a certain voltage due to parasitic resistance in the power routing.

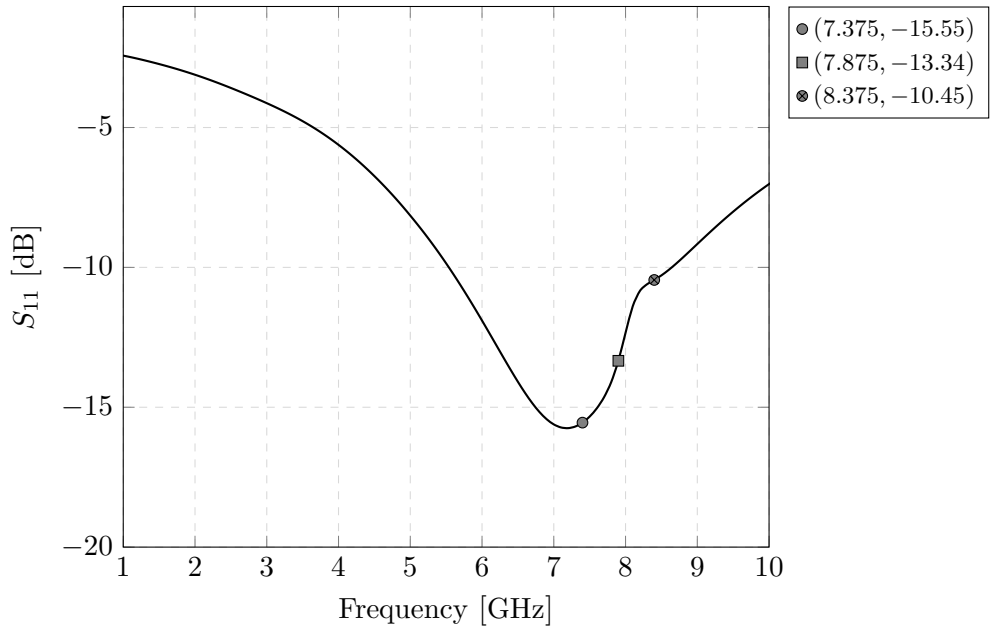

Figure 3.4: S_{11} of the LNA.

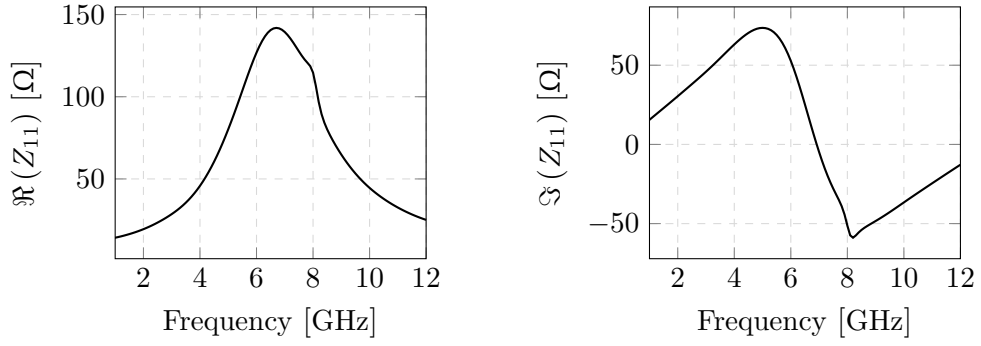

(a) $\Re(Z_{11})$ (b) $\Im(Z_{11})$

Figure 3.5: Real & imaginary input impedances of the LNA.

The $-10\,\mathrm{dB}$ BW is:

$$BW = 8.8\,\mathrm{GHz} - 7.3\,\mathrm{GHz} = 1.5\,\mathrm{GHz}, \tag{3.35}$$

relative to the center frequency, the BW is:

$$BW = f_c \pm \frac{BW}{2} \approx 8.1\,\mathrm{GHz} \pm 750\,\mathrm{MHz} \tag{3.36}$$

Compared to the specifications, we see that the gain is off by $3\,\mathrm{dB}$[3], the center frequency is off by $300\,\mathrm{MHz}$. The bandwidth meets the $1\,\mathrm{GHz}$ requirement at $-10\,\mathrm{dB}$.

[3]With the buffer deembeded

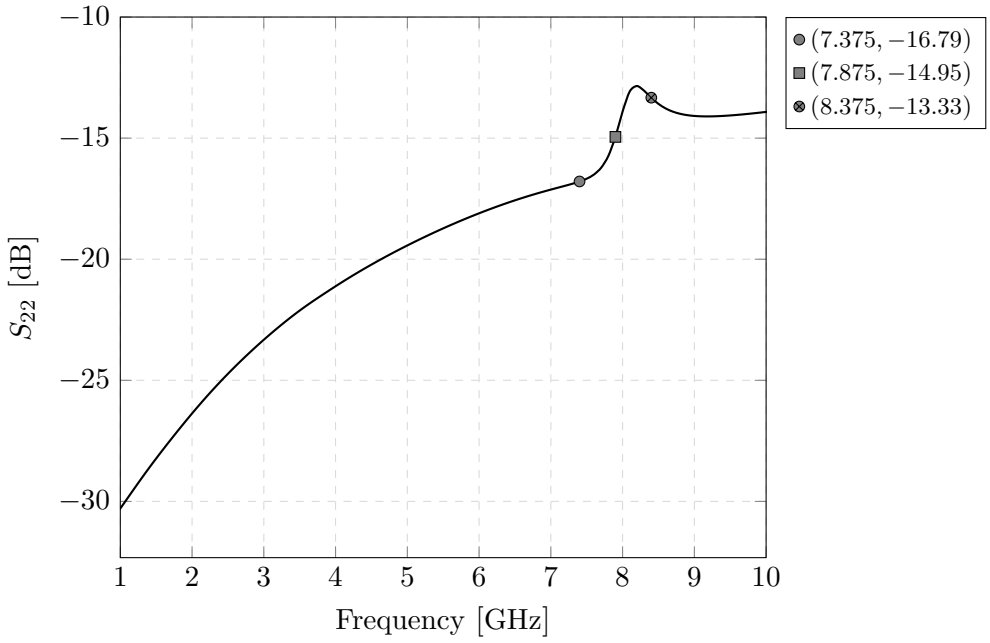

Figure 3.6: S_{22} of the LNA.

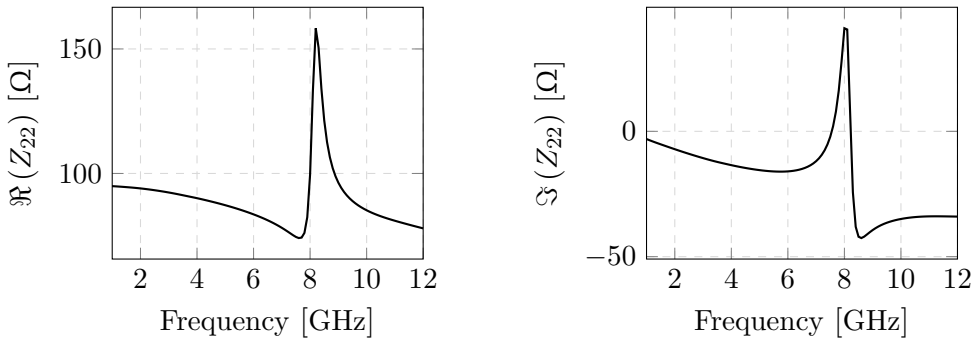

(a) $\Re(Z_{22})$ (b) $\Im(Z_{22})$

Figure 3.7: Real & imaginary output impedance of the LNA.

For the reverse isolation , we look at the transfer function from the output to the input, i.e. the reverse gain of the LNA. The minimum reverse isolation is found at the upper frequency (8.375 GHz) of the passband, and is $S_{12|min} = 43.18\,\text{dB}$
The reverse isolation is $\approx$ 17 dB worse than specified. What matters is that the LNA is unconditionally stable.
To measure stability we will use the μ-stability test, which tells us whether the LNA is unconditionally stable ($\mu \geq 1$). The minimum value of μ is found in the upper frequency (8.2 GHz) of the passband, and is $\mu_{min} = 3.66$.
As shown in Fig. 3.10, we meet the condition for unconditionally stability from 6-10 GHz.

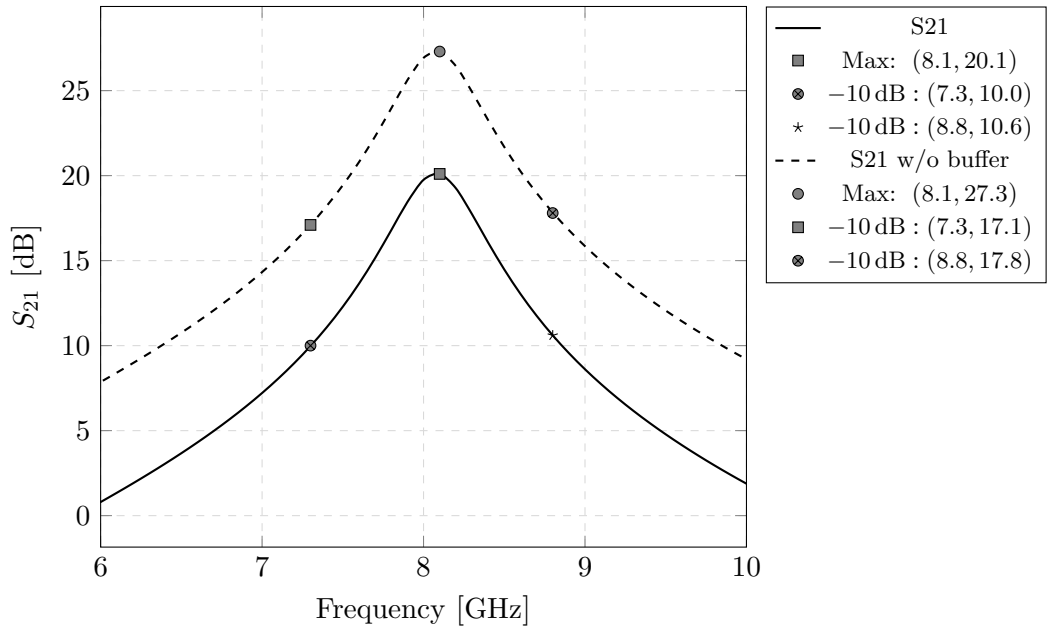

Figure 3.8: Frequency response of the LNA using S-parameter S_{21}

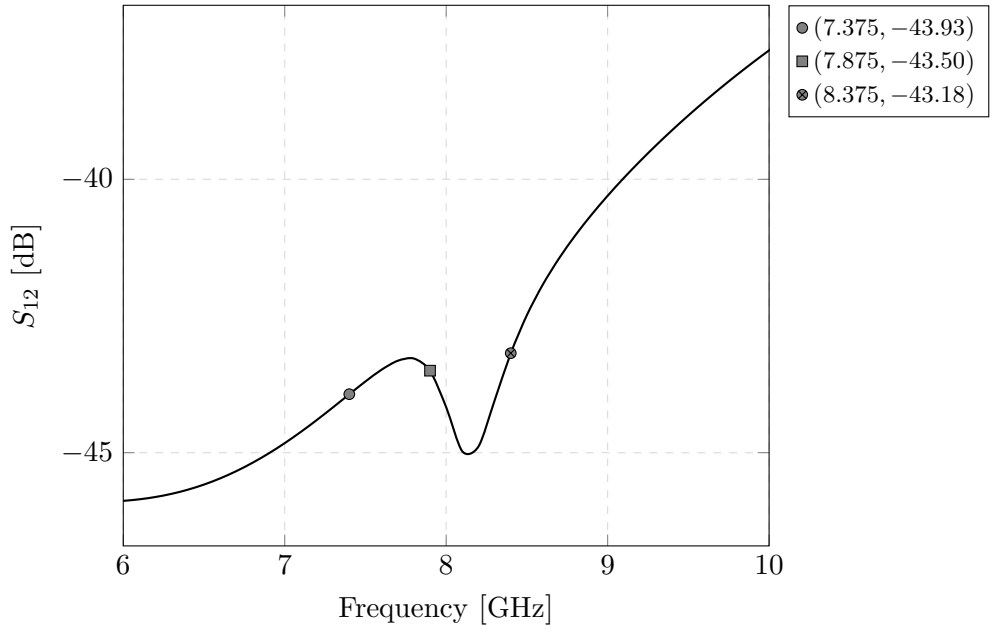

Figure 3.9: Reverse isolation of the LNA

The noise figure (NF) in the passband is

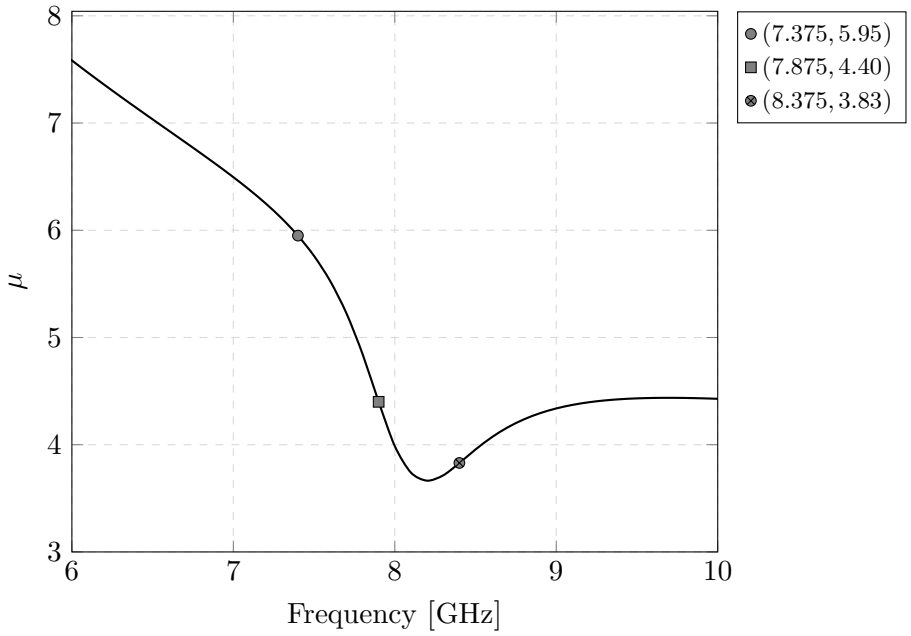

Figure 3.10: μ-factor for stability

	$f_c - 500\,\text{MHz}$	f_c	$f_c + 500\,\text{MHz}$
NF	4.28 dB	4.22 dB	4.38 dB
NF_{min}	4.27 dB	4.20 dB	4.29 dB

Compared to the specifications, we are 1 dB off. Nonetheless, we are noise matched.
For 1 dB compression point (P1dB), we use large signal S-parameters (LSSP), were we sweep the input power, P_{RF}
Input and output return loss is $\ll -10\,\text{dB}$ for $P_{RF} > 0\,\text{dBm}$ (see Figs. 3.12a and 3.12c). From Fig. 3.12b, the P1dB is $-17\,\text{dBm}$, which is 13 dBm higher than required.
The total current consumption, I_{DC}, of the LNA is 10 mA. I_{DC} is the sum of the current per branch ($2 \times 3\,\text{mA}$) and per buffer ($2 \times 2\,\text{mA}$). The total power, P_{DC}, is 15 mW from a 1.5 V supply.

3.4 Conclusion

In this chapter we've looked at the background theory, the specifications required, as well as realized an LNA for the UWB frequency spectrum. This realization will be used as a baseline for the implementation of a RF-receiver front-end moving onward.

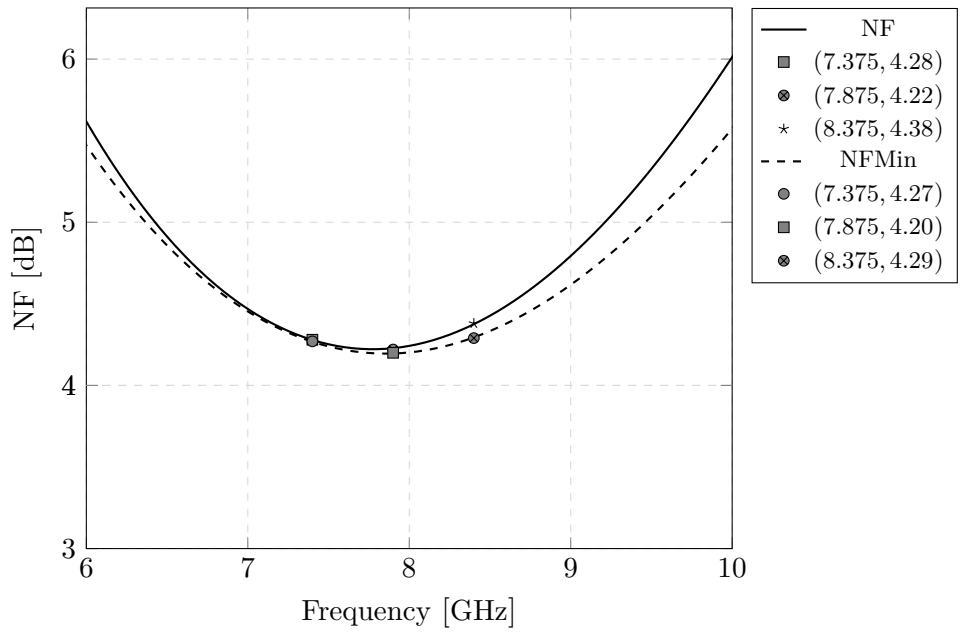

Figure 3.11: Noise figure for the LNA

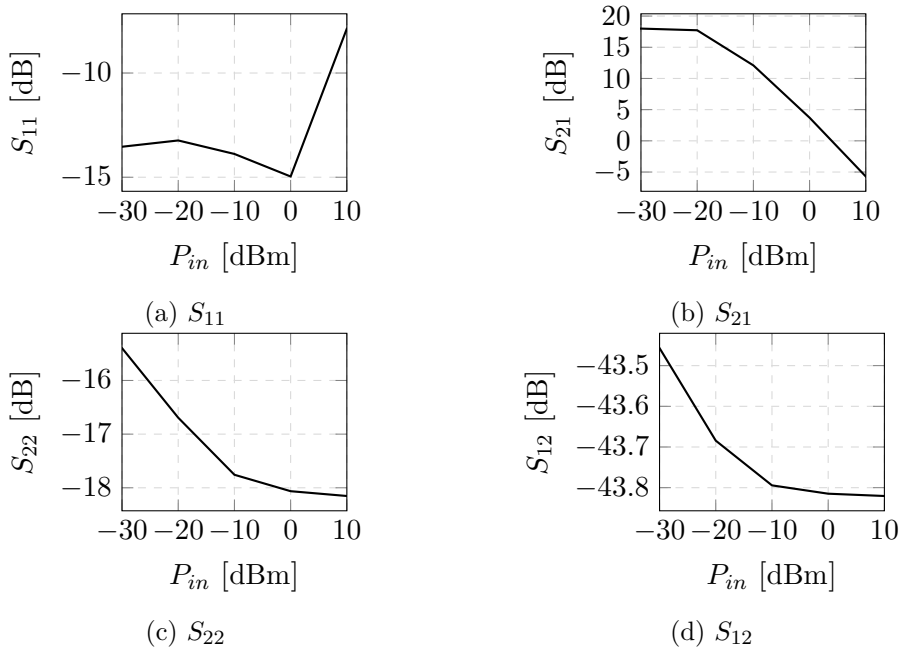

(a) S_{11} (b) S_{21}

(c) S_{22} (d) S_{12}

Figure 3.12: LSSP at $f_c = 7.875\,\text{GHz}$ with P_{RF} from $-30\,\text{dBm}$ to $10\,\text{dBm}$

.

Table 3.11: Summary of simulation results.

Gain	27.3 dB*
Bandwidth†	1.5 GHz
S_{11}	
Minimum‡	5.6-8.6 GHz
Desired§	N/A
S_{22}	
Minimum‖	1-12 GHz
Desired¶	N/A
RI	$\geq$ 43.18 dB
Stability, μ-factor	$>$ 3.83
NF	$\leq$ 4.38 dB
P1dB	-17 dBm
DC current	6 mA*

* Buffer deembedded
† -10 dB
‡ $S_{11} \leq -10$ dB
§ $S_{11} \leq -20$ dB
‖ $S_{22} \leq -10$ dB
¶ $S_{22} \leq -20$ dB

Chapter 4

Area Optimized and Passively Reconfigurable RF Front-Ends

RF receivers have to condition and amplify the received signal to a sufficient level. This can happen in multiple stages. The receiver chain core comprises filter (for signal conditioning), low-noise-amplifier (for frequency selectivity and amplification) and ADC (digitisation). Unlike direct-RF, low-/zero-IF architectures require additional mixing and filtering stages.

Thus, direct-RF has benefits, such as relaxed filtering, no LO-leakage, no quadrature LO, and in general a simpler receiver chain [18]. However, the ADC noise contribution is higher, due to lack of additional gain from the mixing and baseband stage(s) [19].

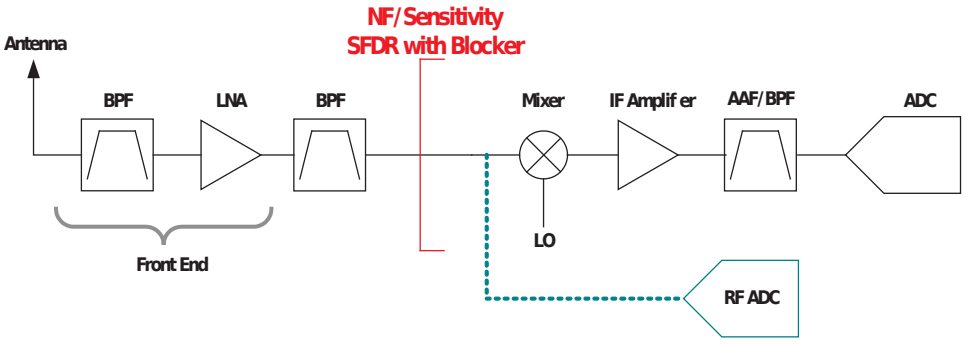

Figure 4.1: Comparison between heterodyne and direct RF-sampling receivers [19]

We will build a front-end, which consists of the HPF is Chapter 2 and an LNA in Chapter 3.

In this chapter, we propose two different RFFEs. The first one being an area optimized RFFE for single-antenna use. The second a passively reconfigurable RFFE.

4.1 Area-optimized RFFE

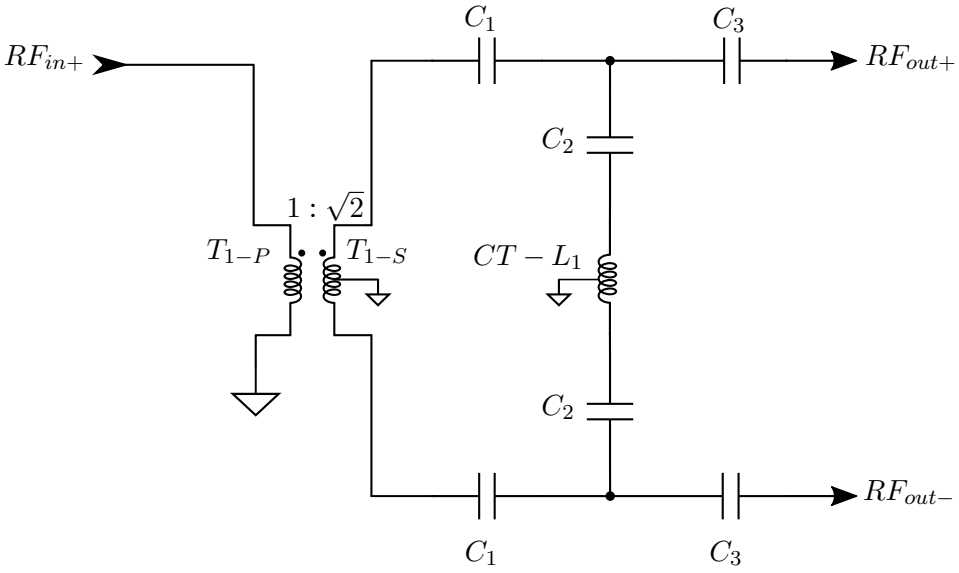

Figure 4.2: SEDE-HPF

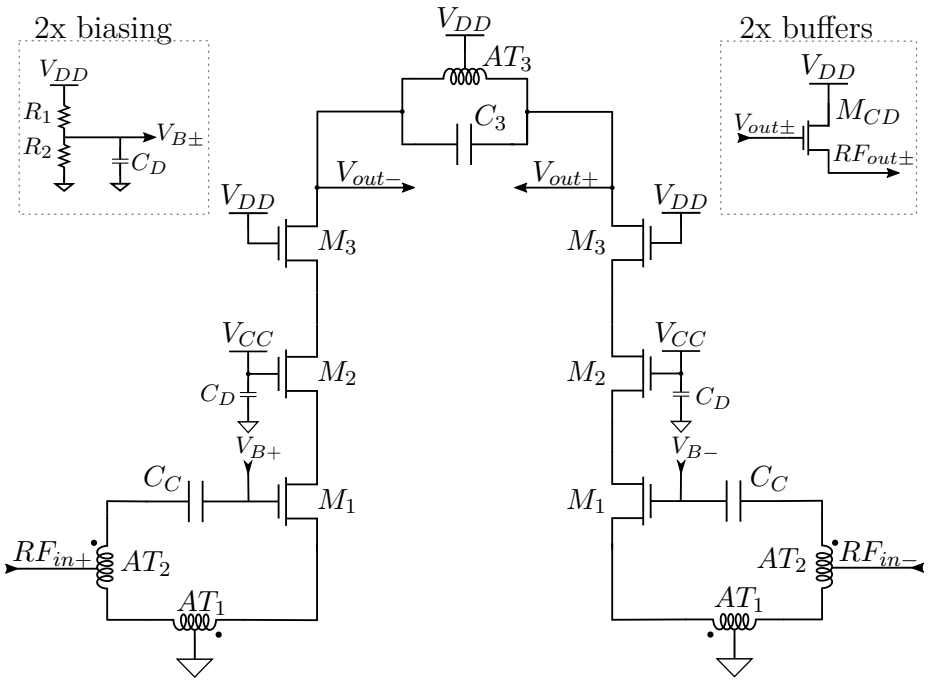

Figure 4.3: Reactive feedback/feedforward LNA

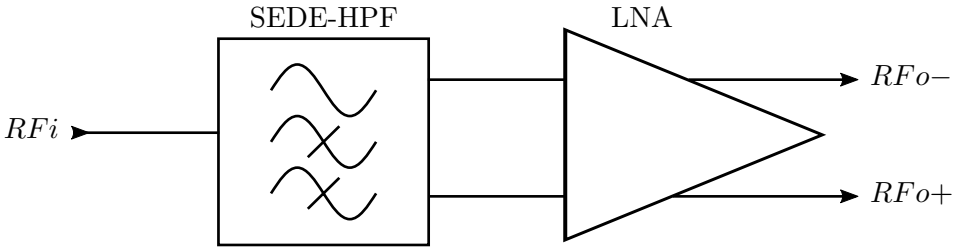

Figure 4.4: Area-optimized RFFE, block level

The area-optimized RFFE comprises of the single-ended to differential (SEDE) HPF from Chapter 2, and the LNA from Chapter 3. No additional modifications were done.

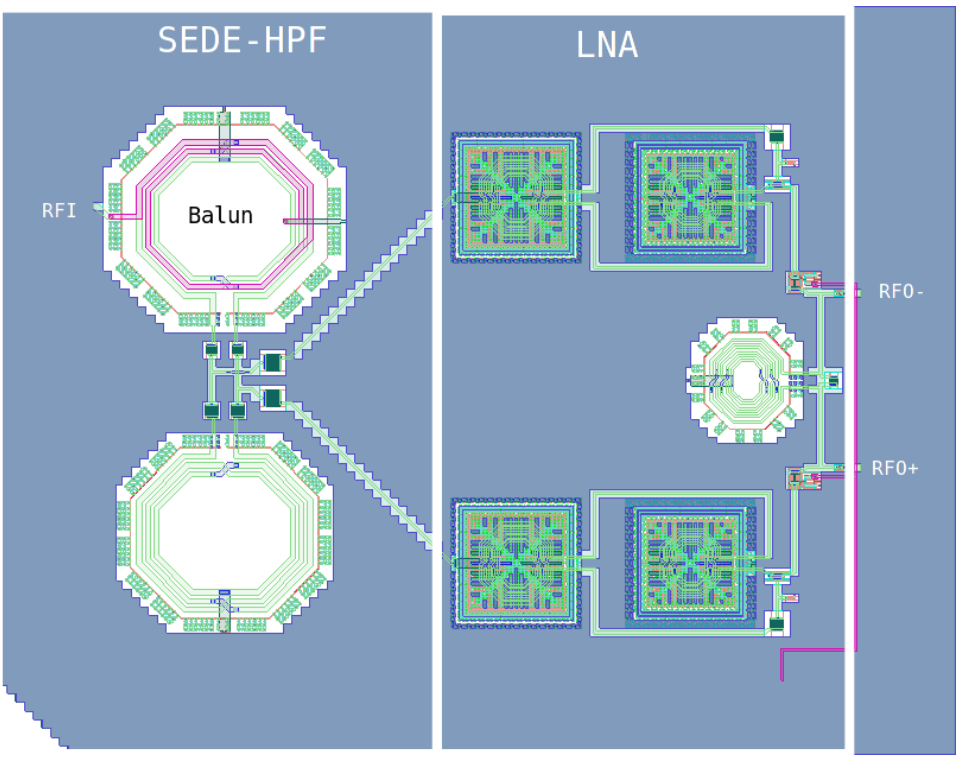

Figure 4.5: Layout of the area-optimized RFFE

4.1.1 Simulation results

The maximum return loss (S_{11}) of the RFFE, for a single-ended source impedance of 50 Ω is measured at 8.375 GHz and is −12.54 dB. The S_{11} −10 dB-bandwidth is 6.5-9.7 GHz. The S_{11} −20 dB-bandwidth is 7.1-7.6 GHz.

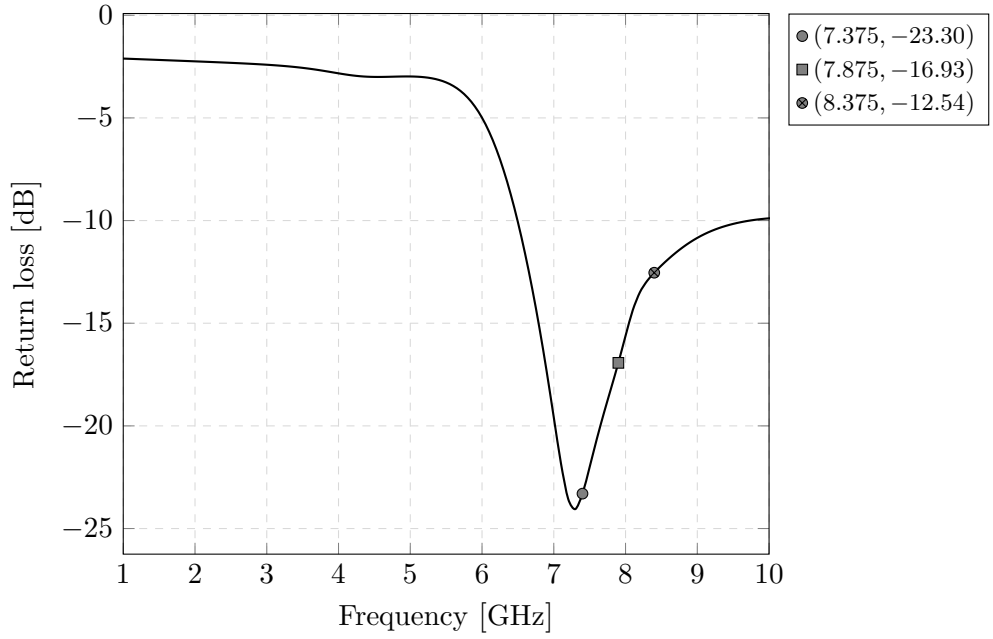

Figure 4.6: S_{11} of the area-optimized RFFE

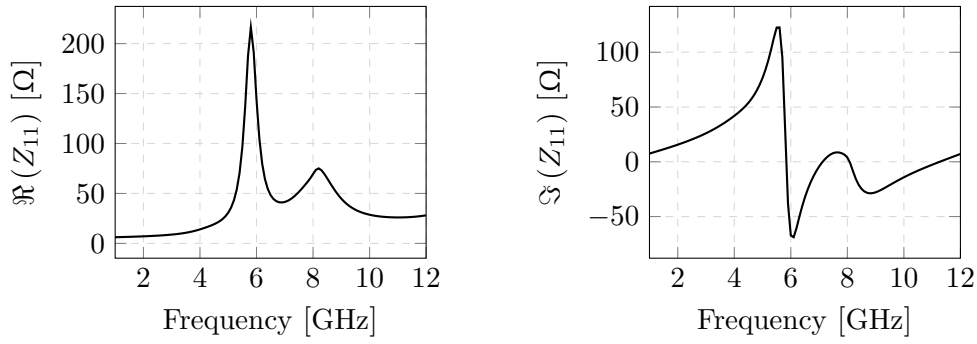

(a) $\Re(Z_{11})$ (b) $\Im(Z_{11})$

Figure 4.7: Real & imaginary input impedance of the area-optimized RFFE

The maximum output return loss (S_{22}) of the RFFE, for a differential load impedance of 100 Ω is measured at 8.375 GHz and is −13.37 dB. The S_{22} −10 dB-bandwidth is 1-10 GHz. The −20 dB-bandwidth is out-of-band ($\leq$ 4.4 GHz).

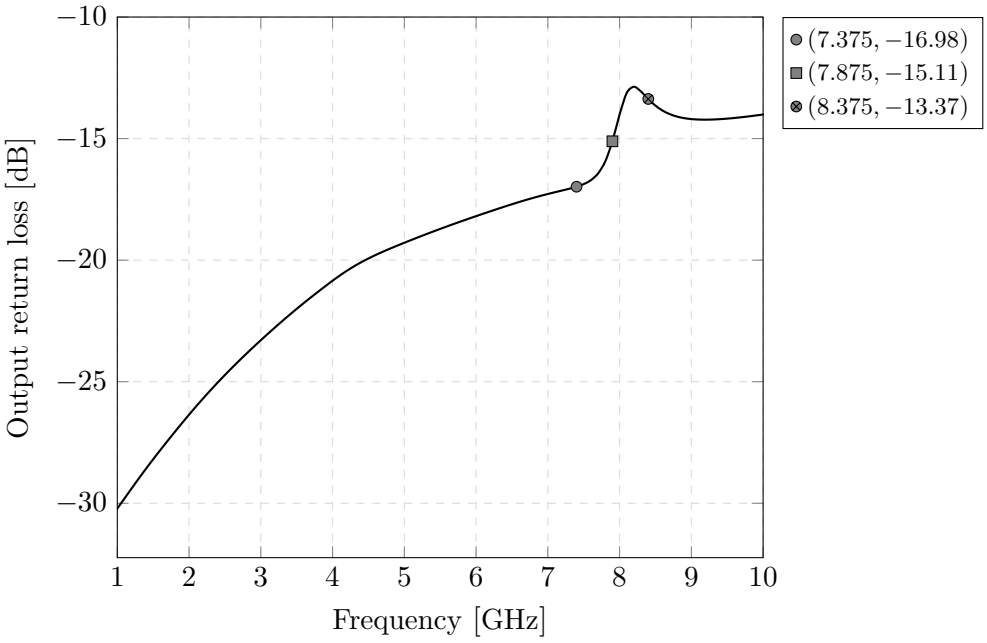

Figure 4.8: S_{22} of the area-optimized RFFE

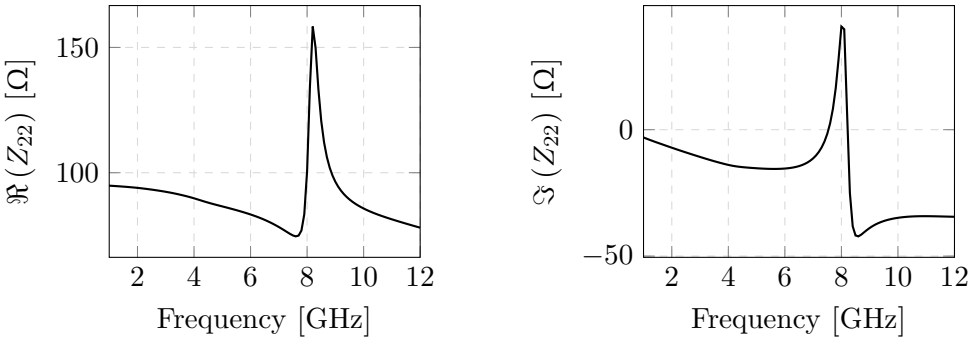

(a) $\Re(Z_{22})$ (b) $\Im(Z_{22})$

Figure 4.9: Real & imaginary output impedance of the area-optimized RFFE

The voltage gain (A_V) is reported as the maximum gain, and the bandwidth is reported as the $-10\,\text{dB}$-bandwidth. The maximum gain at the resonant frequency $8.1\,\text{GHz}$ is $17.39\,\text{dB}$. The $-10\,\text{dB}$ BW is $1.4\,\text{GHz}$. Relative to the resonant frequency the BW is $\pm 700\,\text{MHz}$.
Attenuation at the bands of interest are:

$$\text{Rejection} = \begin{cases} \geq 37.45\,\text{dB}, & f \in [0, 2.4]\,\text{GHz}, \\ \geq 10.97\,\text{dB}, & f \in [2.4, 5.0]\,\text{GHz}, \\ 10.54\,\text{dB}, & f = 5.8\,\text{GHz} \end{cases} \tag{4.1}$$

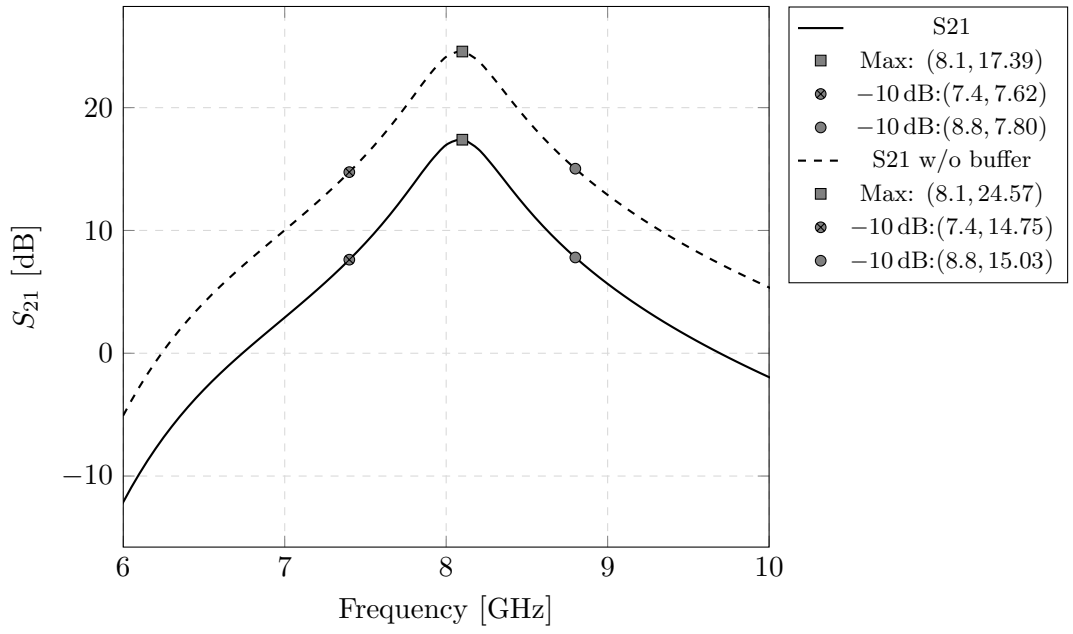

(a) Zoomed in from 6-10 GHz

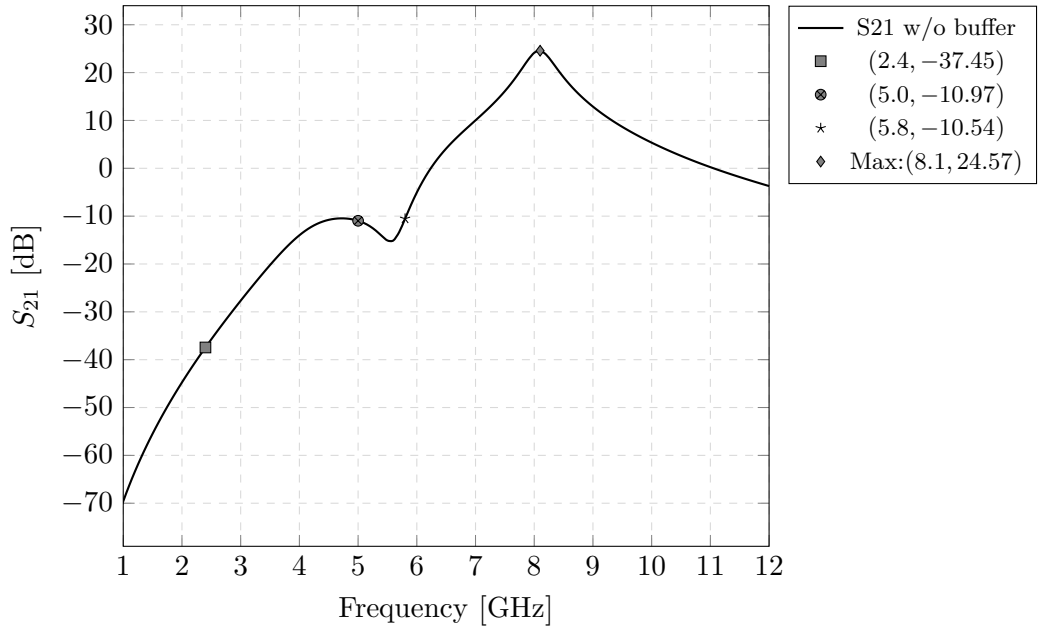

(b) In-band and out-of-band

Figure 4.10: Voltage gain of the area-optimized RFFE

The minimum reverse isolation is -47.42 at 7.375 GHz (passband).

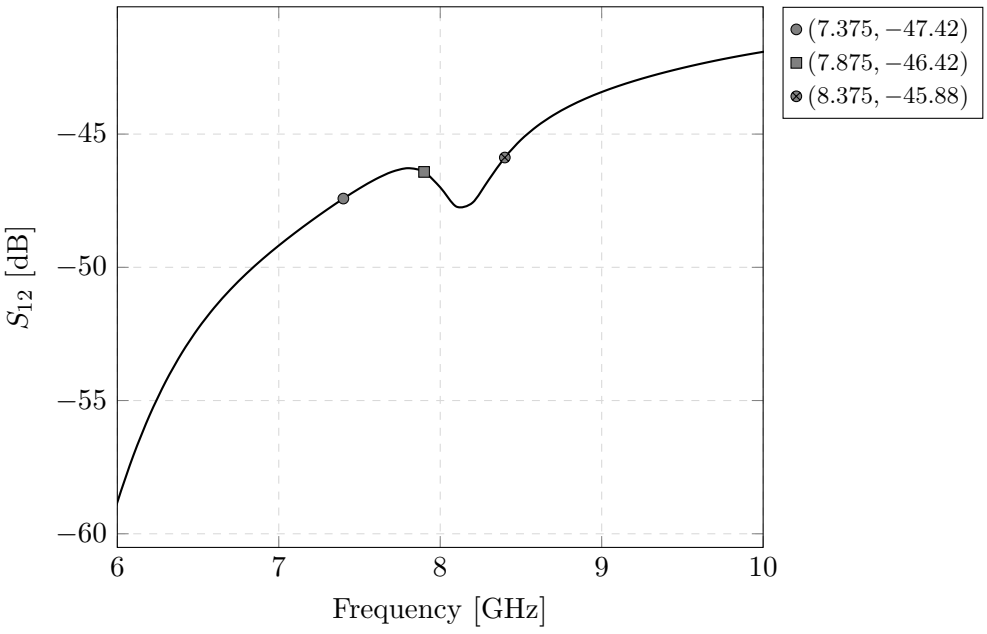

Figure 4.11: Reverse isolation of the area-optimized RFFE

For stability, we use the μ-stability test, if $\mu > 1$, the RFFE is unconditionally stable. The minimum value of μ is $\mu_{min} = 4.18$ at 8.375 GHz (passband).
As shown in Fig. 5.27, we meet the condition for unconditionally stability from 6-10 GHz.

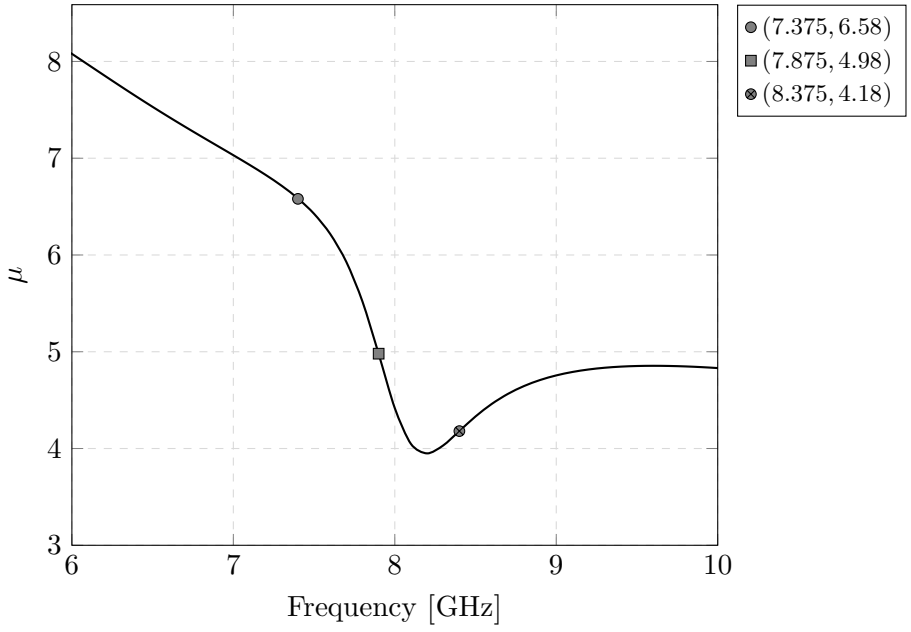

Figure 4.12: μ-factor for stability

The noise figure (NF) in the passband is

	$f_c - 500\,\text{MHz}$	f_c	$f_c + 500\,\text{MHz}$
NF	7.48 dB	6.99 dB	7.02 dB
NF_{min}	7.47 dB	6.95 dB	6.92 dB

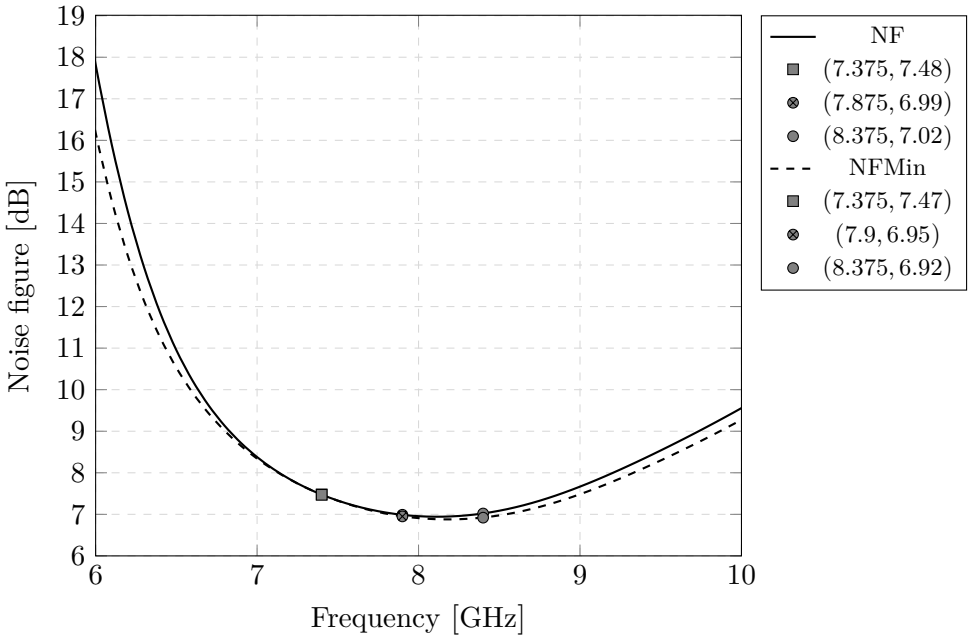

Figure 4.13: Noise figure for the area-optimized RFFE

For the 1 dB compression point (P1dB), we use large signal S-parameters (LSSP), where we sweep the input power, P_{RF}.From Fig. 5.28, the P1dB is -17 dBm, which 13 dB higher than required.

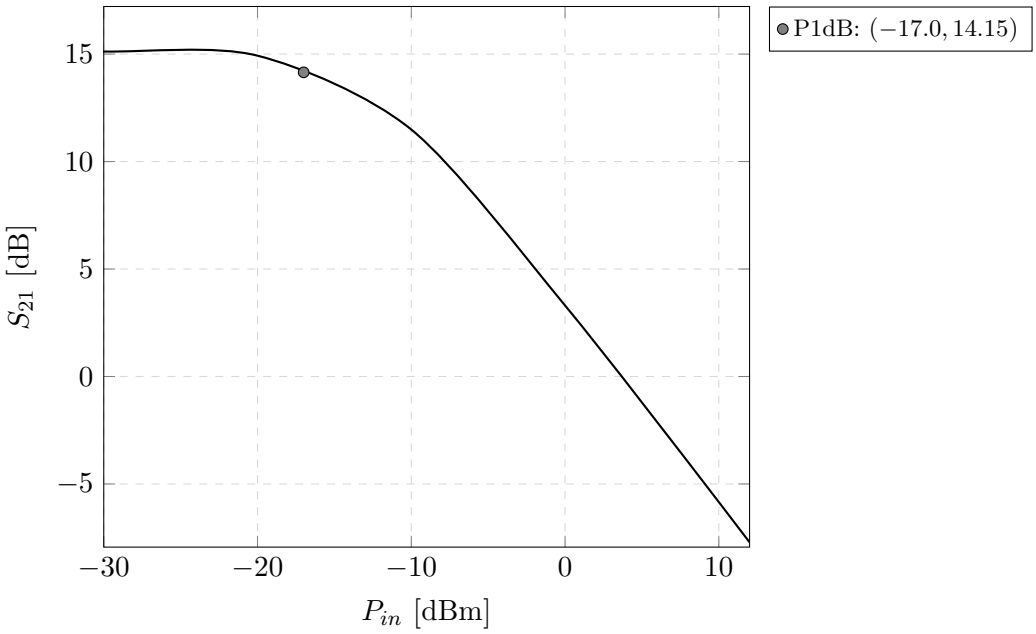

Figure 4.14: Large signal S-parameter, S_{21}, for area-optimized RFFE

The total current consumption, I_{DC} of the area-optimized RFFE in is 10 mA. The active core consumes 5.6 mA and the buffers 4.4 mA.

	Results	Specification
Gain[‡]	24.57 dB	30 dB
Bandwidth[*]	7.4-8.8 GHz	7.375-8.375 GHz
Rejection:		
@ 2.4 GHz	37.45 dB	20 dB
@ 5 GHz	10.97 dB	15 dB
@ 5.8 GHz	10.54 dB	15 dB
S_{11}:		
Minimum[†]	6.5-9.7 GHz	7.375-8.375 GHz
Desired[§]	7.1-7.6 GHz	7.375-8.375 GHz
S_{22}:		
Minimum[†]	1-10 GHz	7.375-8.375 GHz
Desired[§]	$\leq$ 4.4 GHz	7.375-8.375 GHz
Reverse isolation	$\geq$ 47.42 dB	$\geq$ 60 dB
Stability, μ-factor	$\geq$ 4.18	$\geq$ 1
NF	$\leq$ 7.48 dB	$\leq$ 7 dB
P1dB	-22 dBm	-30 dBm
DC current[**]	5.6 mA	6 mA
Area	1.1x0.86 mm^2	
Supply voltage	1.5 V	

[*] -10 dB
[†] ≤ -10 dB
[§] ≤ -20 dB
[**] Active core only
[‡] De-embedded buffers

4.2 Passively reconfigurable RFFE

From literature, we know that full-duplex doubles the spectral capacity compared to half-duplex. Off-chip RF transceivers generally use bulky ferrite circulators to achieve the required TX-RX isolation. For CMOS integration, we rely on non-magnetic circulators with small form factors. In [6], the authors present an active 2-port full-duplex bi-directional frequency converter (BDFC).
The BDFC achieves +25 dB TX-ANT/ANT-RX isolation, with an insertion loss of 3 dB, at a staggering 48 mW power consumption.

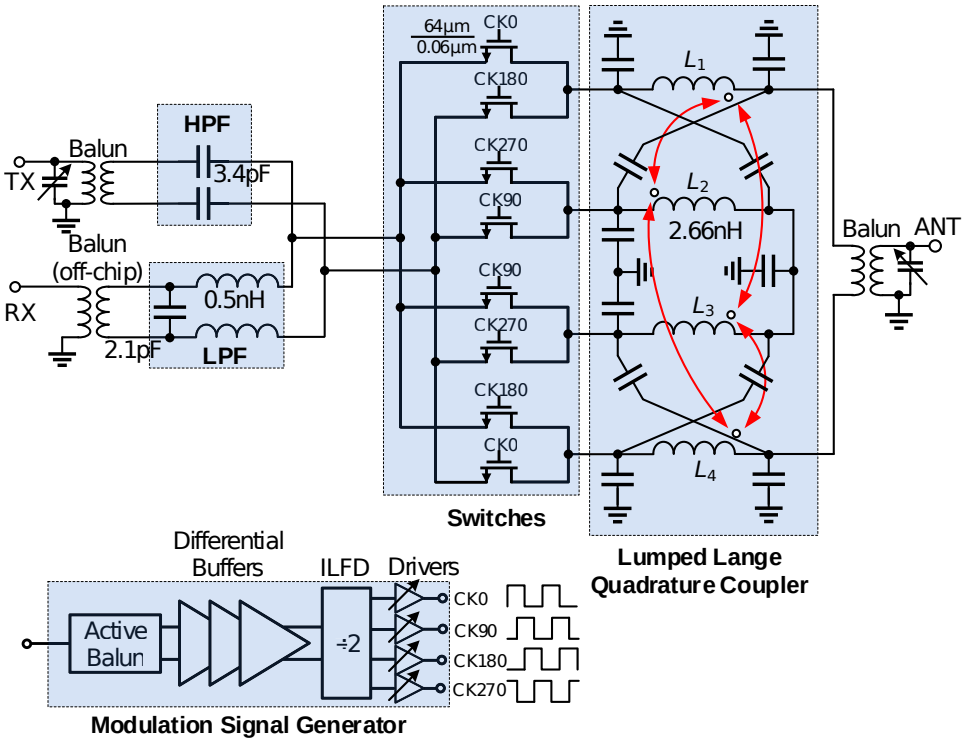

Figure 4.15: Full schematic of the BDFC-based front-end [6]

In contrast to this work, we propose a passively reconfigurable RFFE. For TX-RX isolation, we cancel out the 'common-mode' TX-signal at the output of the LNA by transformer-action. By applying the TX as a common-mode signal across the LC-tank in the LNA, we achieve the required TX-RX cancelllation for full-duplex operation without adding to the power budget.
To transform the TX as a common mode signal, we modify the LNA in Chapter 3. This is shown in Fig. 4.17. A third duplicate (AUX) branch of either of the input-branches is required. One input (say negative CS-stage) is shunted to ground through a switch. The 1st CG-stage is opened (i.e., gate is pulled low). The AUX amplifies a copy of the transmitted signal via the positive branch (TRX) and connects to the drain of the 2nd CG-stage. This gives us the single-ended to pseudo-differential configuration. To ensure that the copy of the transmitted signal is equal

to the 'real' transmitted signal, we ensure that the impedances of the two branches are equal. Thus, assuming perfect match between the TRX branch, the AUX branch, we thus expect the signal at the output of the LNA to be:

$$\begin{aligned} V_{TRX} &= V_{RX|TRX} + V_{TX|TRX} \\ V_{AUX} &= V_{TX|AUX} \\ V_{out} &= A_V \left(V_{TRX} + V_{AUX} \right) \\ &= V_{RX} \cdot A_D + \left(V_{TX|TRX} - V_{TX|AUX} \right) A_{CM} \\ &\approx V_{RX|TRX}, \end{aligned} \tag{4.2}$$

where A_D is the differential gain of the LNA, A_{CM} is the common-mode rejection of the LC-tank. Assuming sufficient common-mode rejection, we will see the single-ended RX signal gained by the differential gain at the output.
We require at least $-20\,\mathrm{dB}$ TX-RX cancellation, i.e. a common-mode rejection of $20\,\mathrm{dB}$. In terms of insertion loss, we have an intrinsic loss of $6\,\mathrm{dB}$ in TX/RX due to the single-ended configuration.
The *passively* reconfigurable RFFE (PR-RFFE) can operate in half-duplex (HD) and full-duplex (FD) mode. In it's natural HD-mode, it is configured as pseudo-differential to pseudo-differential. In FD-mode, it is configured as single-ended to pseudo-differential. The PR-RFFE comprises of the pseudo-differential to pseudo-differential (PDPD) HPF from Chapter 2, and a modified LNA from Chapter 3. In addition, we need to supply a TX-like signal to test the FD-mode, hence a TX-driver was made in addition. This TX-driver was input impedance matched using a $50\,\Omega$ resistance. This TX-driver is not considered as part of the RFFE, but rather a test-structure. Unfortunately, we cannot de-embed the TX-driver.

To ensure amplitude & phase matching between the TRX+-branch and the AUX branch, we have added an additional RC-matching network to the AUX. The RC-matching compensates for the impedance of the HPF seen single-endedly. Ideally, we expect the impedance looking into the interface between the LNA and the HPF to be $25\,\Omega$ ($50\,\Omega \parallel 50\,\Omega$). The added resistance is $40\,\Omega$ and the added capacitance is 1.4 pF.

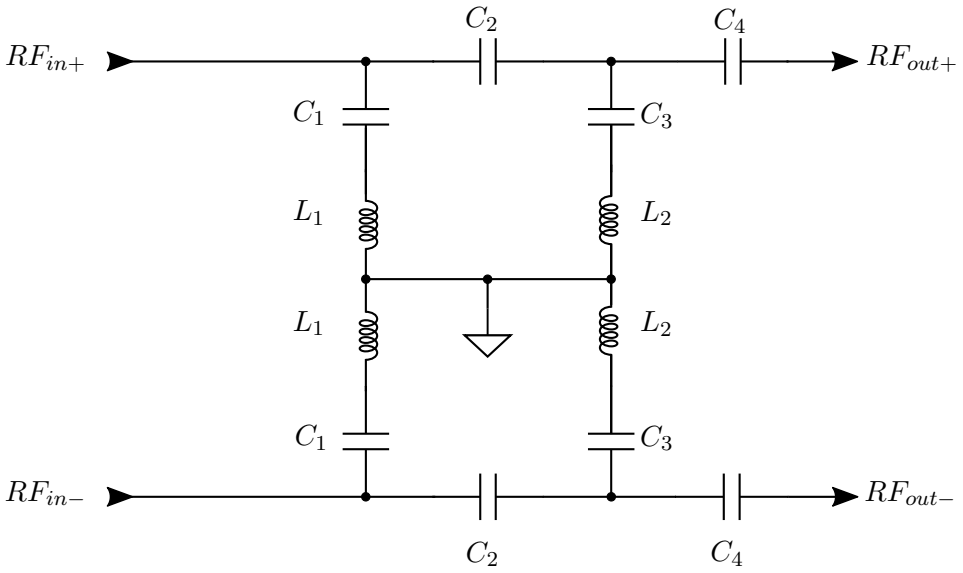

Figure 4.16: PR-RFFE filter, PDPD-HPF from Chapter 2

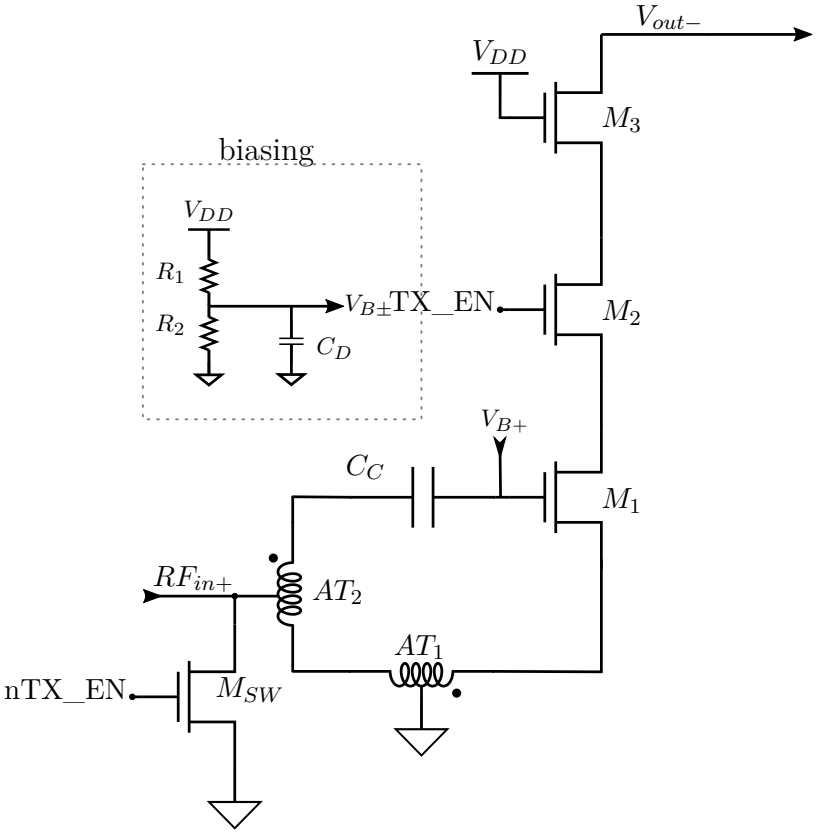

Figure 4.17: PR-RFFE LNA branch for full-duplex mode

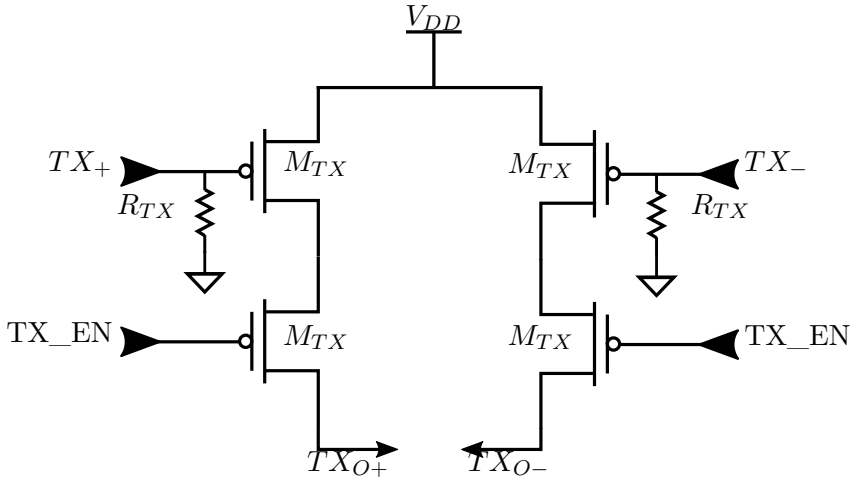

Figure 4.18: PR-RFFE TX-driver stage

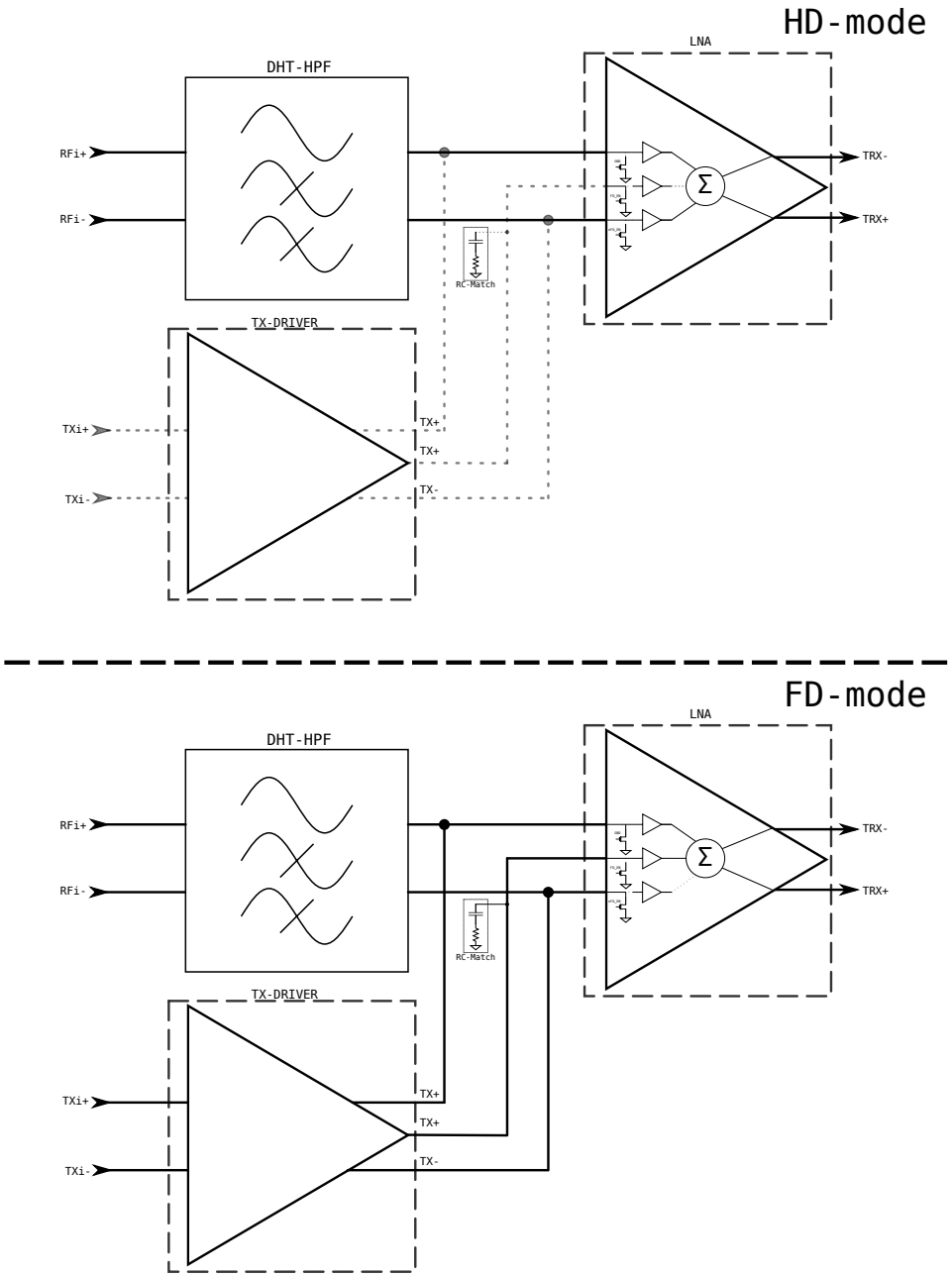

Figure 4.19: PR-RFFE, block level

From Fig. 4.19, we see the total system level for the PR-RFFE. The TX-driver consists of 2×TX-driver stages from Fig. 4.18. The LNA consists of 3×LNA-FD slices from Fig. 4.17 in addition to the summing stage, which is the LC-tank from the LNA in Chapter 3.

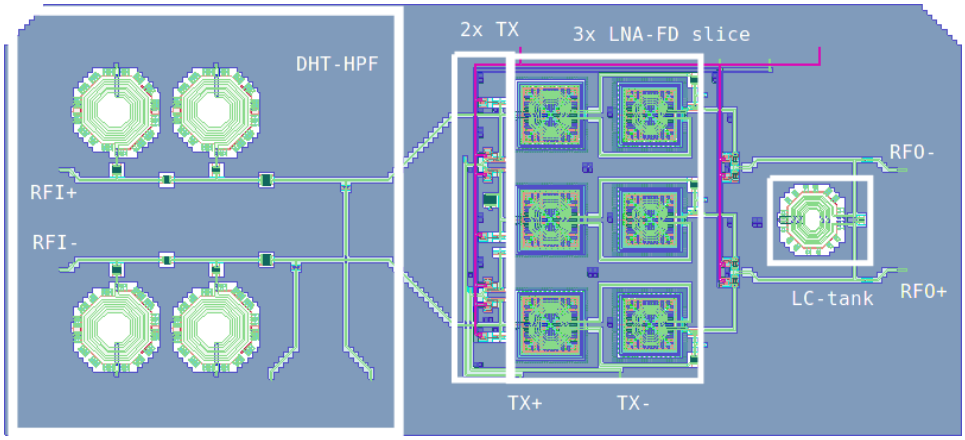

Figure 4.20: Layout PR-RFFE

4.3 Simulation results

The simulation results were done by taking the EMX model of the HPF and the EMX model of the LNA, and then connecting these two together, and we get the following results

4.3.1 Half-duplex mode

The maximum return loss (S_{11}) of the RFFE, for a differential source impedance of 100 Ω is measured at 8.375 GHz and is −15.48 dB. The S_{11} −10 dB-bandwidth is 6.1-8.9 GHz. The S_{11} −20 dB-bandwidth is at a single point 8.1 GHz.

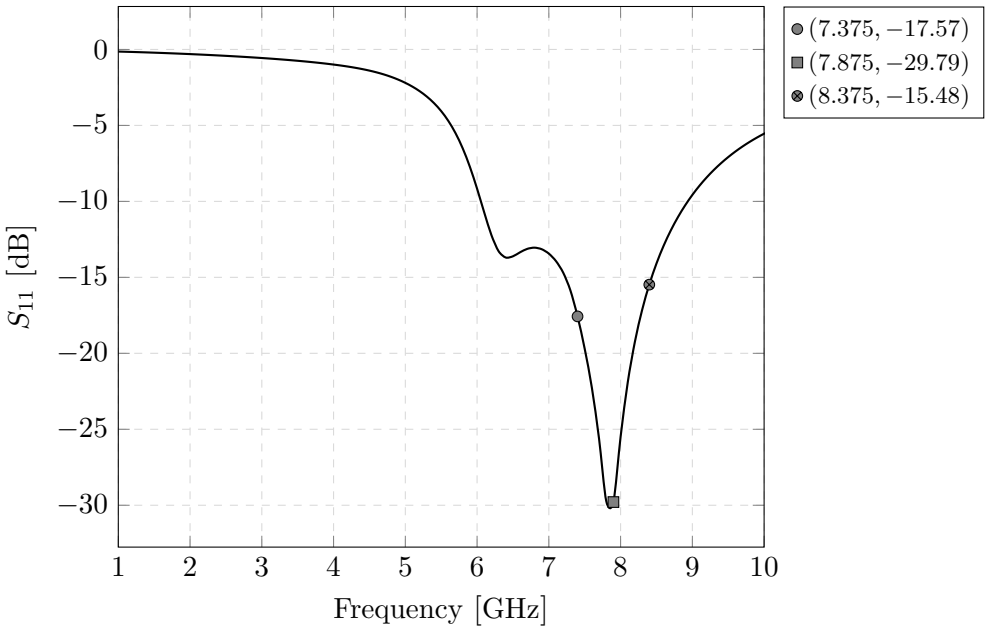

Figure 4.21: S_{11} of the PR-RFFE in HD-mode

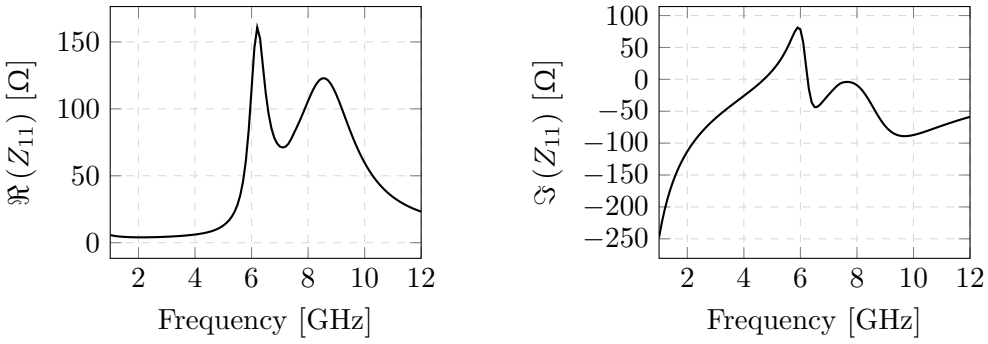

(a) $\Re(Z_{11})$ (b) $\Im(Z_{11})$

Figure 4.22: Real & imaginary input impedances of the PR-RFFE in HD-mode

The maximum output return loss (S_{22}) of the RFFE, for a differential load impedance of 100 Ω is measured at 7.375 GHz and is −10.58 dB. The S_{22} −10 dB-bandwidth is 7.4-10 GHz.

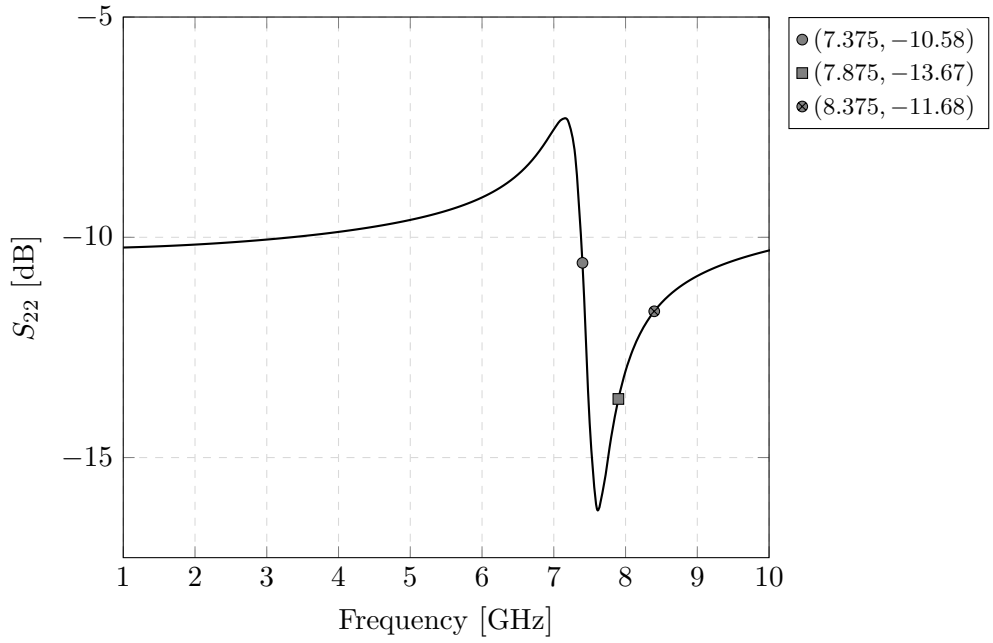

Figure 4.23: S_{22} of the PR-RFFE in HD-mode

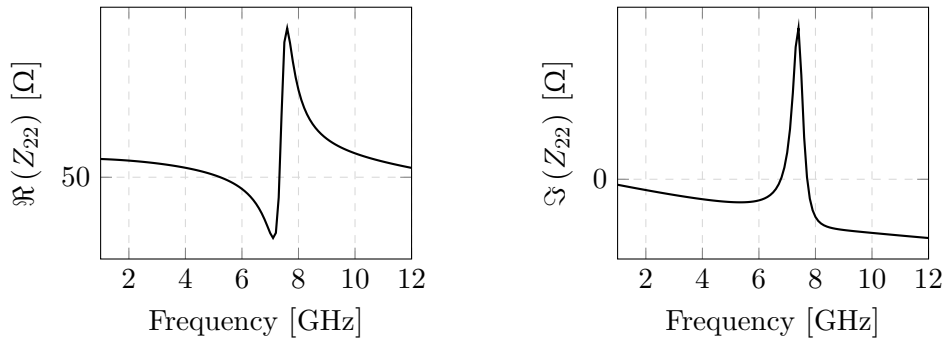

(a) $\Re(Z_{22})$ (b) $\Im(Z_{22})$

Figure 4.24: Real & imaginary output impedances of the PR-RFFE in HD-mode

The voltage gain (A_V) is reported as the maximum gain, and the bandwidth is reported as the $-10\,\text{dB}$-bandwidth. The maximum gain at the resonant frequency $7.4\,\text{GHz}$ is $26.3\,\text{dB}$. The $-10\,\text{dB}$ BW is $1.3\,\text{GHz}$. Relative to the resonant frequency the BW is $\pm 650\,\text{MHz}$.
Attenuation at the bands of interest are:

$$\text{Rejection} = \begin{cases} \geq 27.33\,\text{dB}, & f \in [0, 2.4]\,\text{GHz}, \\ \geq 18.71\,\text{dB}, & f \in [2.4, 5.0]\,\text{GHz}, \\ -6.11\,\text{dB}, & f = 5.8\,\text{GHz} \end{cases} \tag{4.3}$$

The aforementioned meets specifications.

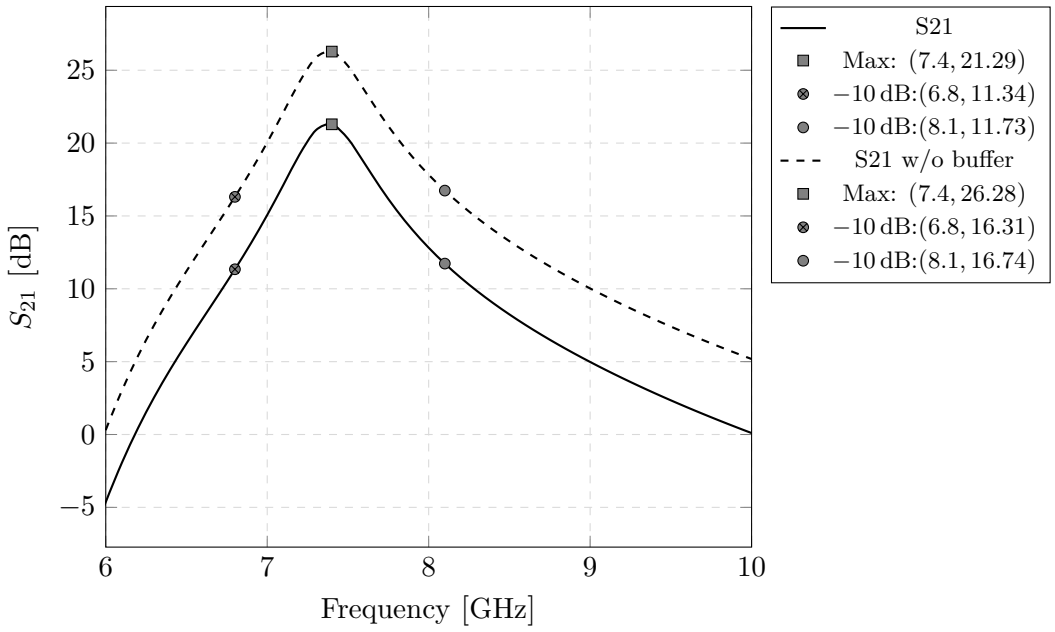

(a) Zoomed in from 6-10 GHz

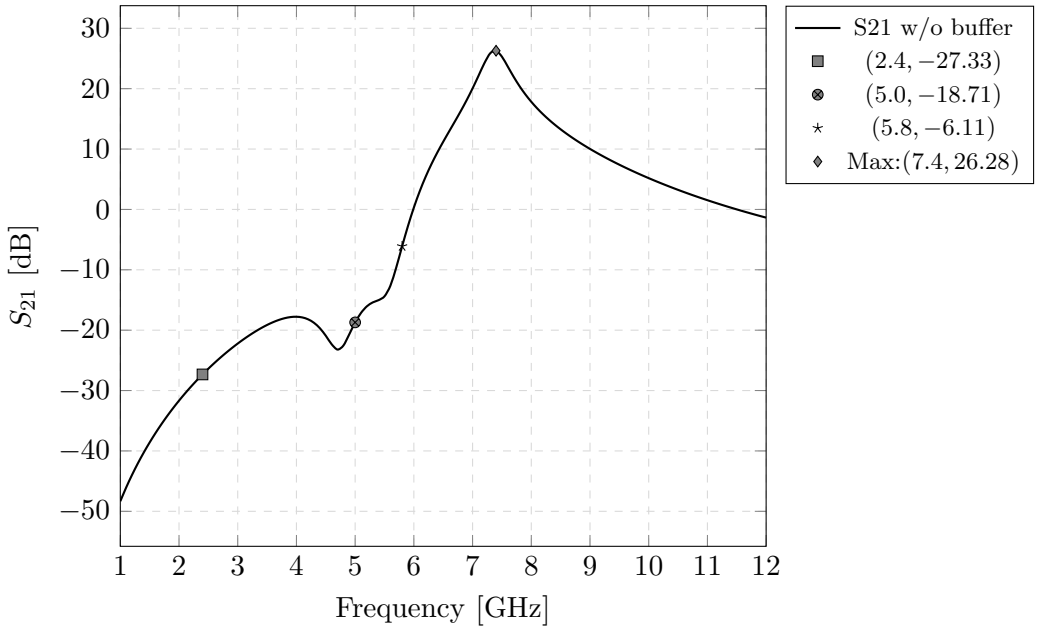

(b) In-band and out-of-band

Figure 4.25: Voltage gain of the PR-RFFE in HD-mode

The minimum reverse isolation is at 7.375 GHz, and is −70.07 dB.

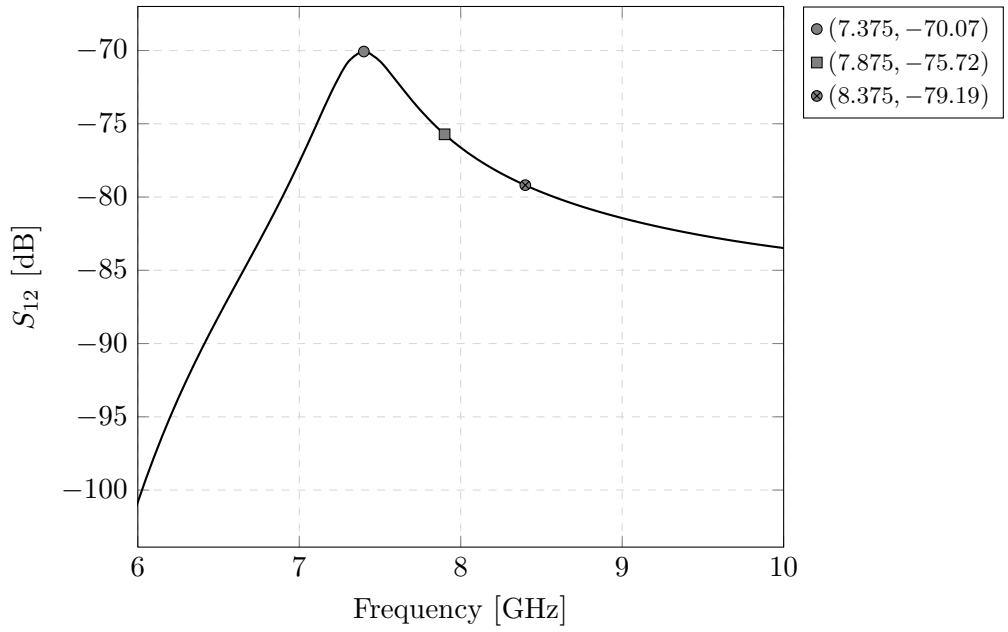

Figure 4.26: Reverse isolation of the PR-RFFE in HD-mode

For stability, we use the μ-stability test, if $\mu > 1$, the RFFE is unconditionally stable. The minimum value of μ is $\mu_{min} = 3.95$ at 7.375 GHz (passband).
As shown in Fig. 5.8, we meet the condition for unconditionally stability from 6-10 GHz.

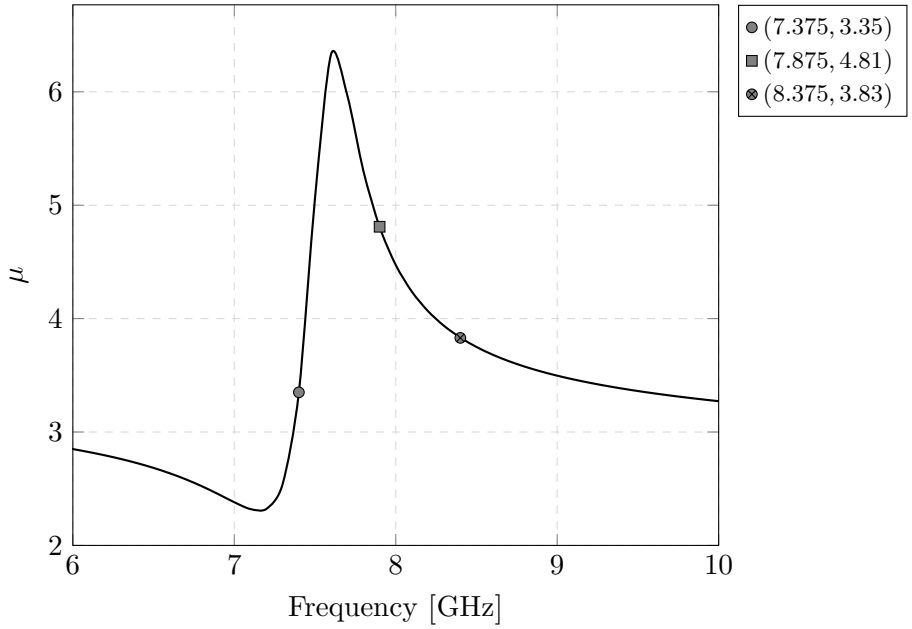

Figure 4.27: μ-factor

The noise figure (NF) in the passband is:

	$f_c - 500\,\text{MHz}$	f_c	$f_c + 500\,\text{MHz}$
NF	5.68 dB	5.41 dB	5.54 dB
NF_{min}	5.68 dB	5.37 dB	5.41 dB

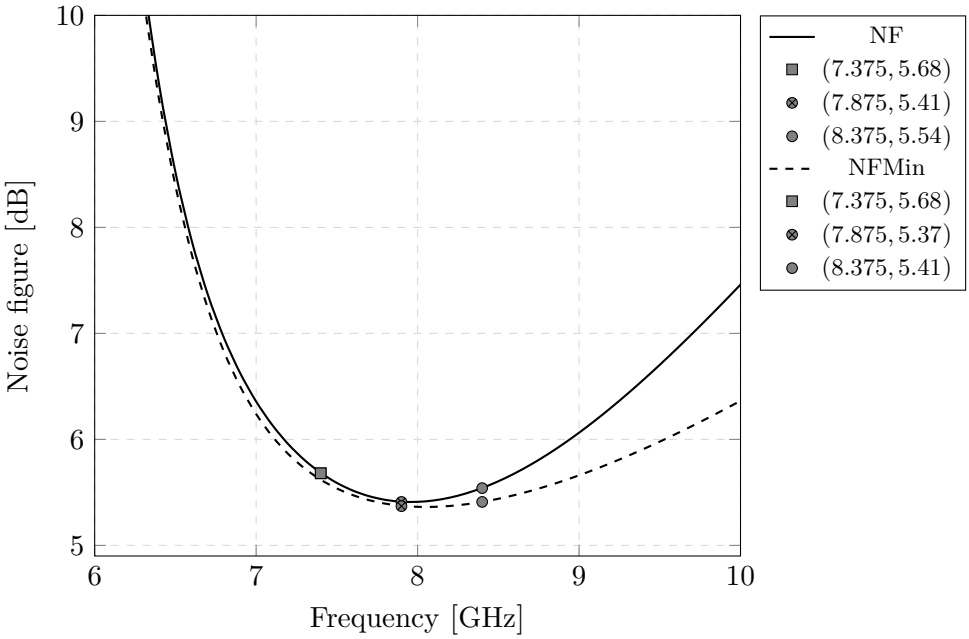

Figure 4.28: Noise figure for the PR-RFFE in HD-mode

For the 1 dB compression point (P1dB), we use large signal S-parameters (LSSP), where we sweep the input power, P_{RF}. From Fig. 5.9, the P1dB is -16 dBm, which is 14 dB higher than required.

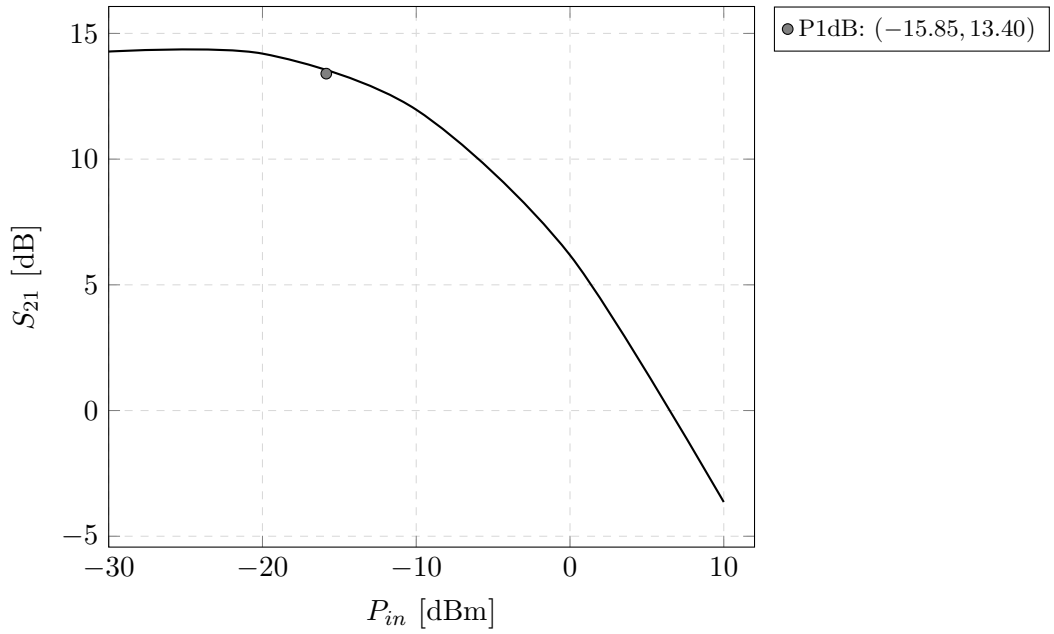

Figure 4.29: Large signal S-parameter, S_{21}, for PR-RFFE in HD-mode

The total current consumption, I_{DC} of the PR-RFFE in HD-mode is 27 mA. The active core consumes 7 mA, and the buffers 20 mA.

4.3.2 Full-duplex mode

The maximum return loss (S_{11}) of the RFFE, for a differential source impedance of 50 Ω is measured at 7.375 GHz and is −17.86 dB. The S_{11} −10 dB-bandwidth is 6.2-9.2 GHz. The S_{11} −20 dB-bandwidth is 7.6-8.2 GHz.

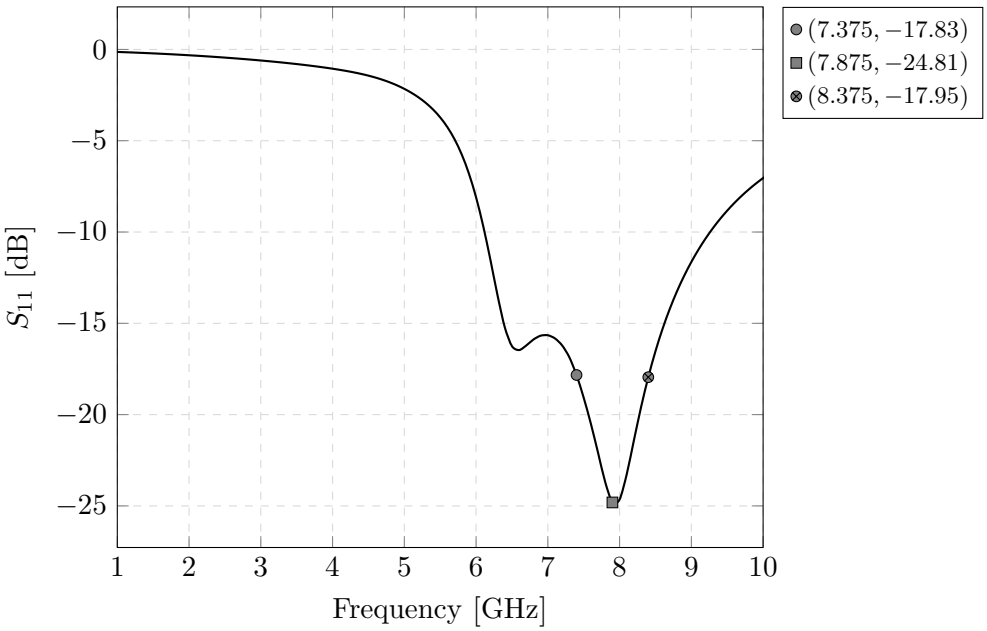

Figure 4.30: S_{11} of the PR-RFFE in FD-mode

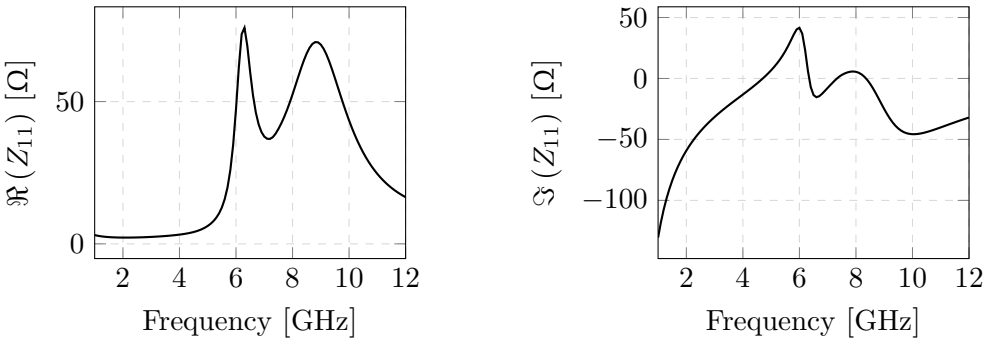

(a) $\Re(Z_{11})$ (b) $\Im(Z_{11})$

Figure 4.31: Real & imaginary input impedance of the PR-RFFE in FD-mode

The maximum output return loss (S_{22}) of the RFFE, for a differential load impedance of 100 Ω is measured at 7.375 GHz and is −10.61 dB. The S_{22} −10 dB-bandwidth is 7.4-10 GHz.

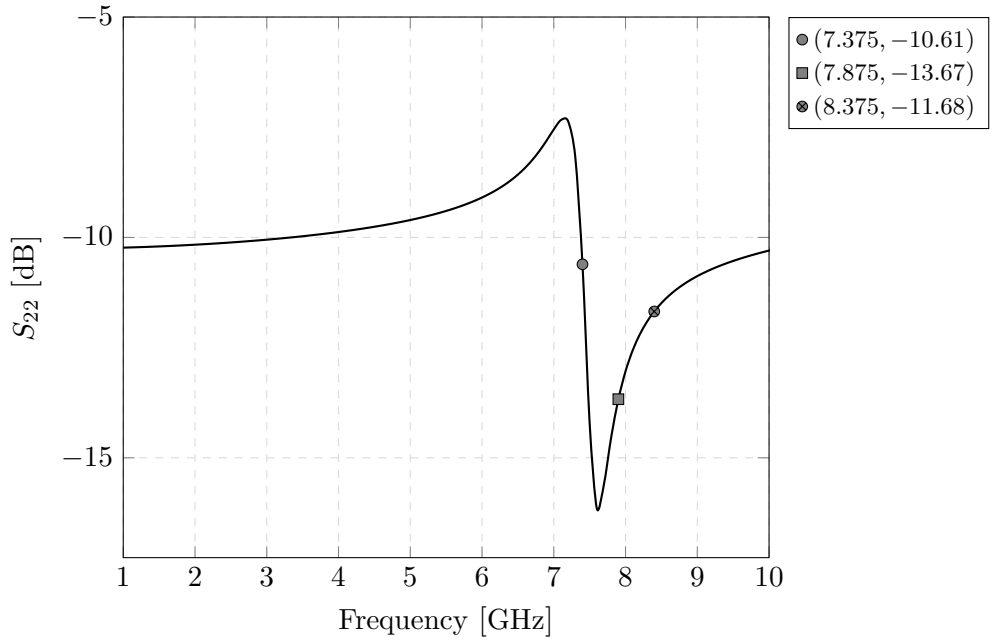

Figure 4.32: S_{22} of the PR-RFFE in FD-mode

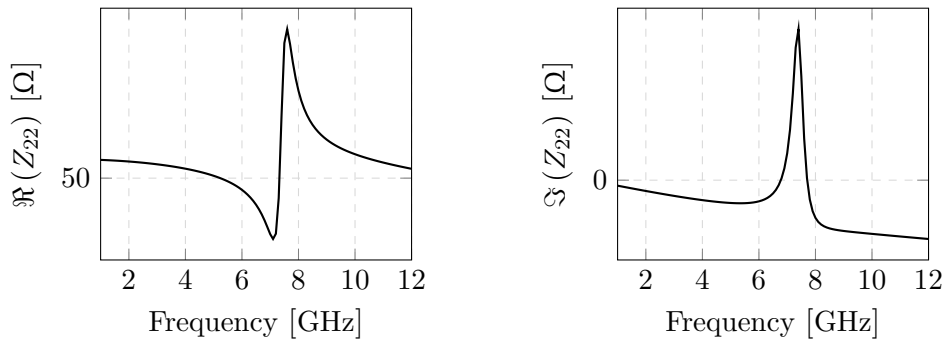

(a) $\Re(Z_{22})$ (b) $\Im(Z_{22})$

Figure 4.33: Real & imaginary output impedance of the PR-RFFE in FD-mode

The maximum input return loss for TX (S_{33}) of the RFFE, for a differential source impedance of 100 Ω is measured at 8.375 GHz and is −11.56 dB. The S_{33} −10 dB-bandwidth is 1-10 GHz.

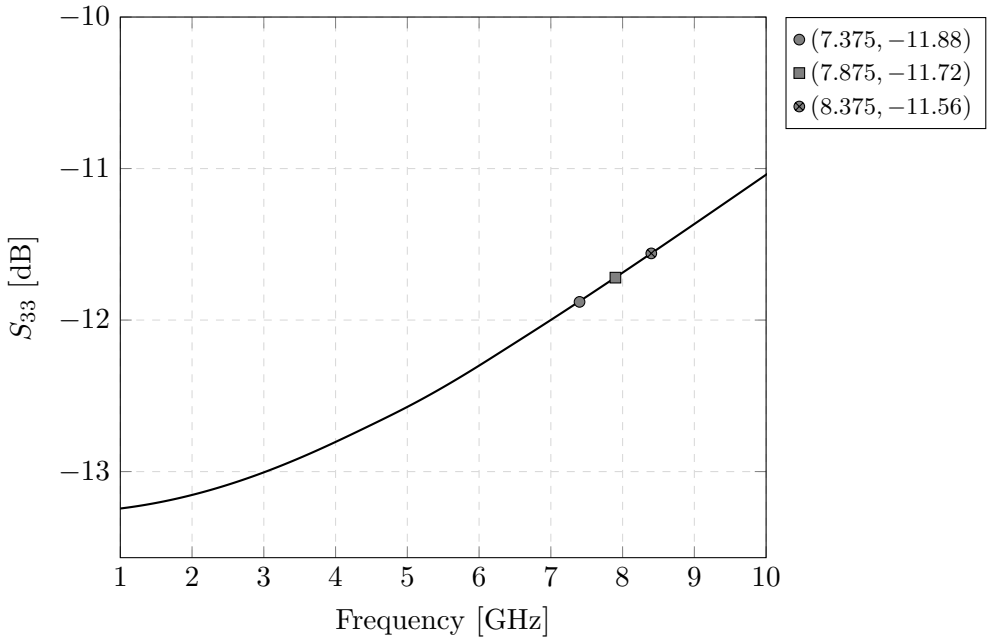

Figure 4.34: S_{33} of the PR-RFFE in FD-mode

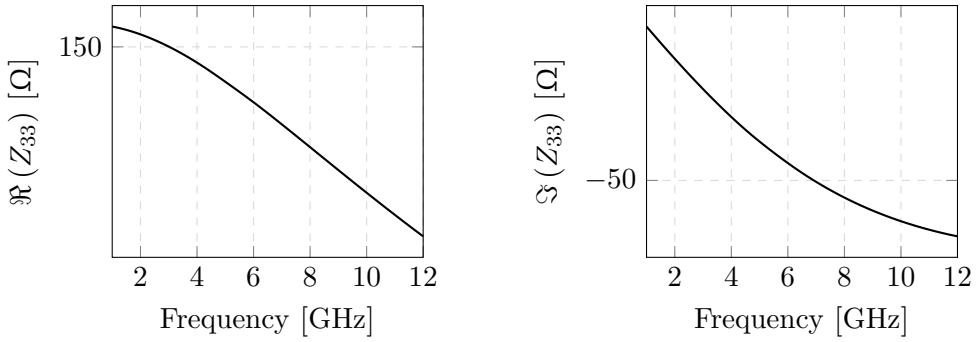

(a) $\Re(Z_{33})$ (b) $\Im(Z_{33})$

Figure 4.35: Real & imaginary input impedances on TX port of the PR-RFFE in FD-mode

The voltage gain (A_V) is reported as the maximum gain, and the bandwidth is reported as the -10 dB-bandwidth. The maximum gain at the resonant frequency 7.4 GHz is 23.2 dB. The -10 dB BW is 1.3 GHz. Relative to the resonant frequency the BW is ± 650 MHz.
Attenuation at the bands of interest are:

$$\text{Rejection} = \begin{cases} \leq 30.15\,\text{dB}, \ f \in [0, 2.4]\,\text{GHz}, \\ \leq 21.87\,\text{dB}, \ f \in [2.4, 5.0]\,\text{GHz}, \\ 10\,\text{dB}, \ f = 5.8\,\text{GHz} \end{cases} \tag{4.4}$$

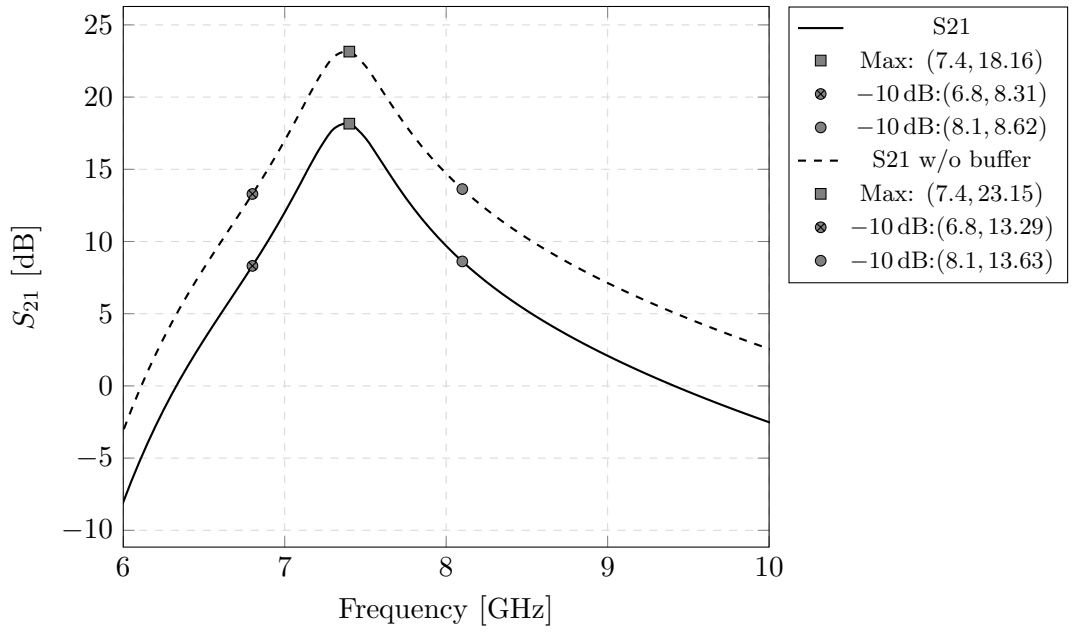

(a) Zoomed in from 6-10 GHz

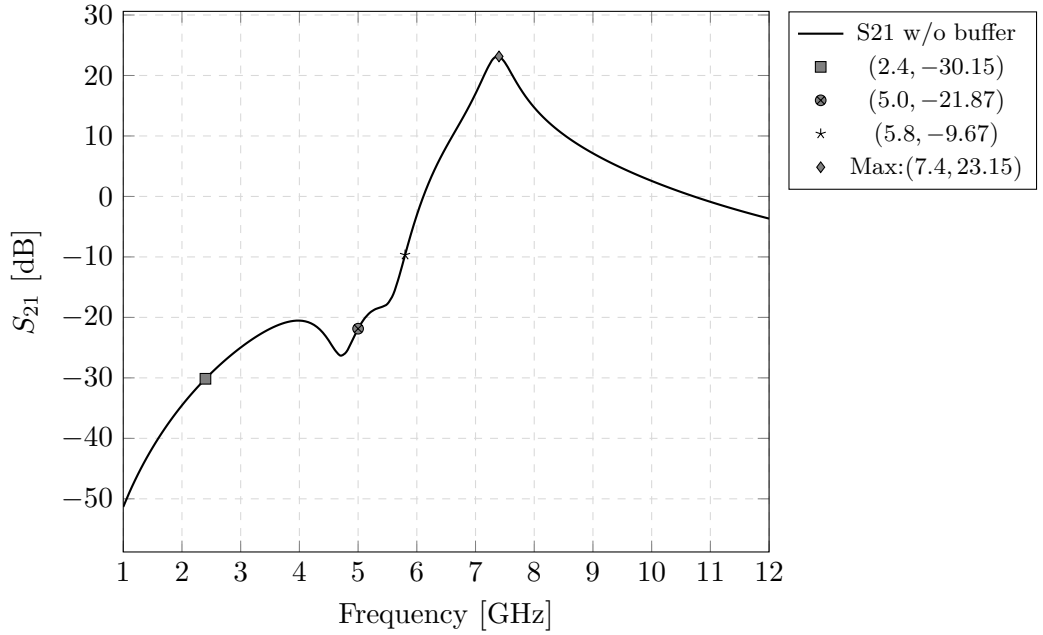

(b) In-band and out-of-band

Figure 4.36: Voltage gain of the PR-RFFE in FD-mode

The voltage gain from TX to the RX port ($A_{V|TX-RX}$) is reported as the maximum gain. The maximum gain is −9.44 dB at the resonance frequency of the LNA (7.4 GHz). The maximum gain looking into the antenna from the TX is $A_{V|TX-ANT} = -15.1$ dB. Thus, the TX-RX isolation is:

$$A_{V|TX-RX} = (S_{23} + |S_{13}|) - S_{21} \tag{4.5}$$

where S_{23} is the unwanted forward transmission gain from TX to RX, S_{13} is the interface loss from TX to RX, and S_{21} is the voltage gain. From Figs. 5.16 and 5.17, we have:

$$A_{V|TX-RX} = (-9.44\,\text{dB} + |-15.09\,\text{dB}|) - 18.16\,\text{dB} = -12.51\,\text{dB},$$

or $\approx$ 12.5 dB cancellation. Due to the high loss at the interface, it is difficult to de-embed whether this is the actual cancellation or not.

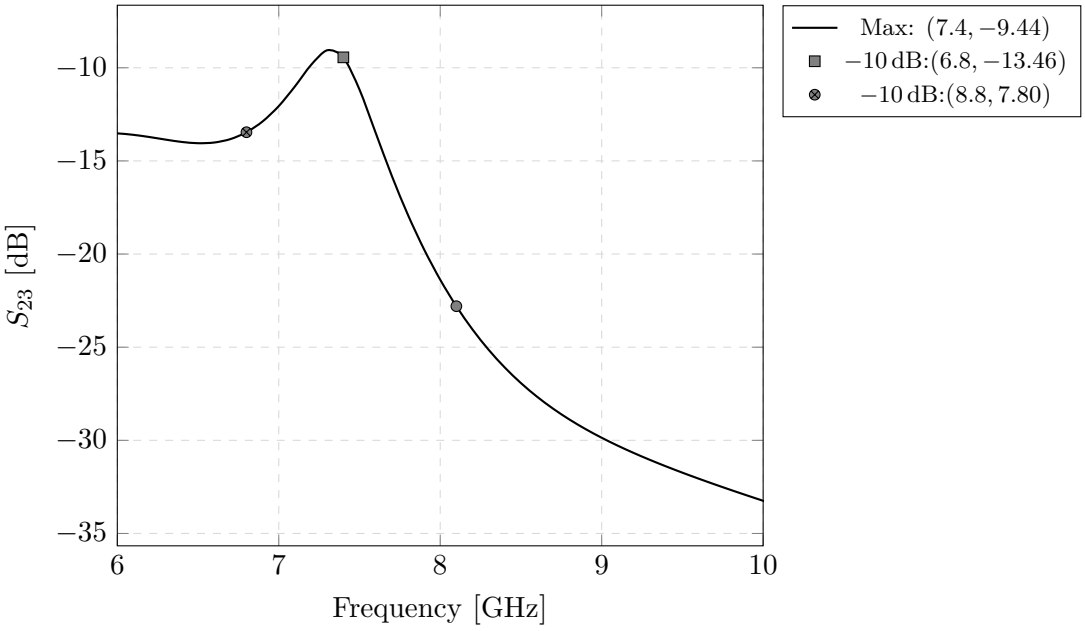

(a) TX to RX

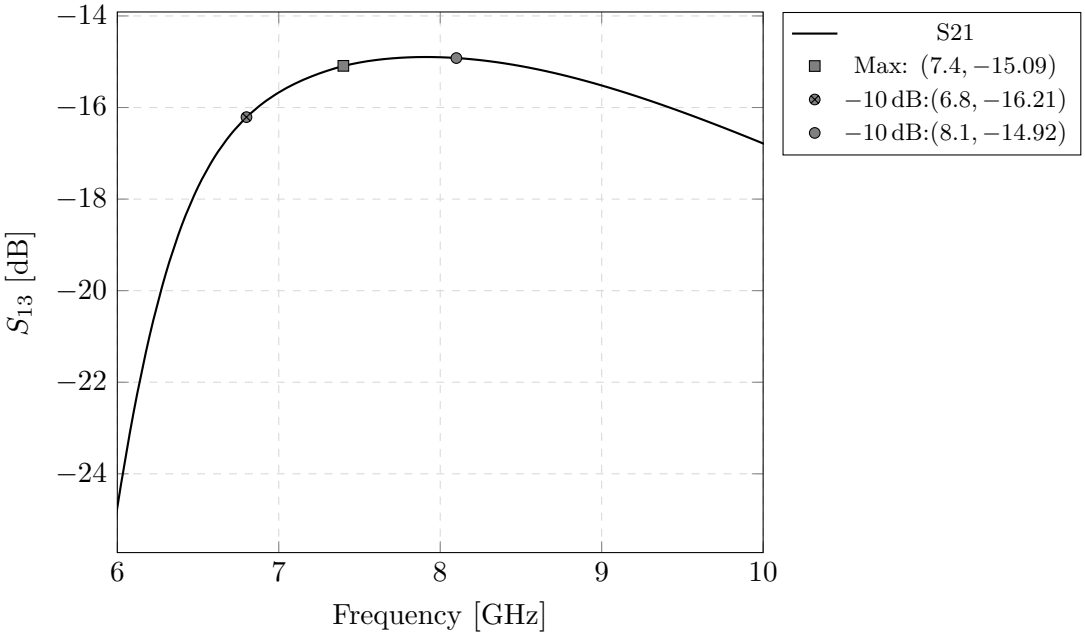

(b) TX to ANT

Figure 4.37: Forward transmission gain, using TX as input port

The minimum reverse isolation is -73.31 at 7.375 GHz (passband).

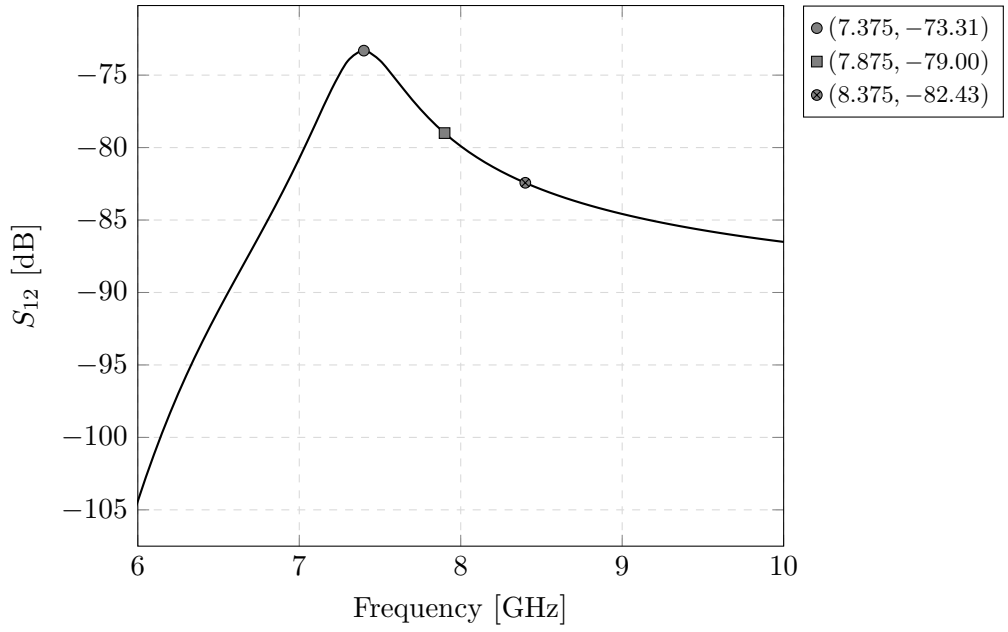

Figure 4.38: Reverse isolation of the area-optimized RFFE

For stability, we use the μ-stability test, if $\mu > 1$, the RFFE is unconditionally stable. The minimum value of μ is $\mu_{min} = 3.38$ at 7.375 GHz (passband). As shown in Fig. 4.40, we meet the condition for unconditionally stability from 6-10 GHz.

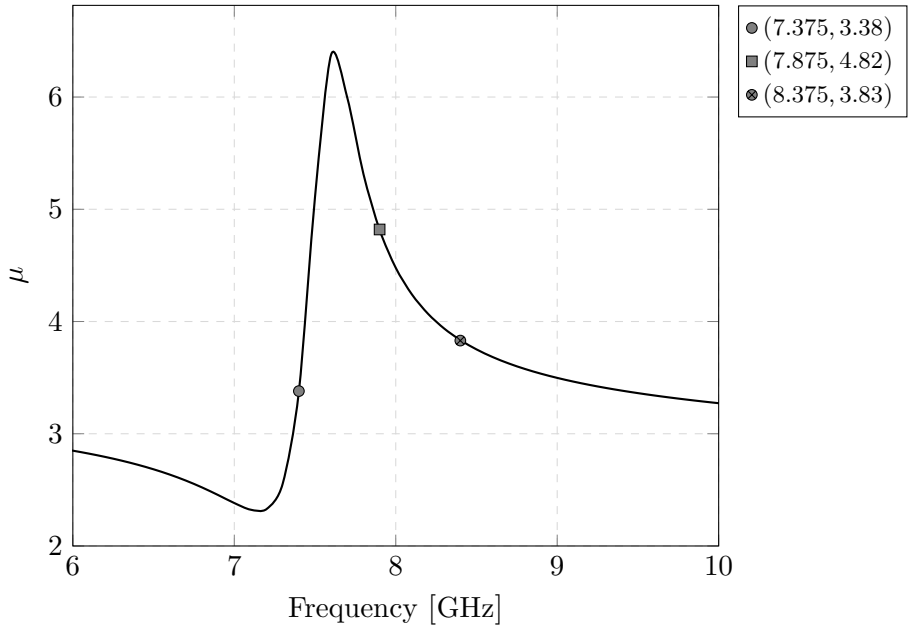

Figure 4.39: μ-factor for stability

The noise figure (NF) in the passband is:

	$f_c - 500\,\text{MHz}$	f_c	$f_c + 500\,\text{MHz}$
NF	9.76 dB	9.46 dB	9.5 dB
NF_{min}	9.75 dB	9.45 dB	9.40 dB

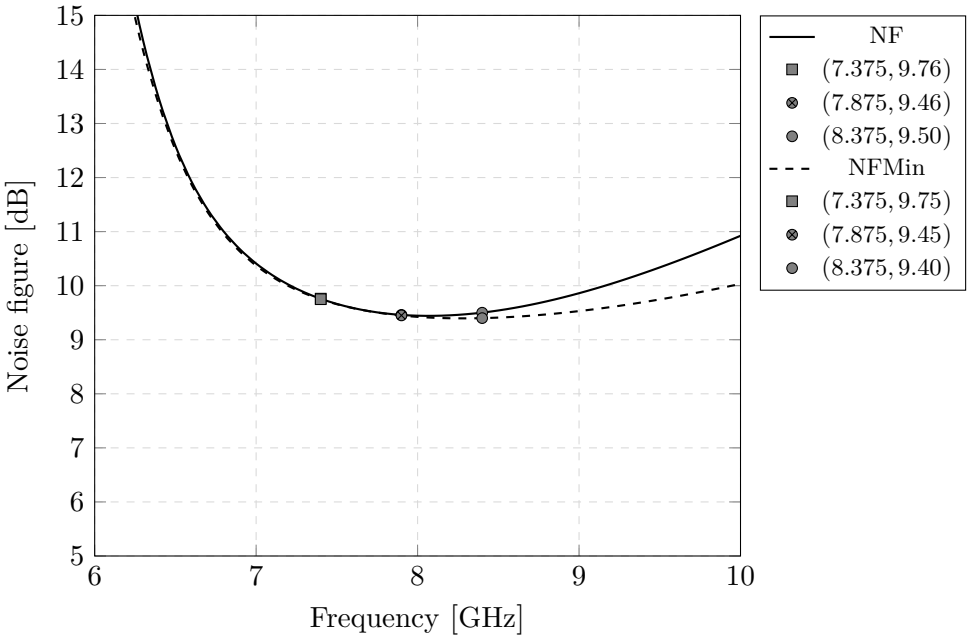

Figure 4.40: Noise figure for the PR-RFFE in FD-mode

For 1 dB compression point (P1dB), we use large signal S-parameters (LSSP), where we sweep the input power, P_{RF}. From Fig. 5.20, the P1dB is -10.8 dBm, which is 20 dB higher than required.

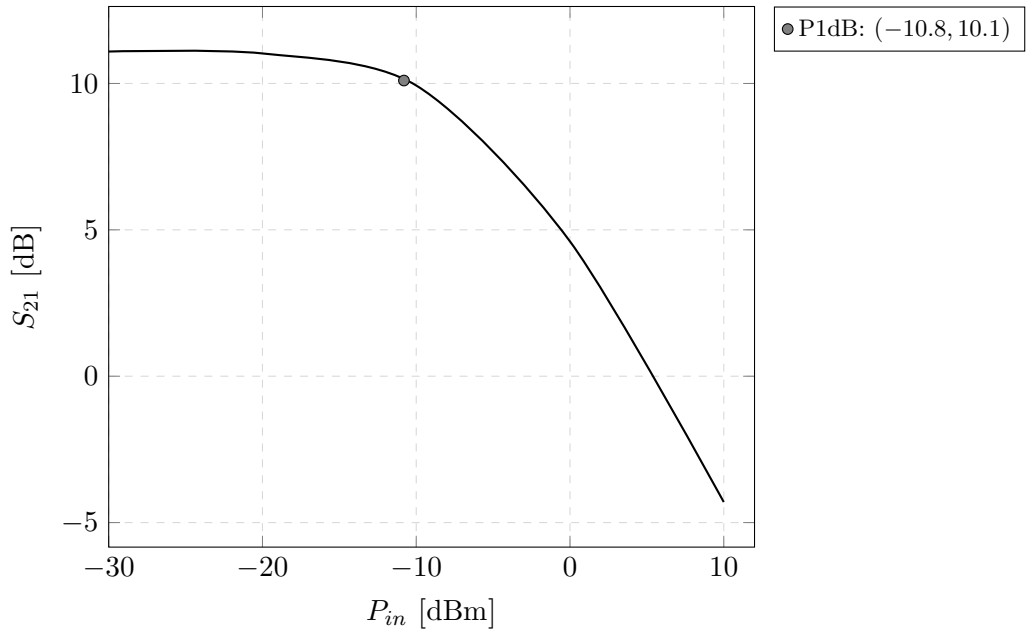

Figure 4.41: Large signal S-parameter, S_{21}, PR-RFFE in FD-mode

The total current consumption, I_{DC} of the PR-RFFE in FD-mode is 37.4 mA. The active core consumes 7.3 mA,the buffers 20 mA and the TX-drivers 10 mA.

	Results		Specification
	HD	FD	
Gain‡	26.8 dB	13.7 dB	≥ 30 dB
Bandwidth*	6.7-7.9 GHz	6.6-8.0 GHz	7.375-8.375 GHz
Rejection:			
@ 2.4 GHz	27.33 dB	30.15 dB	20 dB
@ 5 GHz	18.71 dB	21.87 dB	20 dB
@ 5.8 GHz	6.1 dB	9.67 dB	15 dB
S_{11}:			
Minimum†	6.1-8.9 GHz	6.2-9.2 GHz	7.375-8.375 GHz
Desired§	8.1 GHz	7.6-8.2 GHz	7.375-8.375 GHz
S_{22}:			
Minimum†	7.4-10 GHz	7.4-10 GHz	7.375-8.375 GHz
Desired§	N/A	N/A	7.375-8.375 GHz
S_{33}:			
Minimum†	N/A	1-10 GHz	7.375-8.375 GHz
Desired§	N/A	≤ 2.6 GHz	7.375-8.375 GHz
Reverse isolation	≥ 70 dB	≥ 50 dB	≥ 60 dB
TX-RX isolation	N/A	5 dB	20 dB
Stability, μ-factor	≥ 3.35	≥ 4.46	≥ 1
NF	≤ 5.68 dB	≤ 9.76 dB	≤ 6 dB
P1dB	−19 dBm	−22.1 dBm	−30 dBm
DC current**	7 mA	7.3 mA	6 mA
Area		1.92x0.86 mm^2	
Supply voltage		1.5 V	

* −10 dB
† ≤ −10 dB
§ ≤ −20 dB
** Active core only
‡ De-embedded buffers

4.3.3 Summary

The passively reconfigurable RFFE consumes no additional power, but has an intrinsic loss of 6 dB because of the single-ended operation. Mismatch (including impedance) between the TRX and AUX branches will deteriorate the figure-of-merit, i.e. TX-RX isolation. The area efficient RFFE is optimal for single-ended antenna use. It comprises a single harmonic trap, out-of-band rejection is traded-off.

	PR-RFFE		AO-RFFE
	HD	FD	
Gain[‡]	26.8 dB	13.7 dB	24.57 dB
Bandwidth[*]	6.7-7.9 GHz	6.6-8.0 GHz	7.4-8.8 GHz
Rejection:			
@ 2.4 GHz	27.33 dB	30.15 dB	37.45 dB
@ 5 GHz	18.71 dB	21.87 dB	10.97 dB
@ 5.8 GHz	6.1 dB	9.67 dB	10.54 dB
S_{11}:			
Minimum[†]	6.1-8.9 GHz	6.2-9.2 GHz	6.5-9.7 GHz
Desired[§]	8.1 GHz	7.6-8.2 GHz	7.1-7.6 GHz
S_{22}:			
Minimum[†]	7.4-10 GHz	7.4-10 GHz	1-10 GHz
Desired[§]	N/A	N/A	$<$ 4.4 GHz
S_{33}:			
Minimum[†]	N/A	1-10 GHz	N/A
Desired[§]	N/A	$\leq$ 2.6 GHz	N/A
Reverse isolation	$\geq$ 70 dB	$\geq$ 50 dB	$\geq$ 47.42 dB
TX-RX isolation	N/A	$\geq$ 12.51 dB	N/A
Stability, μ-factor	$\geq$ 3.35	$\geq$ 4.46	$\geq$ 4.18
NF	$\leq$ 5.68 dB	$\leq$ 9.76 dB	$\leq$ 7.48 dB
P1dB	-19 dBm	-22.1 dBm	-22 dBm
DC current[**]	7 mA	7.3 mA	5.6 mA
Area	1.92x0.86 mm^2		1.1x0.86 mm^2
Supply voltage	1.5 V		

[*] -10 dB
[†] ≤ -10 dB
[§] ≤ -20 dB
[**] Active core only
[‡] De-embedded buffers

Chapter 5

Measurements

The RFFEs are fabricated in a 9(+1)-metal layer 65 nm CMOS process. The microphotograph of the chip is shown in Fig. 5.1. Passive components, such as inductors, auto-transformers and transformers are implemented in the top ultra-thick-metal (UTM) layer (thickness > 3 µm). The total die area is 4 mm^2 (2x2 mm^2) including the reconfigurable RFFE (1.92x0.86 mm^2) and the area efficient (1.1x0.86 mm^2). Only for biasing, the IC is placed on a low frequency laminate with a 4.6 dielectric constant.
Our measurement setup comprised on-wafer test platform, vector network analyzer (VNA) and cables, up to 4×RF probes, and the device under test (DUT). For RF, on-wafer measurements and de-embedding can be challenging. All measurements are referenced to the probe-chip interface.

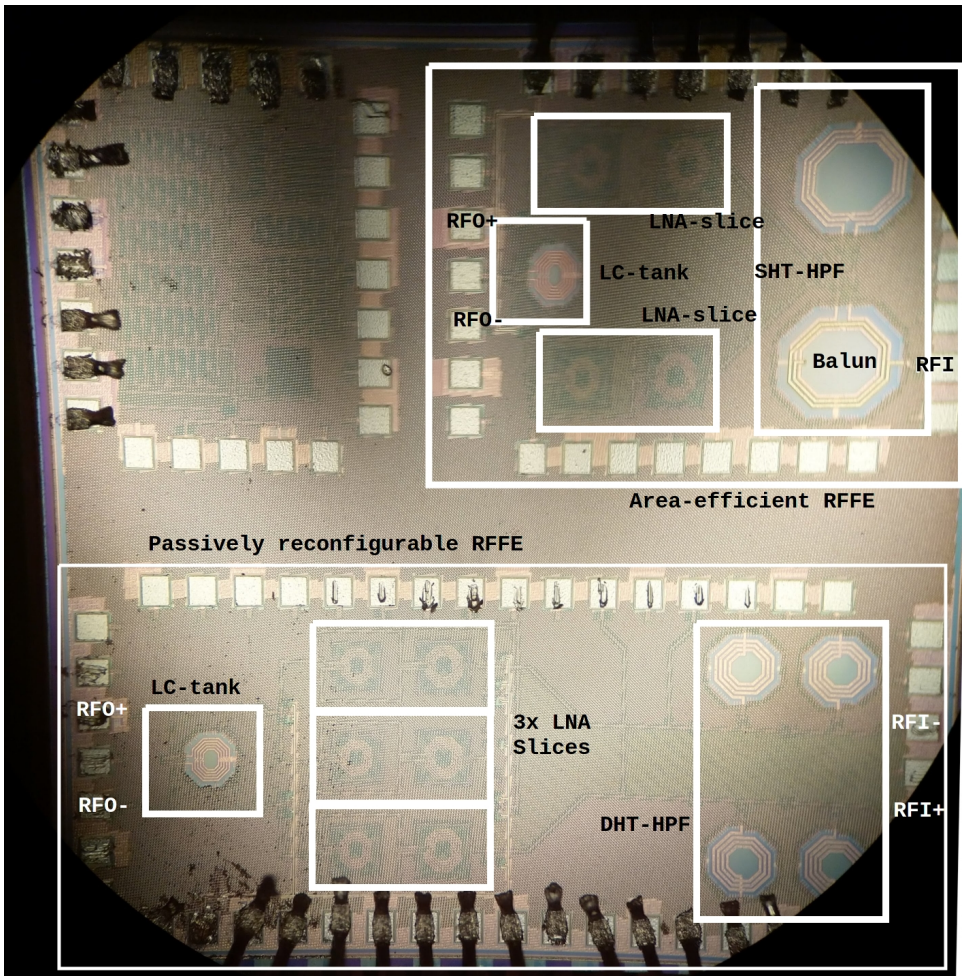

Figure 5.1: Microphotograph of the chip

5.1 Passively reconfigurable RFFE

For the passive reconfigurable RFFE (PR-RFFE), we use a total of 4×probes. In the half-duplex (HD) mode, we measure differentially, and thus, the two probe pairs have a 100 Ω differential impedance. For full-duplex (FD) mode, we measure with 1×single-ended 50 Ω probe (antenna port), 1×single-ended 50 Ω probe (TX port) and 1×differential 100 Ω probe (RX port). For S-parameter, port mapping: Port 1 = antenna (ANT), Port 2 = LNA output (RX), Port 3 = transmitter input (TX).

5.1.1 Half-duplex mode

The maximum return loss (S_{11}) of the RFFE, for a differential source impedance of 100 Ω is measured at 8.375 GHz and is −8.31 dB. The S_{11} −10 dB-bandwidth is 6.2-8.1 GHz. The S_{11} −20 dB-bandwidth is 7.2-7.6 GHz.

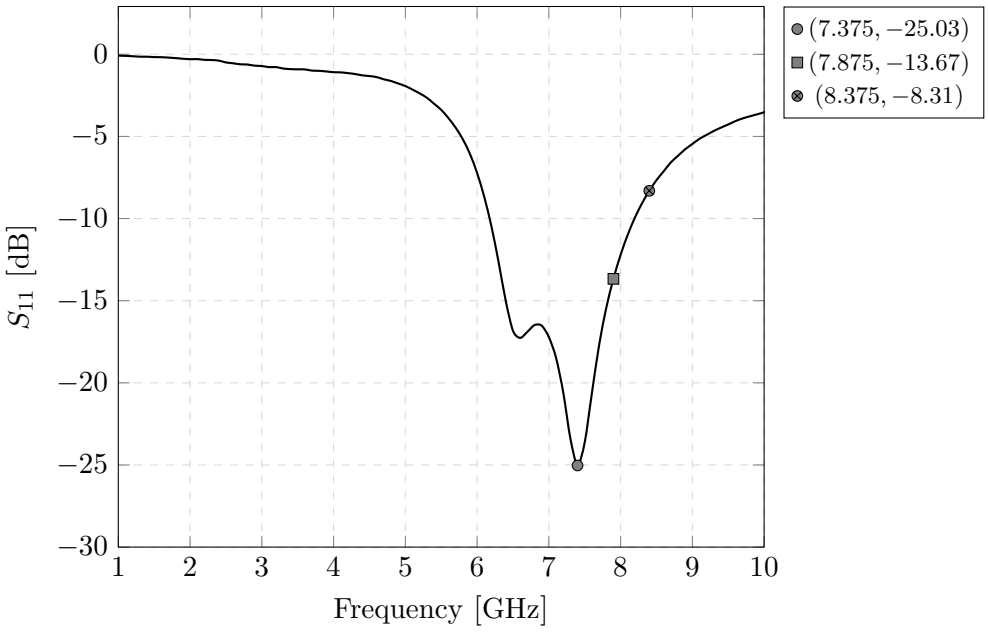

Figure 5.2: S_{11} of the PR-RFFE in HD-mode

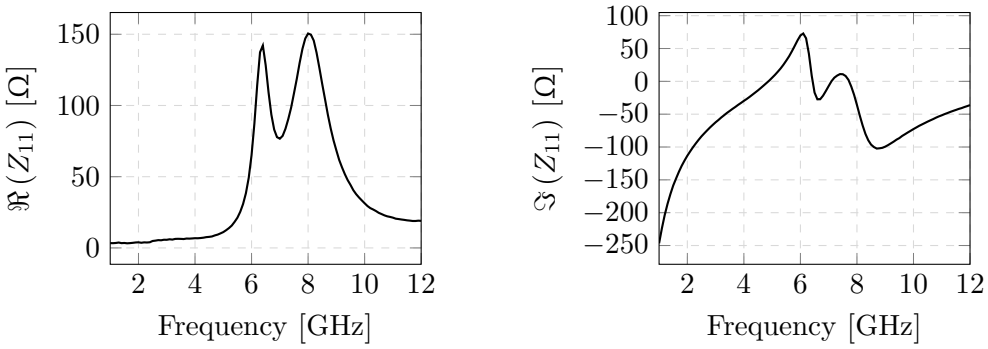

(a) $\Re(Z_{11})$ (b) $\Im(Z_{11})$

Figure 5.3: Real & imaginary input impedances of the PR-RFFE in HD-mode

The maximum output return loss (S_{22}) of the RFFE, for a differential load impedance of 100 Ω is measured at 8.375 GHz and is −11.98 dB. The S_{22} −10 dB-bandwidth is 1-10 GHz. The S_{22} −20 dB-bandwidth is 7-7.2 GHz.

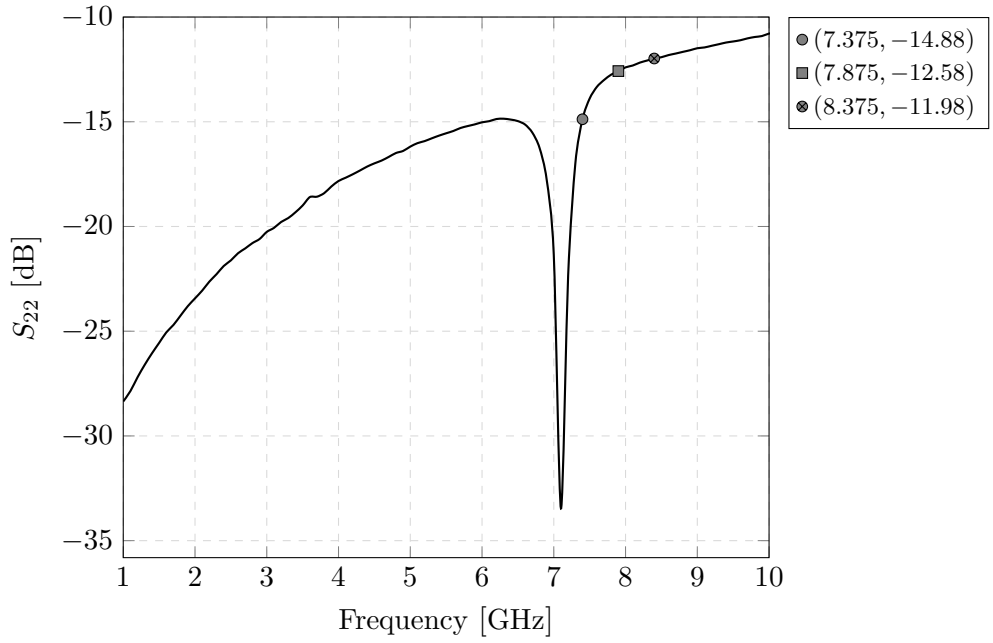

Figure 5.4: S_{22} of the PR-RFFE in HD-mode

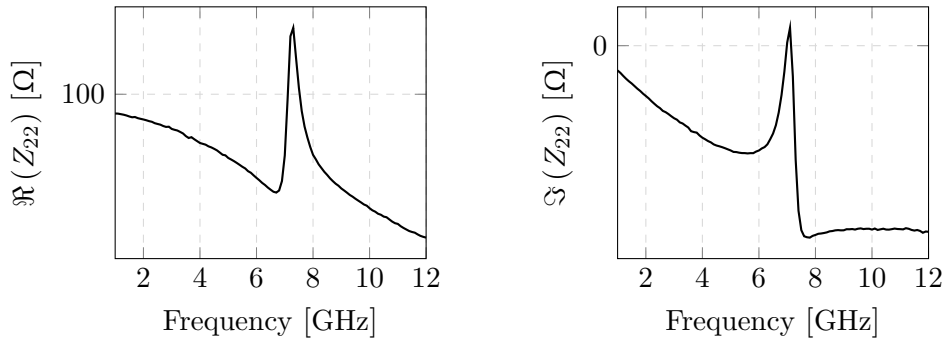

(a) $\Re(Z_{22})$ (b) $\Im(Z_{22})$

Figure 5.5: Real & imaginary output impedances of the PR-RFFE in HD-mode

The voltage gain (A_V) is reported as the maximum gain, and the bandwidth is reported as the -10 dB-bandwidth. In this RFFE, there was no de-embedding of output buffers. The maximum gain at the resonant frequency 7.2 GHz is 16.3 dB. The -10 dB BW is 1.2 GHz. Relative to the resonant frequency the BW is ± 600 MHz.

Attenuation at the bands of interest are:

$$\text{Rejection} = \begin{cases} \geq 31.88\,\text{dB}, & f \in [0, 2.4]\,\text{GHz}, \\ \geq 20.90\,\text{dB}, & f \in [2.4, 5.0]\,\text{GHz}, \\ 20.81\,\text{dB}, & f = 5.8\,\text{GHz} \end{cases} \tag{5.1}$$

The aforementioned meets specifications.

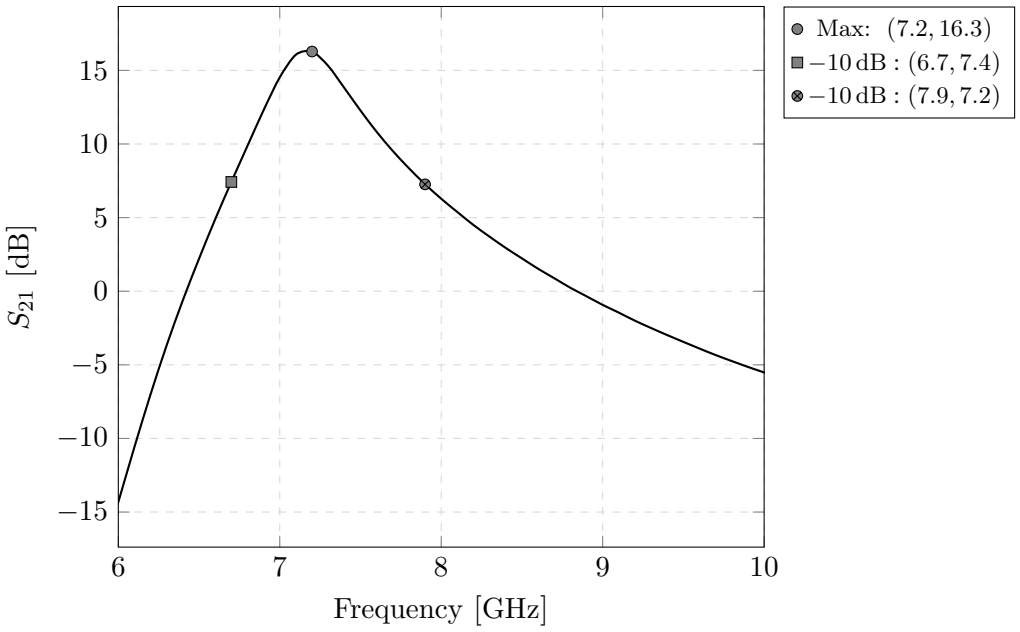

(a) Zoomed in from 6-10 GHz

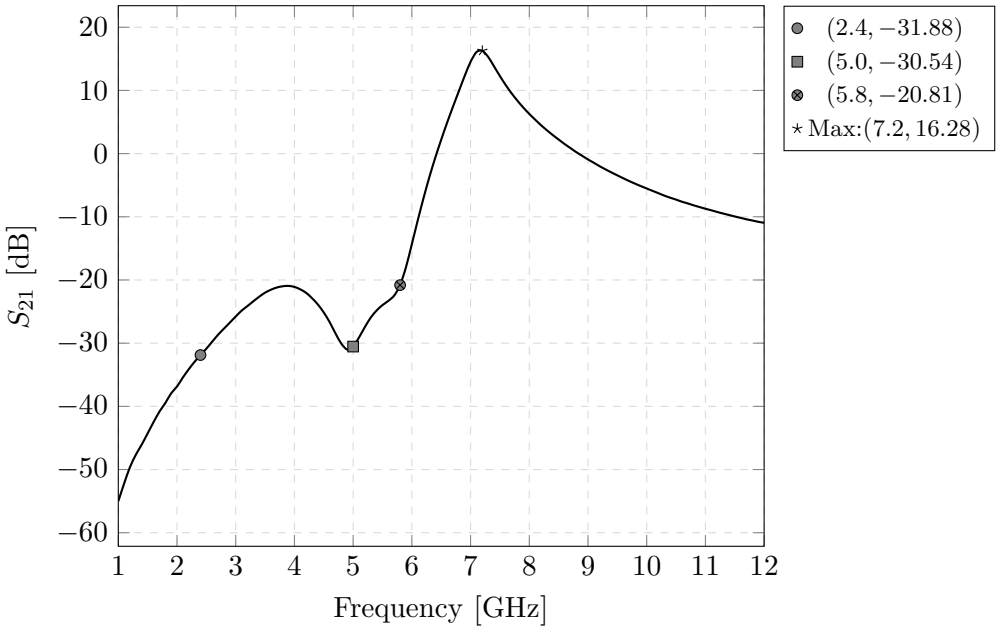

(b) In-band and out-of-band

Figure 5.6: Forward voltage gain of the PR-RFFE in HD-mode

The minimum reverse isolation is at 7.875 GHz, and is −58.23 dB.

For values lower than −50 dB, we start approaching the noise floor of the measurement setup. Thus, all signals lower than −50 dB, will be reported as < -50 dB.

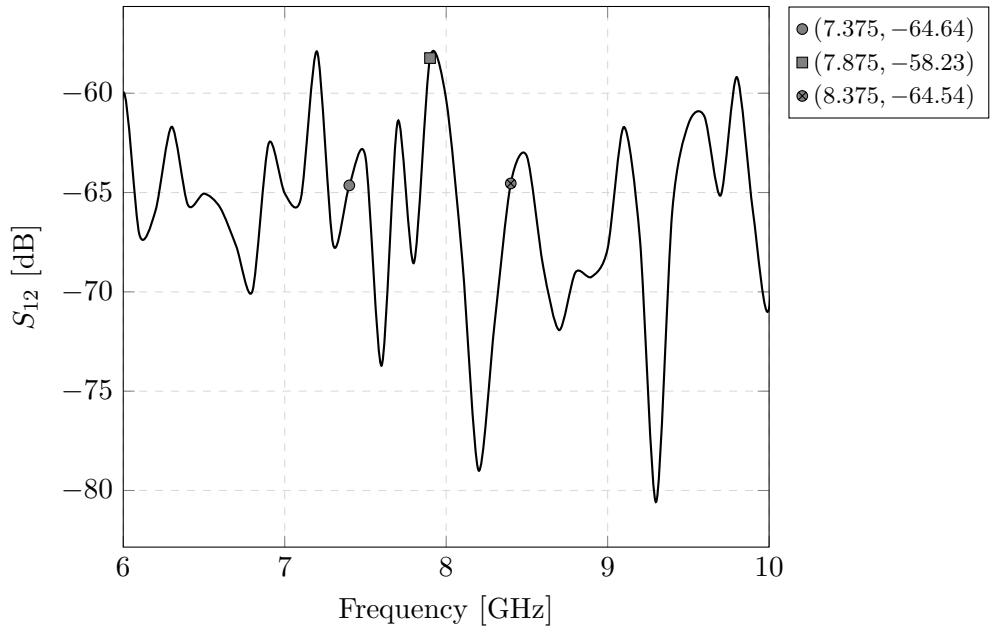

Figure 5.7: Reverse isolation of the PR-RFFE in HD-mode

For stability, we use the μ-stability test, if $\mu > 1$, the RFFE is unconditionally stable. The minimum value of μ is $\mu_{min} = 3.95$ at 8.375 GHz (passband).

As shown in Fig. 5.8, we meet the condition for unconditionally stability from 6-10 GHz.

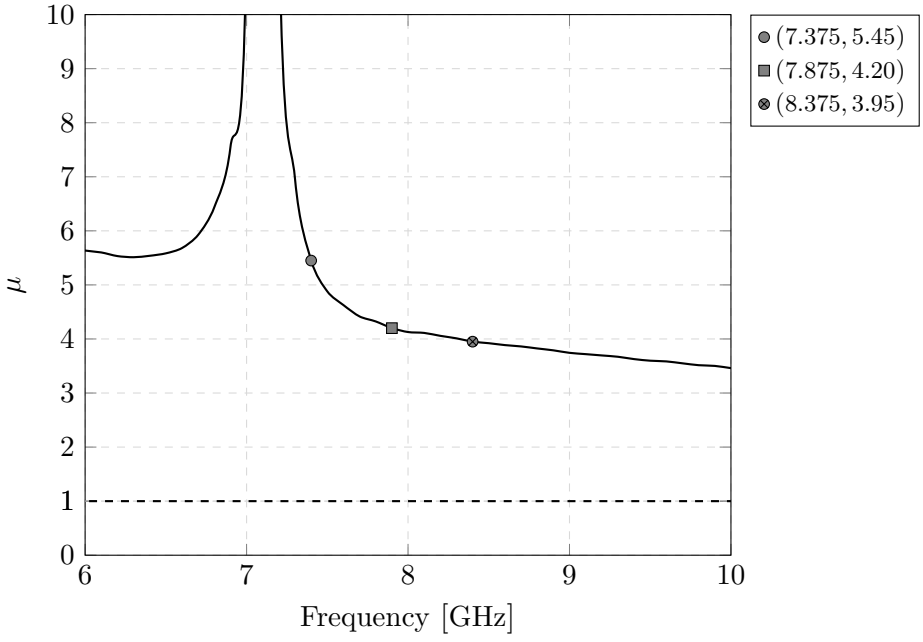

Figure 5.8: μ-factor

For the 1 dB compression point (P1dB), we use large signal S-parameters (LSSP), where we sweep the input power, P_{RF}

From Fig. 5.9, the P1dB is −19 dBm, which is 8 dB higher than required.

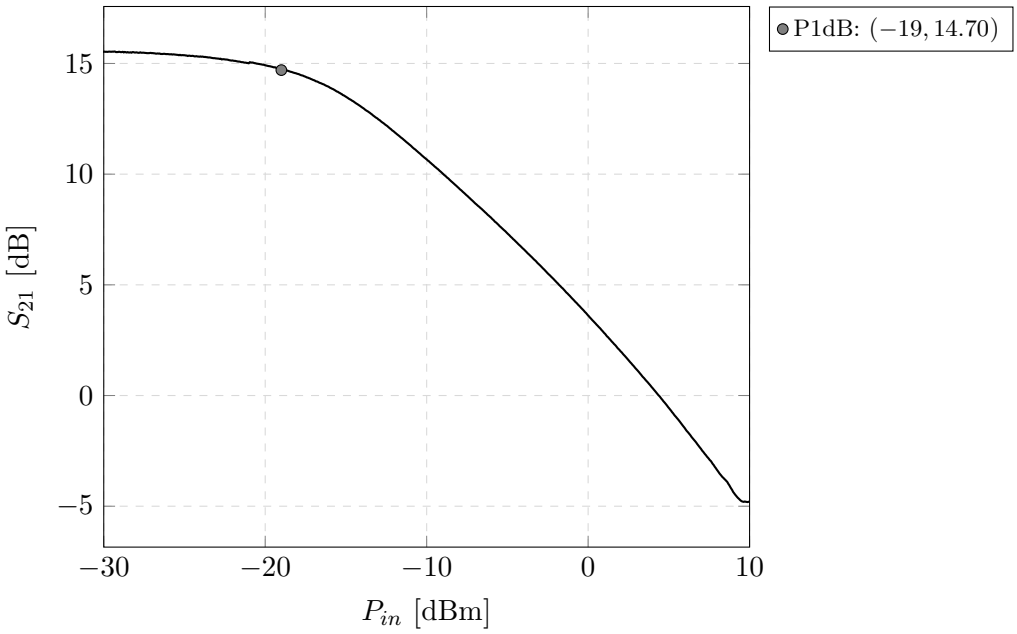

Figure 5.9: Large signal S-parameter, S_{21}, for PR-RFFE in HD-mode

The total current consumption, I_{DC} of the PR-RFFE in HD-mode is 13.8 mA. The active core consumes 7.3 mA, and the buffers 6.5 mA. As a proof of concept, we will not pay too much attention to current consumption.

5.1.2 Full-duplex mode

The maximum return loss (S_{11}) of the RFFE, for a differential source impedance of 50 Ω is measured at 8.375 GHz and is −8.32 dB. The S_{11} −10 dB-bandwidth is 6.2-8.1 GHz.

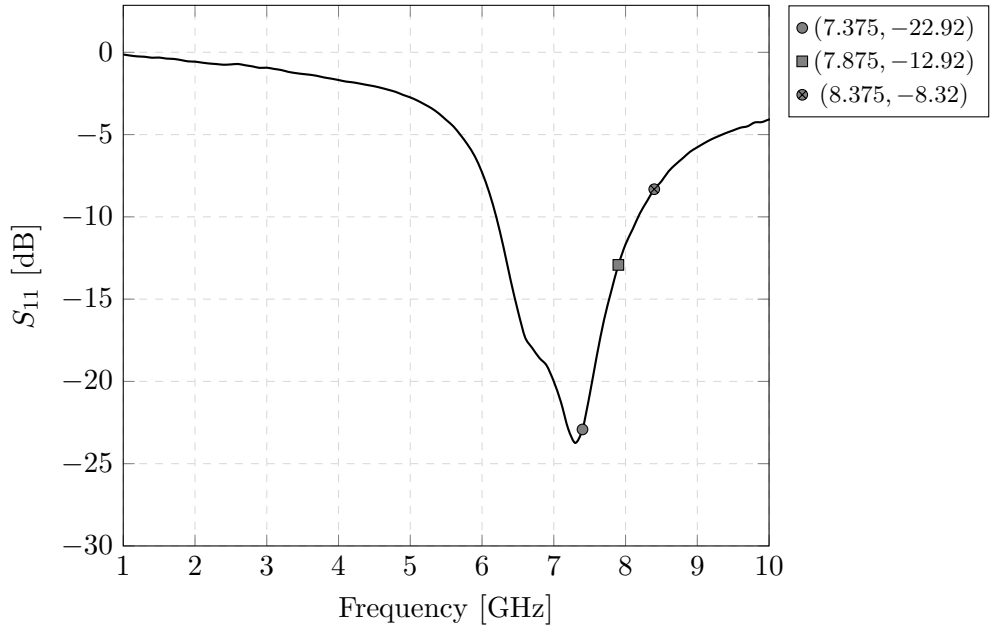

Figure 5.10: S_{11} of the PR-RFFE in FD-mode

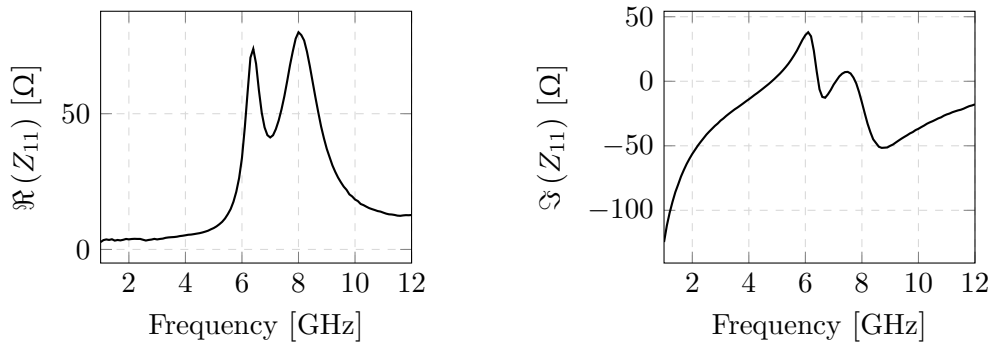

(a) $\Re(Z_{11})$ (b) $\Im(Z_{11})$

Figure 5.11: Real & imaginary input impedance of the area-optimized RFFE.

The maximum output return loss (S_{22}) of the RFFE, for a differential load impedance of 100 Ω is measured at 8.375 GHz and is −13.36 dB. The S_{22} −10 dB-bandwidth is 1-10 GHz. The S_{22} −20 dB-bandwidth is a single point at 7.5 GHz.

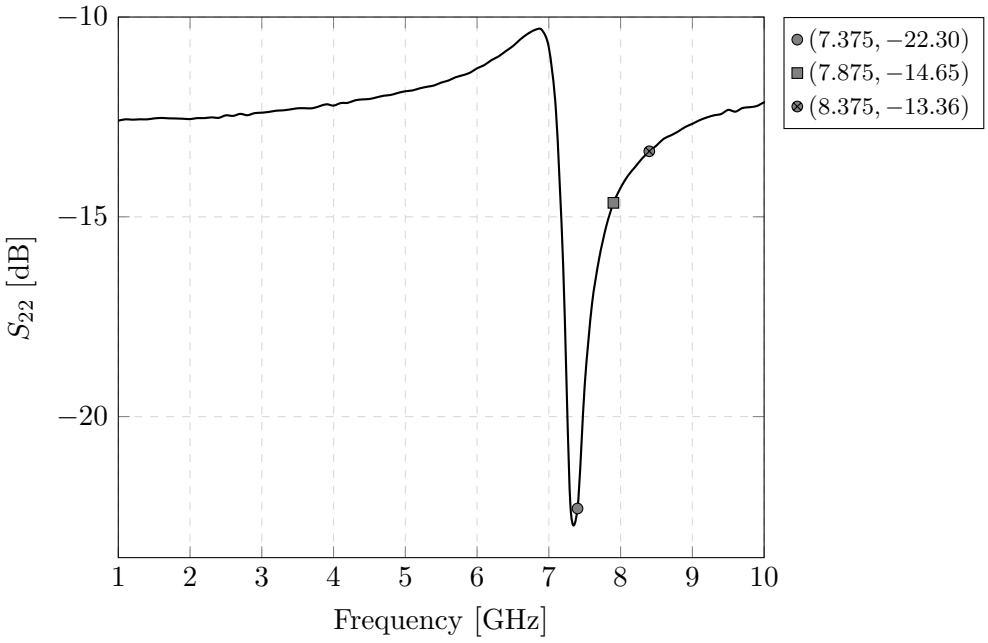

Figure 5.12: S_{22} of the PR-RFFE in FD-mode

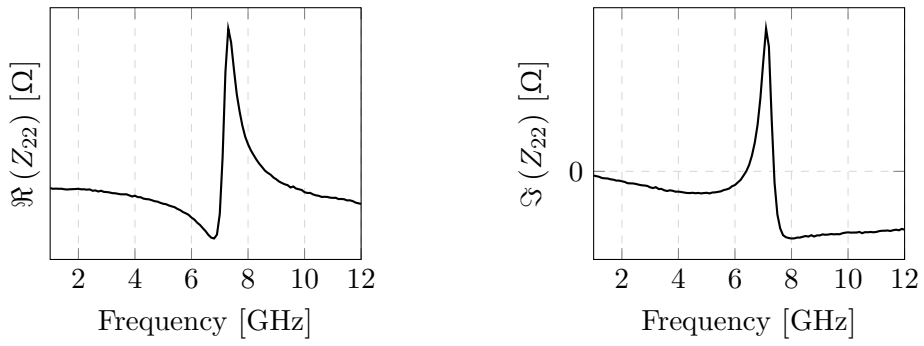

(a) $\Re(Z_{22})$ (b) $\Im(Z_{22})$

Figure 5.13: Real & imaginary output impedance of the PR-RFFE in FD-mode

The maximum input return loss for TX (S_{33}) of the RFFE, for a single-ended source impedance of 50 Ω is measured at 8.375 GHz and is −11.30 dB. The S_{33} −10 dB-bandwidth is 1-10 GHz. The S_{33} −20 dB-bandwidth are out-of-bound (< 2.6 GHz).

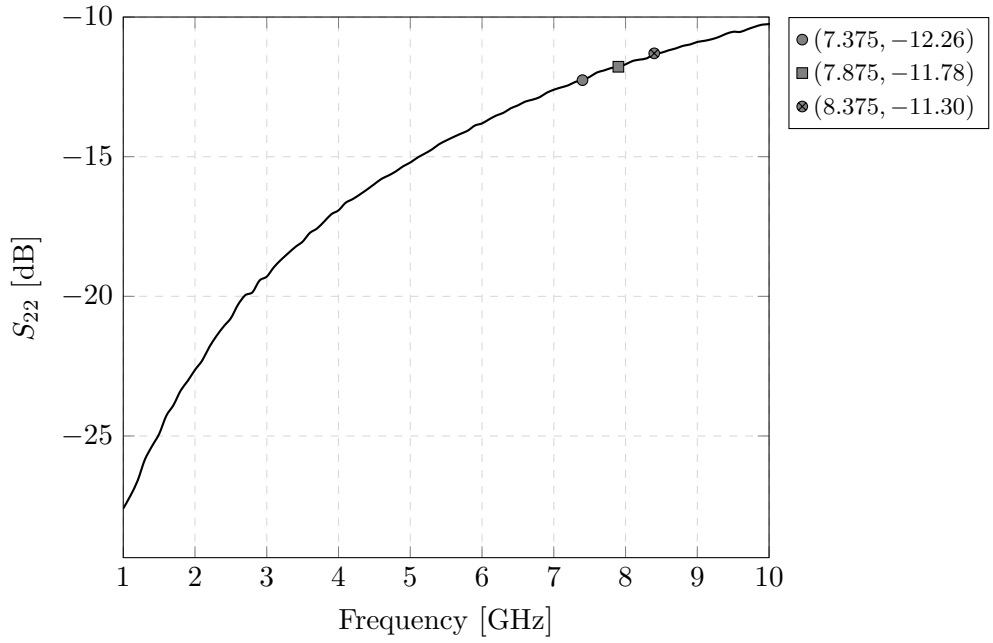

Figure 5.14: S_{33} of the PR-RFFE in FD-mode

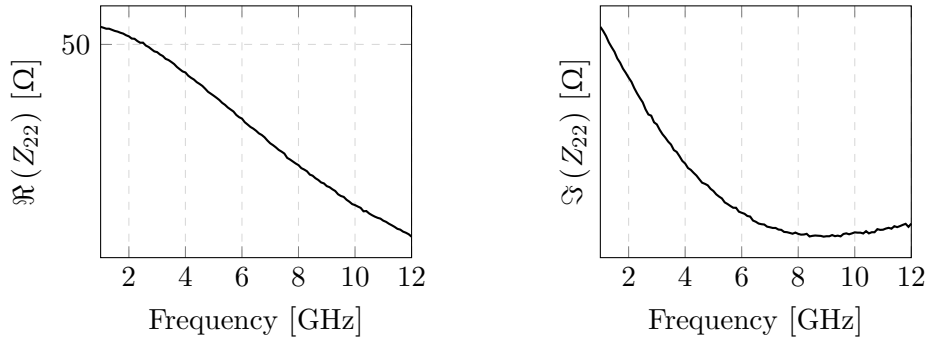

(a) $\Re(Z_{33})$ (b) $\Im(Z_{33})$

Figure 5.15: Real & imaginary input impedances on TX port of the PR-RFFE in FD-mode

The voltage gain (A_V) is reported as the maximum gain, and the bandwidth is reported as the $-10\,\text{dB}$-bandwidth. In this RFFE, there was no de-embedding of output buffers. The maximum gain at the resonant frequency 7.2 GHz is 13.7 dB. The $-10\,\text{dB}$ BW is 1.4 GHz. Relative to the resonant frequency the BW is $\pm 700\,\text{MHz}$.

Attenuation at the bands of interest are:

$$\text{Rejection} = \begin{cases} \leq 34.20\,\text{dB}, & f \in [0, 2.4]\,\text{GHz}, \\ \leq 23.29\,\text{dB}, & f \in [2.4, 5.0]\,\text{GHz}, \\ 23.51\,\text{dB}, & f = 5.8\,\text{GHz} \end{cases} \tag{5.2}$$

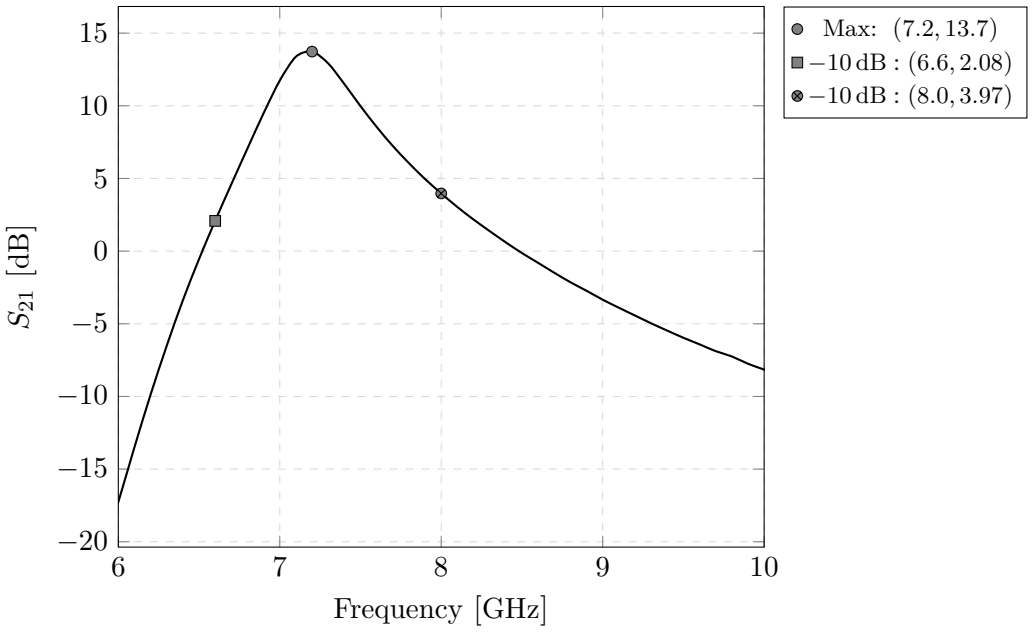

(a) Zoomed in from 6-10 GHz

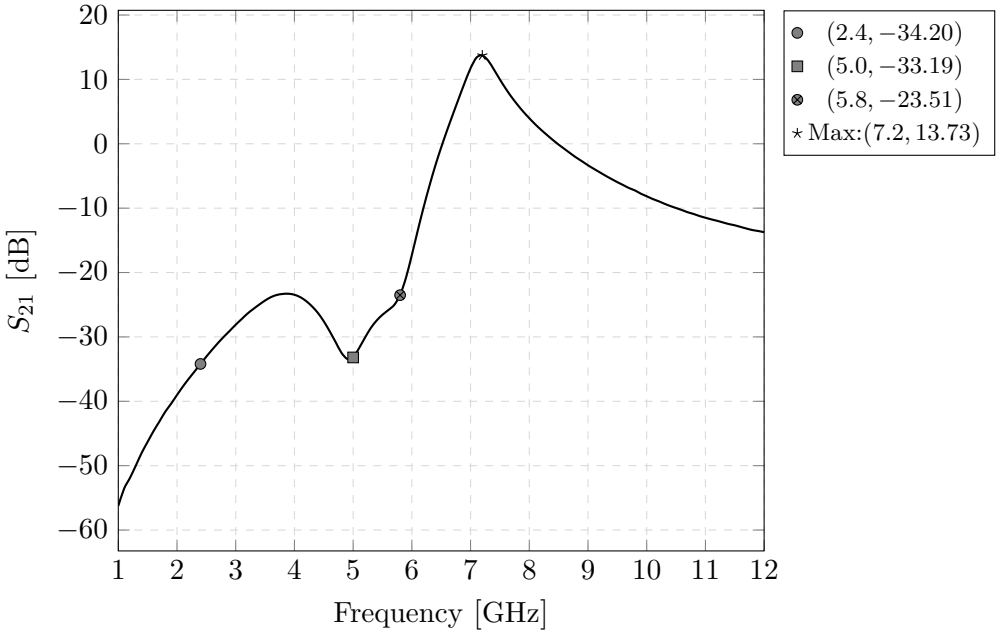

(b) In-band and out-of-band

Figure 5.16: Forward voltage gain of the PR-RFFE in FD-mode

The voltage gain from TX to the RX port ($A_{V|TX-RX}$) is reported as the maximum gain. The maximum gain is $-7.8\,\text{dB}$ at the resonance frequency of the LNA (7.2 GHz). The maximum gain looking into the antenna from the TX is $A_{V|TX-ANT} = -10.9\,\text{dB}$. Thus, the TX-RX isolation is:

$$A_{V|TX-RX} = (S_{23} + |S_{13}|) - S_{21} \tag{5.3}$$

where S_{23} is the unwanted forward transmission gain from TX to RX, S_{13} is the interface loss from TX to RX, and S_{21} is the forward voltage gain.

From Figs. 5.16 and 5.17, we have:

$$A_{V|TX-RX} = (-7.8\,\text{dB} + |-16.71\,\text{dB}|) - 13.73\,\text{dB} = -4.82\,\text{dB},$$

or $\approx 5\,\text{dB}$ cancellation. Due to the high loss at the interface, it is difficult to de-embed whether this is the actual cancellation or not.

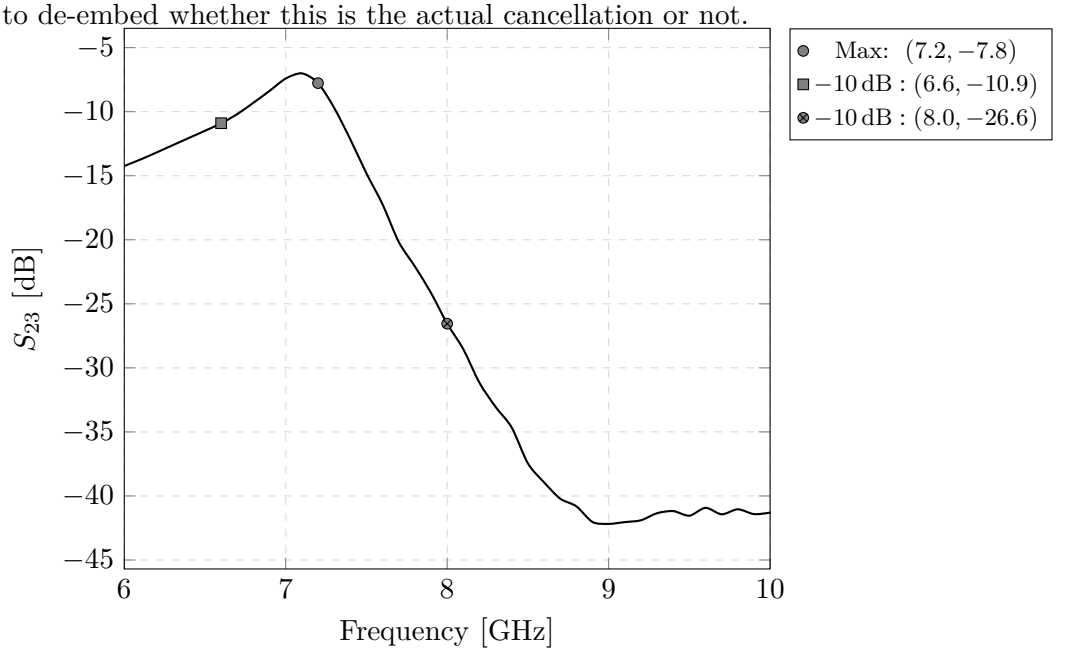

(a) TX to RX

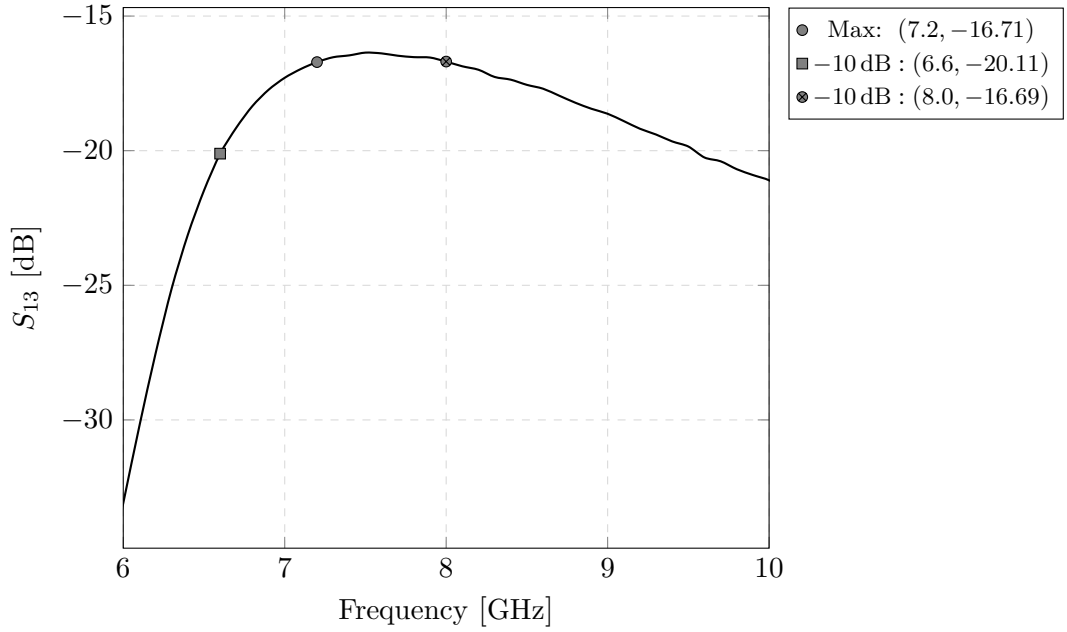

(b) TX to ANT

Figure 5.17: Forward transmission gain, using TX as input port

The minimum reverse isolation is -65.10 at $8.375\,\text{GHz}$ (passband).
For values lower than $-50\,\text{dB}$, we start approaching the noise floor of the measurement setup. Thus, all signals lower than $-50\,\text{dB}$, will be reported

as $< -50\,\text{dB}$.

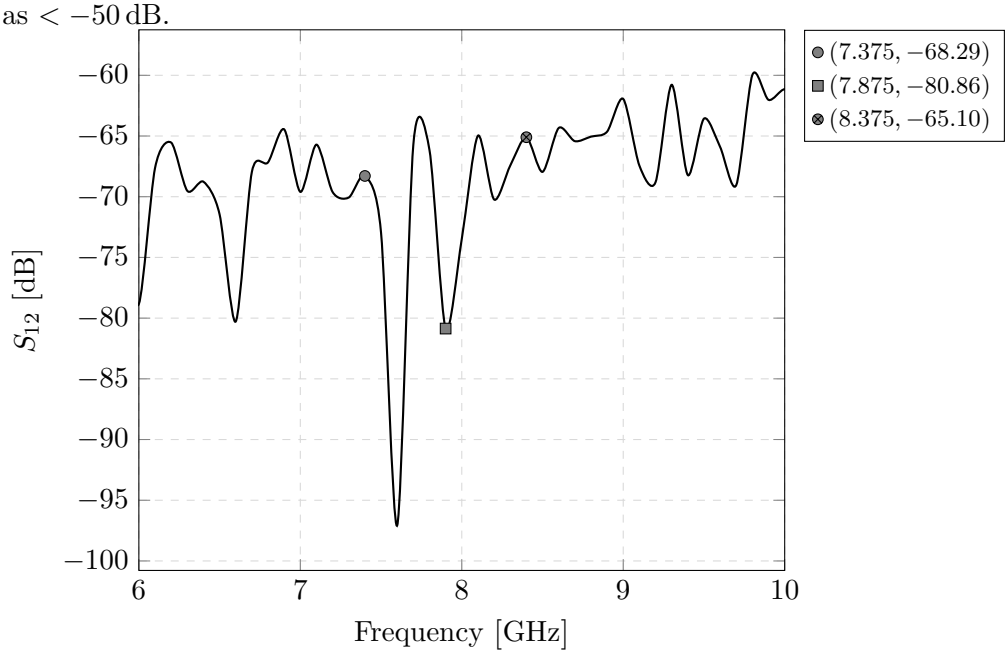

Figure 5.18: Reverse isolation of the area-optimized RFFE

For stability, we use the μ-stability test, if $\mu > 1$, the RFFE is unconditionally stable. The minimum value of μ is $\mu_{min} = 4.46$ at 8.375 GHz (passband).

As shown in Fig. 4.40, we meet the condition for unconditionally stability from 6-10 GHz.

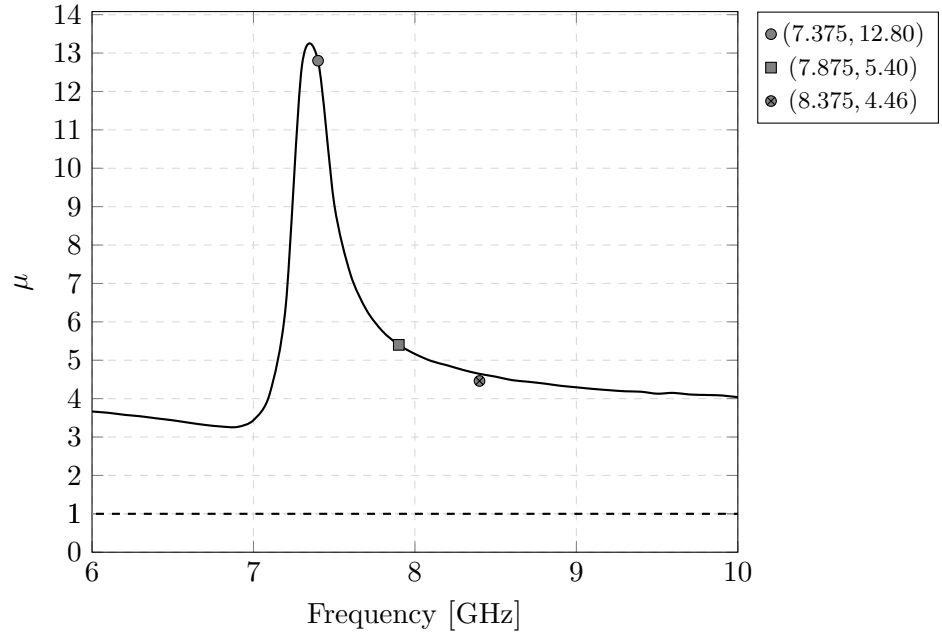

Figure 5.19: μ-factor for stability

For 1 dB compression point (P1dB), we use large signal S-parameters (LSSP), where we sweep the input power, P_{RF}.From Fig. 5.20, the P1dB is -22 dBm, which is 8 dB higher than required.

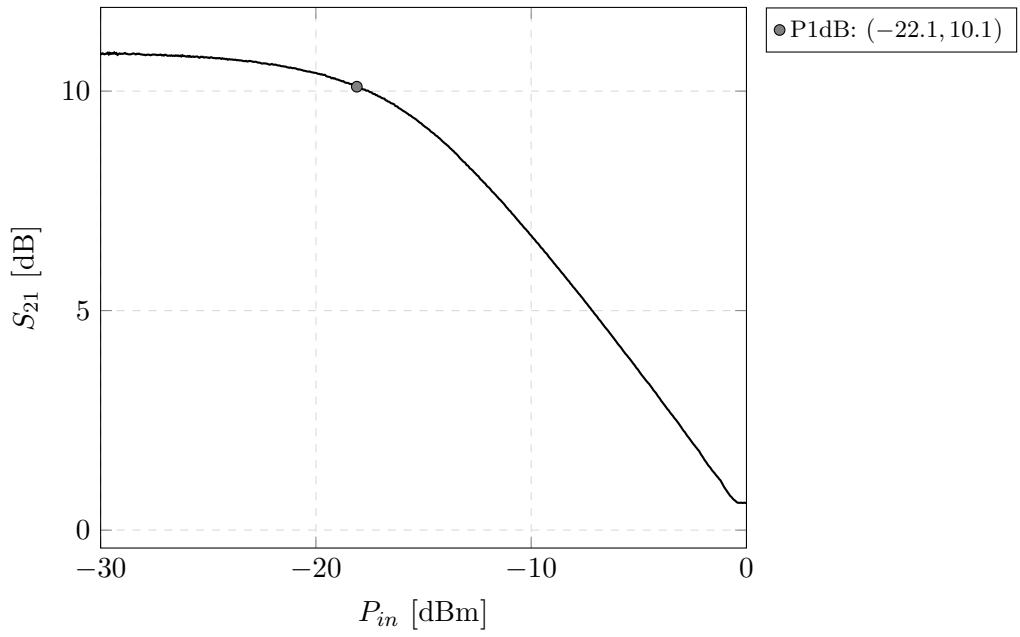

Figure 5.20: Large signal S-parameter, S_{21}, PR-RFFE in FD-mode

The total current consumption, I_{DC} of the PR-RFFE in FD-mode is 23.7 mA. The active core consumes 7.3 mA,the buffers 6.5 mA and the TX-drivers 9.9 mA. As a proof of concept, we will not pay too much attention to current consumption.

	Measurement		Simulation	
	HD	FD	HD	FD
Gain	16.3 dB	13.7 dB	26.8 dB**	13.7 dB**
Bandwidth*	6.7-7.9 GHz	6.6-8.0 GHz	6.7-7.9 GHz	6.6-8.0 GHz
Rejection:				
@ 2.4 GHz	31.88 dB	34.20 dB	27.33 dB**	30.15 dB**
@ 5 GHz	20.90 dB	23.29 dB	18.71 dB	21.87 dB
@ 5.8 GHz	20.81 dB	23.51 dB	6.1 dB	9.67 dB
S_{11}:				
Minimum†	6.2-8.1 GHz	6.2-8.1 GHz	6.1-8.9 GHz	6.2-9.2 GHz
Desired§	7.2-7.6 GHz	N/A	8.1 GHz	7.6-8.2 GHz
S_{22}:				
Minimum†	1-10 GHz	1-10 GHz	7.4-10 GHz	7.4-10 GHz
Desired§	7-7.2 GHz	7.5 GHz	N/A	N/A
S_{33}:				
Minimum†	N/A	1-10 GHz	N/A	1-10 GHz
Desired§	N/A	$\leq$ 2.6 GHz	N/A	$\leq$ 2.6 GHz
Reverse isolation	$>$ 50 dB	$>$ 50 dB	70 dB	50 dB
TX-RX isolation	N/A	5 dB	N/A	$\geq$ 12.51 dB
Stability, μ-factor	$\geq$ 3.95	$\geq$ 4.46	$\geq$ 3.35	$\geq$ 4.46
NF	N/A	N/A	$\leq$ 5.68 dB	$\leq$ 9.76 dB
P1dB	$-$19 dBm	$-$22.1 dBm	$-$19 dBm	$-$22.1 dBm
DC current	13.8 mA	23.7 mA	27 mA	37.4 mA
Area	1.92x0.86 mm^2			
Supply voltage	1.4 V		1.5 V	

* $-$10 dB
† ≤ -10 dB
§ ≤ -20 dB
** Buffer de-embedded

5.2 Area-optimized RFFE

The area-optimized RFFE, which is a single-ended to differential structure, has a a single-ended 50 Ω probe at the input, and a differential 100 Ω probe pair at the output.

The maximum return loss (S_{11}) of the RFFE, for a differential source impedance of 50 Ω is measured at 7.875 GHz and is $-$13.13 dB. The S_{11} $-$10 dB-bandwidth is 6.8-10 GHz.

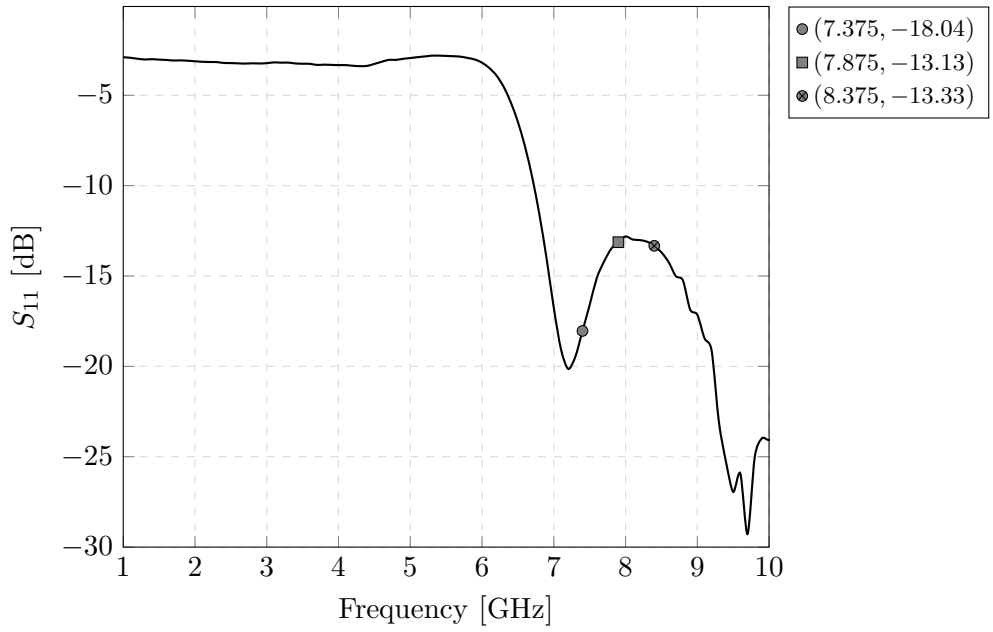

Figure 5.21: S_{11} of the area-optimized RFFE.

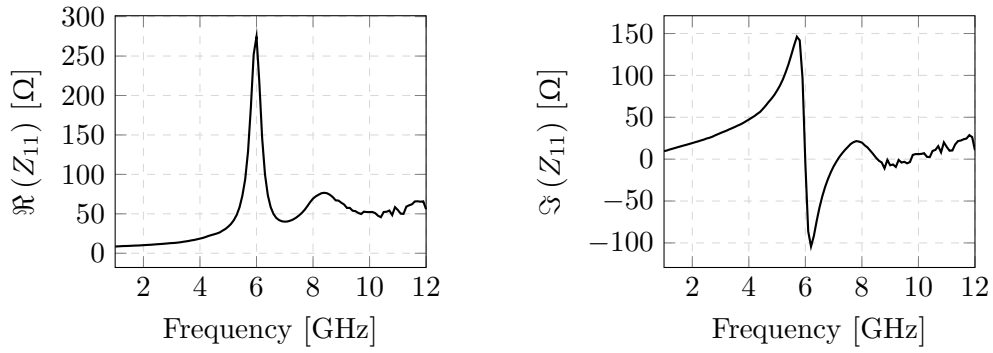

(a) $\Re(Z_{11})$ (b) $\Im(Z_{11})$

Figure 5.22: Real & imaginary input impedance of the area-optimized RFFE.

The maximum output return loss (S_{22}) of the RFFE, for a differential load impedance of 100 Ω is measured at 8.375 GHz and is −10.56 dB. The S_{22} −10 dB-bandwidth is 1-10 GHz.

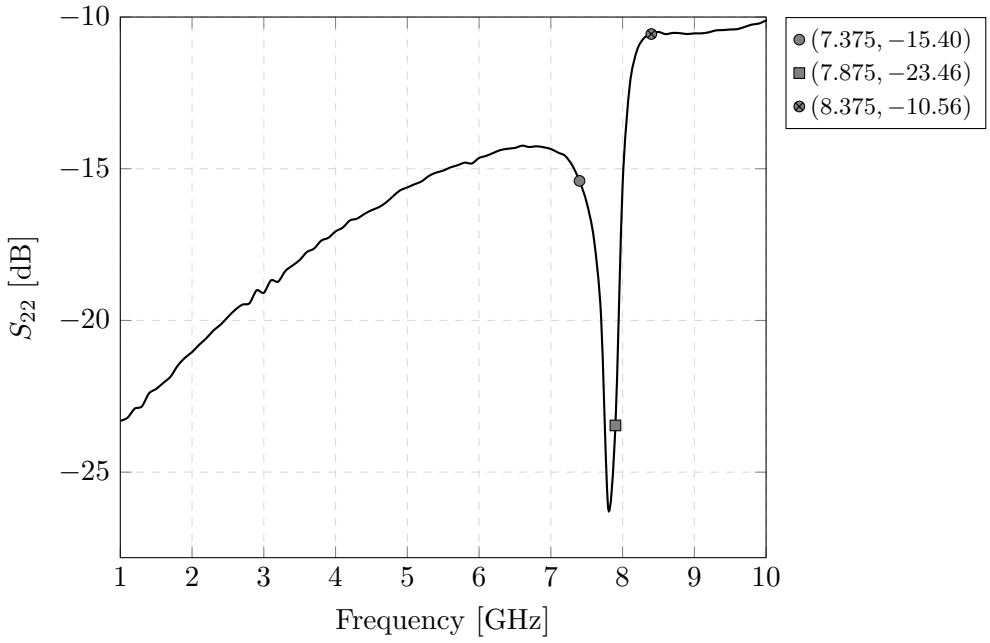

Figure 5.23: S_{22} of the SEDERFFE.

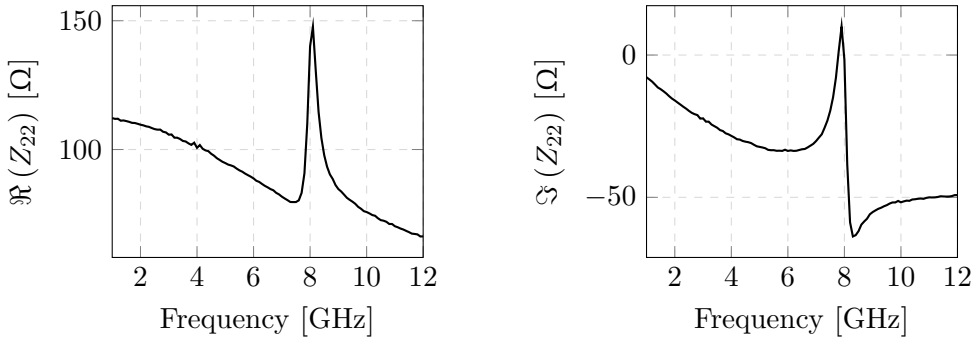

(a) $\Re(Z_{22})$ (b) $\Im(Z_{22})$

Figure 5.24: Real & imaginary output impedance of the area-optimized RFFE.

The voltage gain (A_V) is reported as the maximum gain, and the bandwidth is reported as the −10 dB-bandwidth. In this RFFE, there was no de-embedding of output buffers. The maximum gain at the resonant frequency 8.0 GHz is 16.9 dB. The −10 dB BW is 1.3 GHz. Relative to the resonant frequency the BW is ±650 MHz.

Attenuation at the bands of interest are:

$$\text{Rejection} = \begin{cases} \geq 45.21\,\text{dB}, & f \in [0, 2.4]\,\text{GHz}, \\ \geq 16.43\,\text{dB}, & f \in [2.4, 5.0]\,\text{GHz}, \\ 18.81\,\text{dB}, & f = 5.8\,\text{GHz} \end{cases} \tag{5.4}$$

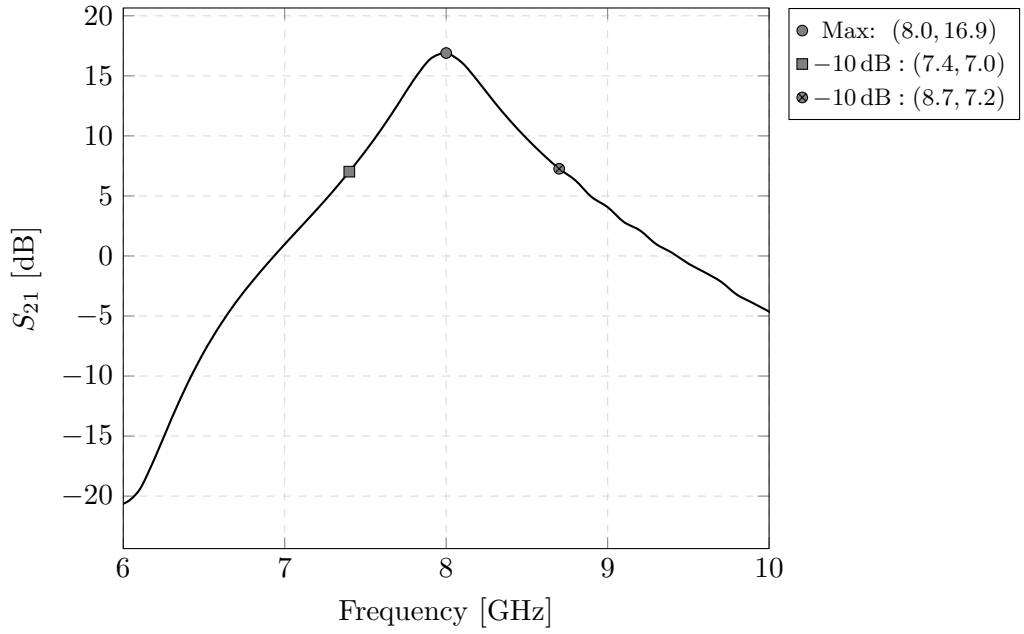

(a) Zoomed in from 6-10 GHz

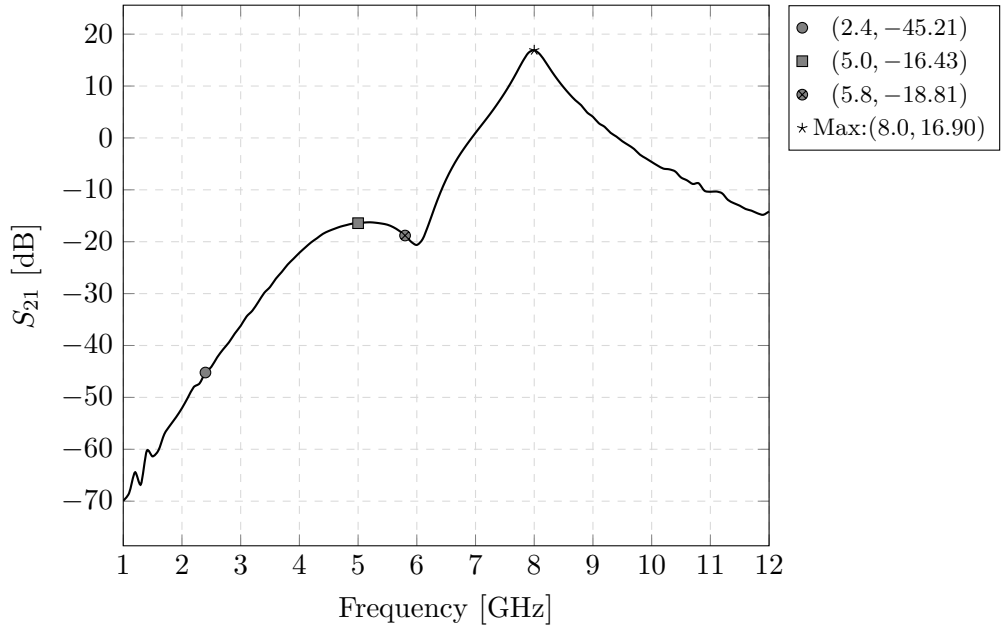

(b) In-band and out-of-band

Figure 5.25: Forward voltage gain of the area-optimized RFFE

The minimum reverse isolation is −58.33 at 7.875 GHz (passband).

For values lower than −50 dB, we start approaching the noise floor of the measurement setup. Thus, all signals lower than −50 dB, will be reported as < -50 dB.

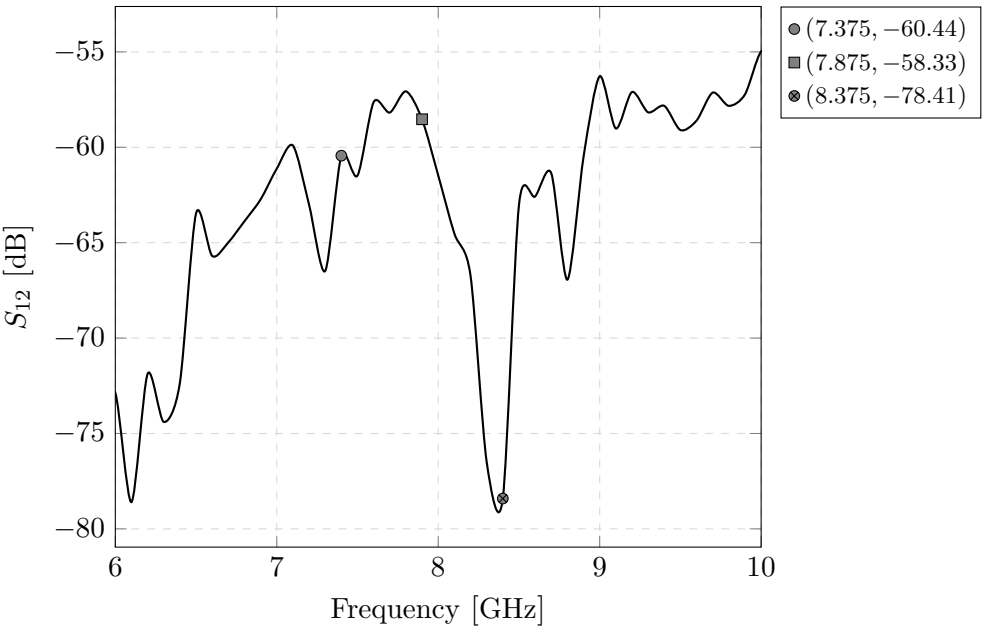

Figure 5.26: Reverse isolation of the area-optimized RFFE

For stability, we use the μ-stability test, if $\mu > 1$, the RFFE is unconditionally stable. The minimum value of μ is $\mu_{min} = 3.37$ at 8.375 GHz (passband).

As shown in Fig. 5.27, we meet the condition for unconditionally stability from 6-10 GHz.

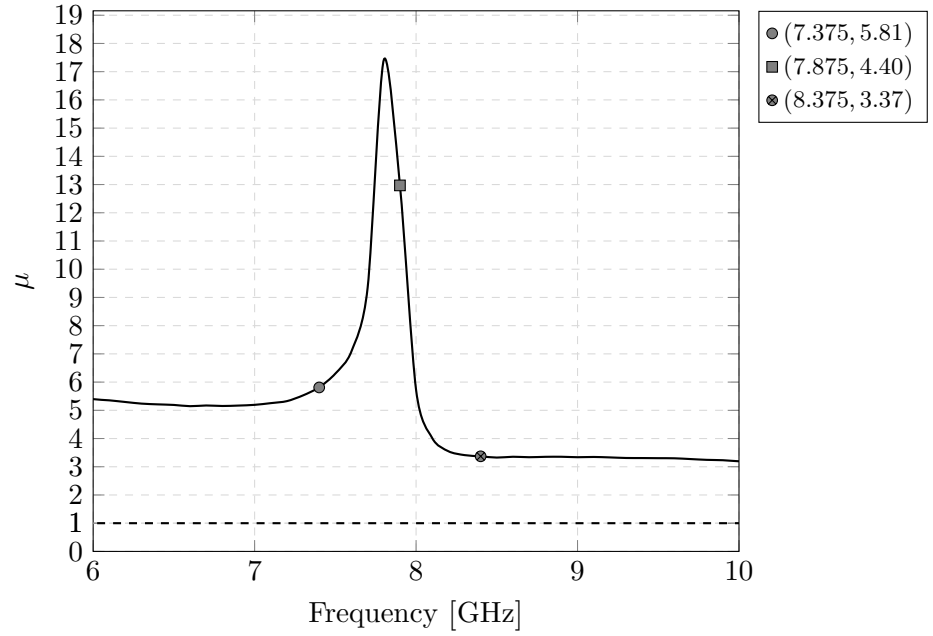

Figure 5.27: μ-factor for stability

For the 1 dB compression point (P1dB), we use large signal S-parameters (LSSP), where we sweep the input power, P_{RF}.From Fig. 5.28, the P1dB is −22 dBm, which is 8 dB higher than required.

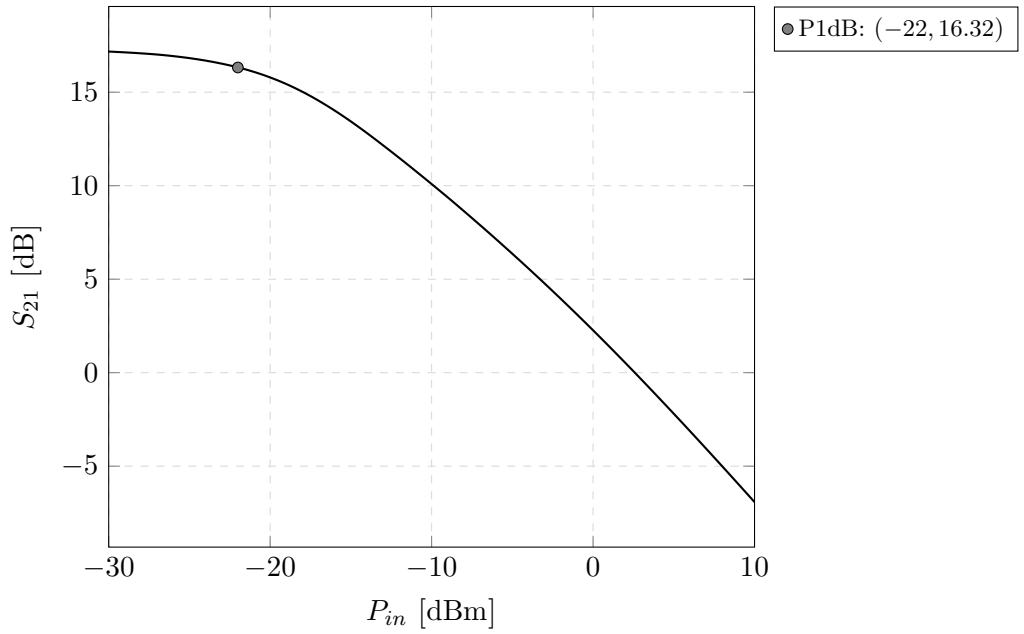

Figure 5.28: Large signal S-parameter, S_{21}, for area-optimized RFFE

The total current consumption, I_{DC} of the area-optimized RFFE in is 13.8 mA. The active core consumes 7.3 mA and the buffers 6.5 mA. As a proof of concept, we will not pay too much attention to current consumption.

	Measurement	Simulation
Gain	16.9 dB	24.57 dB**
Bandwidth*	7.4-8.7 GHz	7.4-8.8 GHz
Rejection:		
@ 2.4 GHz	45.21 dB	37.45 dB**
@ 5 GHz	16.43 dB	10.97 dB**
@ 5.8 GHz	18.81 dB	10.54 dB**
S_{11}:		
Minimum†	6.8-10 GHz	6.5-9.7 GHz
Desired§	$>$ 9.2 GHz	7.1-7.6 GHz
S_{22}:		
Minimum†	1-10 GHz	1-10 GHz
Desired§	$\leq$ 2.4 GHz	$\leq$ 4.4 GHz
Reverse isolation	$>$ 50 dB	$\geq$ 47.42 dB
Stability, μ-factor	$\geq$ 3.37	$\geq$ 4.18
NF	N/A	$\leq$ 7.48 dB
P1dB	-22 dBm	-22 dBm
DC current	13.8 mA	10 mA
Area	1.1x0.86 mm^2	
Supply voltage	1.4 V	1.5 V

* -10 dB
† ≤ -10 dB
§ ≤ -20 dB
** Buffer de-embedded

5.3 Summary

For the area optimized and passively configurable RFFEs, the measurement results closely match with specifications. For the AO-RFFE, rejection at 2.4 GHz and 5,5.8 GHz is off by ≈ 2 and ≈ 4 dB, respectively compared to HD PR-RFFE. Voltage gain compared to HD PR-RFFE is practically the same. For the FD PR-RFFE, we expect a 3 dB loss in gain.

	PR-RFFE		AO-RFFE
	HD	FD	
Gain	16.3 dB	13.7 dB	16.9 dB
Bandwidth*	6.7-7.9 GHz	6.6-8.0 GHz	7.4-8.7 GHz
Rejection:			
@ 2.4 GHz	31.88 dB	34.20 dB	45.21 dB
@ 5 GHz	20.90 dB	23.29 dB	16.43 dB
@ 5.8 GHz	20.81 dB	23.51 dB	18.81 dB
S_{11}:			
Minimum†	6.2-8.1 GHz	6.2-8.1 GHz	6.8-10 GHz
Desired§	7.2-7.6 GHz	N/A	$>$ 9.2 GHz
S_{22}:			
Minimum†	1-10 GHz	1-10 GHz	1-10 GHz
Desired§	7-7.2 GHz	7.5 GHz	$\leq$ 2.4 GHz
S_{33}:			
Minimum†	N/A	1-10 GHz	N/A
Desired§	N/A	$\leq$ 2.6 GHz	N/A
Reverse isolation	$>$ 50 dB	$>$ 50 dB	$>$ 50 dB
TX-RX isolation	N/A	5 dB	N/A
Stability, μ-factor	$\geq$ 3.95	$\geq$ 4.46	$\geq$ 3.37
NF	N/A	N/A	N/A
P1dB	-19 dBm	-22.1 dBm	-22.1 dBm
DC current	13.8 mA	23.7 mA	13.8 mA
Area	1.92x0.86 mm^2		1.1x0.86 mm^2
Supply voltage	1.4 V	1.5 V	

* -10 dB
† ≤ -10 dB
§ ≤ -20 dB

Chapter 6

Conclusion

In this work, we present two passive high-pass filters (HPF), a wideband reactive low-noise amplifier (LNA), a 'passively reconfigurable' RF front-end (RFFE) and an area efficient RFFE comprising said components. The reconfigurable RFFE can operate in half-duplex (HD) and full-duplex (FD) mode. In it's natural HD-mode, it is configured as pseudo-differential to pseudo-differential. In FD-mode, it is configured as single-ended to pseudo-differential. All blocks are realized in 65 nm CMOS.

The filter in the reconfigurable RFFE is a 4^{th}-order, pseudo-differential double harmonic trap (DHT) with 7 GHz -3 dB cut-off frequency and an insertion loss of <3 dB. Notches at 4.8 GHz & 5.6 GHz offer a minimum of 20 dB broadband (1500 MHz) rejection. The filter in the area efficient RFFE is a 4^{th}-order, single-ended to differential single harmonic trap (SHT) with a wideband on-chip $1{:}\sqrt{2}$ balun with a coupling coefficient of 0.82. For single-ended termination, the source impedance is 50 Ω. The cut-off frequency and insertion loss are 7.4 GHz and < 3.1 dB, respectively. Notch at 5.7 GHz offers a minimum of 15 dB rejection. The die area of the DHT and SHT HPFs is 0.757 mm^2 and 0.473 mm^2 respectively. The HPFs, especially the DHT can be used to overcome interference problems and improve coexistence of IEEE 802.15.z (e.g., 6-10 GHz) and IEEE 802.11a wireless RF systems.

Standalone, the 7.3-8.8 GHz tuned low-noise amplifier (LNA) provides at least 0 dB out-of-band rejection at frequencies in the 5 GHz-band. The power-to-voltage (P-V) configured LNA comprises of reactive-feedback and feedforward loops; negative current-current and positive voltage-voltage loops for impedance matching and g_m-boosting. The LNA achieves 22.3$\pm$5 dB gain, 4.29$\pm$0.07 dB noise figure at 6 mA and 1.5 V supply with -17 dBm 1-dB (P1dB), demonstrating design parameters well suited for impulse-radio ultra-wideband (IR-UWB). The die area of the LNA is 0.72 mm^2.

For the DHT and LNA configuration (in HD-mode), notches at 4.8 GHz and 5.6 GHz offer a minimum of -15 dB broadband (1400 MHz) rejection. The combined gain and noise figure 18$\pm$5 dB and 5.5$\pm$0.1 dB, respectively.

For FD-mode, there is a design flaw that need to be addressed, i.e., the impedance mismatch between the core and auxiliarybranches of the

LNA. This directly affects the amplitude and phase of the 'copied' signal required for cancelling out the transmitted signal.
Moreover, because of the limitation in the measurement setup, and higher than expected losses at the interface of the DHT HPF & LNA, we cannot accurately de-embed the TX-ANT/ANT-RX isolation.
For the area efficient RFFE (i.e., the SHT HPF and LNA configuration) provides a minimum of -10 dB rejection with a single notch at 5.7 GHz. The combined gain and noise figure is 19.57 ± 5 dB and 7.25 ± 0.25 dB, respectively. This design demonstrates on how to embed the self-inductance of the balun windings as part of the ladder filter implementation.
Measured results closely match specifications.

Future work

Configurable impedance matching network for TX-auxiliary For maximum TX-RX isolation we require amplitude and phase matching of the cancelling signal. Instead of a 'fixed' impedance for the auxiliary branch, we can use a configurable/switchable RC network. This provides tunability, and robustness to process-voltage-temperature (PVT) variations.

PVT For the LC tank in the LNA, we can replace the fixed capacitor with a trimmable switched-capacitor to compensate PVT effects. Similarly, adding switched-capacitor banks for the notch(es) in the HPFs provides frequency tuning.

Wi-Fi 6 GHz-band IN 2020, the Federal Communications Commission (FCC) opened up the 6 GHz-band for unlicensed use [20]. The 6 GHz-band stretches from 5.925-7.125 GHz. With the RFFEs in this work, these bands are a significant problem with regards to reliability. For future UWB-RFFEs, one requires significant rejection at 2.4 GHz-band, 5 GHz-band as well as the new 6 GHz-band if UWB-RFFEs are to co-exist with licensed devices.

Bibliography

[1] J. Yoshida. 'iPhone 11, Watch 5: What's New, What's Dropped'. In: *EETimes* (10th Apr. 2019). URL: https://www.eetimes.com/iphone-11-watch-5-whats-new-whats-dropped/ (visited on 12/12/2020).

[2] S. Asif. 'Galaxy Note 20 Ultra's UWB tech to be used for faster file sharing, digital keys'. In: *SamMobile* (6th Aug. 2020). URL: https://www.sammobile.com/news/galaxy-note-20-ultra-uwb-faster-file-transfers-digital-keys/ (visited on 12/12/2020).

[3] Decawave Ltd. *DW1000 Datasheet*. Version 2.22. 2017. URL: https://www.decawave.com/product/dw1000-radio-ic/ (visited on 12/12/2020).

[4] N. Dahad. 'Lenovo adds Novelda UWB sensor for human presence detection in ThinkPad'. In: *Embedded* (5th Nov. 2020). URL: https://www.embedded.com/lenovo-adds-novelda-uwb-sensor-for-human-presence-detection-in-thinkpad/.

[5] N. Andersen et al. 'A 118-mW Pulse-Based Radar SoC in 55-nm CMOS for Non-Contact Human Vital Signs Detection'. In: *IEEE Journal of Solid-State Circuits* 52.12 (2017), pp. 3421–3433. DOI: 10.1109/JSSC.2017.2764051.

[6] X. Yi et al. 'A 3.4–4.6GHz In-Band Full-Duplex Front-End in CMOS Using a Bi-Directional Frequency Converter'. In: *2020 IEEE Radio Frequency Integrated Circuits Symposium (RFIC)*. 2020, pp. 47–50. DOI: 10.1109/RFIC49505.2020.9218445.

[7] Heimo Uhrmann, Robert Kolm and Horst Zimmermann. *Analog Filters in Nanometer CMOS*. eng. Vol. 45. Springer Series in Advanced Microelectronics. Springer Berlin / Heidelberg, 2013. ISBN: 9783642430299.

[8] Analog Devices Inc. *Linear circuit design handbook*. eng. 1st edition. Elsevier/Newnes Press, 2008. ISBN: 1-281-27326-0.

[9] David M. Pozar. *Microwave engineering*. eng. 4th ed. Chichester: Wiley, 2012. ISBN: 9780470631553.

[10] Hooman Darabi. *Radio Frequency Integrated Circuits and Systems*. eng. 1st ed. Cambridge University Press, 2015. ISBN: 9780521190794.

[11] J. R. Long. 'Monolithic transformers for silicon RF IC design'. In: *IEEE Journal of Solid-State Circuits* 35.9 (Sept. 2000), pp. 1368–1382. ISSN: 1558-173X. DOI: 10.1109/4.868049.

[12] B. Razavi. *Design of Analog CMOS Integrated Circuits*. 2nd ed. McGraw-Hill Higher Education, 2016. ISBN: 9780077496128.

[13] A.M. Niknejad. *Electromagnetics for High-Speed Analog and Digital Communication Circuits*. 1st ed. Cambridge University Press, 2007. ISBN: 9781139462242.

[14] T.H. Lee. *The Design of CMOS Radio-Frequency Integrated Circuits*. 2nd ed. Cambridge University Press, 2004. ISBN: 9780521835398.

[15] B. Razavi. *RF Microelectronics*. 2nd ed. Pearson Education International, 2012. ISBN: 9780132839419.

[16] Xiaoyong Li, S. Shekhar and D. J. Allstot. 'G_m-boosted common-gate LNA and differential colpitts VCO/QVCO in 0.18-μ m CMOS'. In: *IEEE Journal of Solid-State Circuits* 40.12 (2005), pp. 2609–2619. DOI: 10.1109/JSSC.2005.857426.

[17] B.E. Boser. 'Analog Design Using g_m/I_d and f_t Metrics'. In: (2011). URL: https://people.eecs.berkeley.edu/~boser/presentations/2011-12%20OTA%20gm%20Id.pdf.

[18] National Instruments. *Advantages of Direct RF Sampling Architectures*. National Instruments. 5th Mar. 2019. URL: https://www.ni.com/en-no/innovations/white-papers/18/advantages-of-direct-rf-sampling-architectures.html (visited on 14/02/2020).

[19] Tommy Neu. *Direct RF conversion: From vision to reality*. Texas Instruments. May 2015. URL: http://www.ti.com/lit/slyy068 (visited on 14/12/2020).

[20] Federal Communications Commision. *FCC Opens 6 GHz Band to Wi-Fi and Other Unlicensed Uses*. Federal Communications Commision. 23rd Apr. 2020. URL: https://www.fcc.gov/document/fcc-opens-6-ghz-band-wi-fi-and-other-unlicensed-uses (visited on 13/12/2020).